JCMM

Implications for Mesoscale Modelling from a Study of the FASTEX IOP 16 Mid-latitude Cyclone

Richard M Forbes, Humphrey W Lean,
Nigel M Roberts and Peter A Clark

March 2000

INTERNAL REPORT NO.107

NWP Technical Report No.302

Joint Centre for Mesoscale Meteorology

Implications for Mesoscale Modelling from a Study of the FASTEX IOP 16 Mid-latitude Cyclone

Richard M. Forbes, Humphrey W. Lean,
Nigel M. Roberts, Peter A. Clark

Joint Centre For Mesoscale Meteorology
The Met. Office

Abstract

High resolution Numerical Weather Prediction models driven by larger scale information are used to add finer scale structure to model forecasts. Much of this structure in forecasts of mid-latitude cyclones developing over the North Atlantic is internally generated due to non-linear effects in the model dynamics and parametrized physics. This report investigates the development of mesoscale structure in such a mid-latitude cyclone from the Fronts and Atlantic Storm Track Experiment (FASTEX) using the Unified Model at mesoscale resolution. Intensive Observing Period 16 was characterised by a rapidly developing secondary wave cyclone and was observed with dropsondes and Doppler radar from two dedicated aircraft over an eight hour period. The developing system is described in detail from observations and compared with model forecasts and analyses. Emphasis is placed on the sensitivity of the forecasts to initial conditions, horizontal and vertical model resolution, and the parametrization of ice microphysical processes. Results from the resolution and microphysics sensitivity experiments show a systematic impact on the mesoscale structure which may have general implications for operational modelling.

Index

1. Introduction

High resolution NWP models have to be driven by larger scale information, usually derived from coarser resolution models. They are thus used, in practice, to add finer scale structure ('detail') to the larger scale information. For the purposes of this report we shall use the term 'mesoscale' to refer to such higher resolution models, though strictly the coarse resolution model may be resolving some mesoscale features. Added detail arises from three sources:

1. Increased detail in ancillary fields contributing to diagnostics, such as land surface type.
2. Finer scale forcing from boundary conditions, primarily the surface boundary condition in the form of orography and surface characteristics.
3. Internally generated structure due to non-linear effects in the model dynamics and parametrized physics. Often this takes the form of flow instabilities.

Many assessments of mesoscale models have been dominated by the first two of these factors, and much skill has been demonstrated in predicting impacts from higher resolution surface forcing. Somewhat less attention has been paid to the inherent accuracy of internally generated structure. Experience suggests that models may be rather less successful in this area. This is probably an inevitable effect of the instabilities involved. Idealised scenarios may be used to study these phenomena, but it is clearly impossible to validate the results against observations. Systems which develop entirely over the sea within the model domain approximate the ideal of being purely driven by internal processes. The only significant specified surface boundary condition is the sea surface temperature (SST). In practice, we rarely have accurate, time-varying values of SST on the mesoscale even if structure on this scale were significant.

The mesoscale structure of extra-tropical cyclones is a good example of internally generated structure. The Fronts and Atlantic Storm Tracks Experiment (FASTEX) provided a number of high quality observational data sets concentrating on cyclone development over the northern Atlantic. This report concentrates on one Intensive Observation Period (IOP 16), during which a weak trough to the west of the Atlantic developed, over roughly a 12 hour period, into an intense secondary cyclone to the north west of Scotland. The mesoscale structure of the cyclone was well observed using airborne Doppler radar, dropsondes and *in-situ* aircraft measurements. The cyclone was associated with severe weather, in the form of strong winds, heavy rain and low cloud, and so is of forecasting interest in itself.

The primary intention of this report is to investigate how aspects of the model formulation and configuration influence the development of mesoscale structure within the system, with a view to establishing those aspects which could usefully and practicably be improved. The report covers the current formulation of the Unified Model (UM), in particular the split explicit Eulerian hydrostatic dynamics. A future report will compare results with the new semi-implicit semi-Lagrangian non-hydrostatic dynamics. Furthermore, while data assimilation will be touched upon, impact of and improvements to the assimilation scheme will not be covered. It will, however, be shown that the initial conditions are a dominant component in the subsequent development, so the case would form a useful case study for data

assimilation systems. While we concentrate on one case, we intend to consider results in as general a way as possible.

Section 2 of the report outlines the available observations and their interpretation. The intention here is not to give a full analysis of the system structure and evolution. Instead, we identify those features of primary importance which may be used to assess model performance. Section 3 provides an overview of larger scale model runs that were performed operationally and subsequently, in order to put the mesoscale structure developed in higher resolution simulations into perspective. Section 4 discusses a number of mesoscale runs leading to a 'reference' simulation we regard as approaching the best possible with the current model formulation and computer power. Section 5 presents an investigation of model sensitivity. Earlier work has lead us to believe that the most important model processes, in this case, are the model dynamics itself and the interaction with diabatic forcing due to layer cloud processes, especially those involving ice. We have thus concentrated on the impact of model resolution and aspects of the ice microphysics parametrization. Section 6 builds on these results to highlight the areas where changes to model formulation would be expected to have an impact, and the nature of that impact.

2. Case Study Description from Observations

2.1 The Observations

We make use of measurements taken between 05Z and 13Z from the UK C-130 and the NOAA P3 aircraft. The C-130 flew at an altitude of around 8km and released dropsondes into the cyclone. The P3 flew at an altitude of around 2km and was fitted with Doppler radar. Both had additional instruments on board to take flight level measurements.

The two aircraft, flying roughly the same track, systematically mapped out the whole cyclone with six flight tracks (legs) perpendicular to the direction of travel of the system. Figure 2.1(a) shows the flight pattern of the C-130 superimposed on the 09Z Meteosat infrared image. The track has been spread out relative to the moving system to take account of the system velocity and gain a snapshot picture. This is a reasonable thing to do if the system velocity is nearly constant, the cyclone does not evolve (change shape) too rapidly and the flight time is not too long relative to the evolution of the system. In this case, it is the nature of the particular features of interest within the cyclone that determine whether such considerations are important.

Satellite imagery was available from Meteosat every half-hour from the infrared channel and every hour from the water vapour and visible channels. There was sufficient daylight for the visible imagery to be useful between 09Z and 16Z.

2.2 General Development and Track

The storm that was observed during FASTEX IOP16 was a rapidly deepening frontal-wave cyclone that developed in a pre-existing baroclinic zone. The start of the development of the low from a trough was observed through the emergence of a cloud head at 02Z from beneath the upper-level cloud band marking the jet stream. Figure 2.1(b) shows the track of the cyclone from 03Z when it was at the trough stage, through to the well-developed system revealed by the infrared image at 12Z.

We have utilised radar altimeter measurements of surface pressure from the P3 and dropsonde wind measurements from the C-130 in conjunction with satellite imagery and synoptic observations to determine the location and central pressure of the low at 09Z and 12Z (synoptic measurements only) (see Table 2.1). At earlier times the position of the cyclone was difficult to locate accurately because the low centre was not closed (in pressure contours) and observations were sparse.

	Surface Pressure (hPa)	Latitude, Longitude (degrees)	Estimated positional uncertainties
09Z	967.5 +/- 1.0	54.5 N, 18.0 W	+/- 60km along NE-SW +/- 30km along NW-SE
12Z	963 +/- 2	56.5 N, 13.0 W	+/- 60km

Table 2.1 Location and central pressure of the surface low

2.3 Cloud Head Evolution

2.3.1 Cloud Head Definition

A cloud head is defined here as the layer cloud that emerges from beneath the cold-air side of the main polar-front cloud band (PFCB) during baroclinic cyclone development. Cloud heads are characterised by a sharp outer edge in infrared imagery. As they grow and extend away from the PCFB they often develop into the distinctive hook shape associated with well-developed cyclones. The emergence of a cloud head is the result of cross-frontal slantwise ascent of air originating both in the warm sector (warm conveyor belt) side and the cold side of the thermal gradient (Browning and Roberts 1994).

2.3.2 Cloud Head and System Velocity

Since cloud heads are a manifestation of the ascent associated with a developing cyclone, they remain in the same position relative to the deepening low centre. An estimate of the velocity of the low can be found by using Meteosat infrared imagery to track the centre of the cloud head once it has clearly emerged from beneath the PFCB. Evolution of the shape of a cloud head and the gradual transition, during a system life cycle, from ascent on the warm-air side to ascent on the cold-air side reduce the validity of this method, but it is still a reasonable measure. A satisfactory estimate of system velocity is essential so that we can position dropsonde measurements accurately relative to satellite imagery and construct a system-relative 3-dimensional picture of the primary flows associated with the developing cyclone. Table 2.2 shows the system velocity at 06, 09 and 12Z.

Time (UTC)	Direction system is moving from. Bearing from north. (degrees) (+/- 3)	System speed (m/s) (+/- 3)
06	243	39
09	233	29
12	222	23

Table 2.2 System velocity.

2.3.3 Multiple Cloud Heads and Cross-frontal Circulations

A characteristic of the IOP16 cyclone (as with many others) was the multiple cloud head structure observed in the satellite imagery. Three separate cloud heads could be seen emerging from beneath the PFCB during the period when the C-130 and P3 aircraft were flying. The water vapour imagery sequence in Figure 2.2 shows the three cloud heads, which are identified by the letters A, A2 & B.

Diagnosis of dropsonde measurements allowed us to relate cloud heads A & B to distinctly separate and coherent cross-frontal ascending flows that were stacked one on top of the other (B on top of A), with weaker ascent or even descent between. Cloud head A2 was associated with the same cross-frontal flow responsible for cloud

head A, but became visible as a 'new' cloud head emerging from beneath the SW edge of cloud head B as the developing storm became more wound up. The flow feeding a fourth cloud head (cloud head C beneath cloud head A2) could also be identified from a few dropsonde measurements; although cloud head C could not be easily distinguished as a separate entity in satellite imagery.

Streamlines of the system-relative flow pattern that fed into cloud heads A/A2 & B are shown in Figure 2.3. Characteristics of each of the four cloud heads are described below with references to Figures 2.4 & 2.5. Figure 2.4 shows a cross-section perpendicular to the thermal wind that reveals primarily the flow into cloud head A. Figure 2.5 is a schematic of the multiple cloud head evolution of the whole system.

a) Cloud heads A & A2

Cloud heads A and A2 were the result of rearward slantwise ascent from the warm/cold front through the low centre (frA in Figure 2.5). Cloud head A was fed from the section of the front ahead and through the low centre when below the PFCB; cloud head A2 was fed from the section of the front behind and through the low centre when no longer beneath the PFCB. The emergence of cloud head A coincided with the appearance of the strip of reduced cloudiness in the PFCB (RCS in Figures 2.2 & 2.5).

Figure 2.4 shows the precipitation core at the front (labelled A) extending up to 770hPa and the slanted region of precipitation within and beneath the flow feeding cloud head A (black arrow). Beneath the slantwise ascent is a compensating slantwise descending flow (grey arrow), which was probably enhanced by sublimation/evaporation of precipitation. On the warm-air side (to the right) of front frA is labelled a region of middle-level divergence (in the two dimensions of this section) located between the ascent into cloud head A and the flow beneath cloud head B (dashed grey arrow). The low/zero radar reflectivity above the divergence maximum is indicative of descent and was aligned directly below the strip of reduced cloudiness in the PFCB. Quantitative measurements of cloud heads A and A2 are shown in Table 2.3. The estimate of vertical velocity is an average taken from the dropsonde measurements available, which assumes that isentropic surfaces have a constant slope throughout the system and with time (also for Table 2.4). In fact isentropes slope more steeply towards the rear of the cyclone and the slopes probably do change as the system evolves.

Time of emergence of cloud head A from beneath the PFCB	02Z
Time of emergence of cloud head A2 from beneath cloud head B	10Z
Speed of the outer edge separation of cloud head A from the PFCB	$12ms^{-1}$ +/- $2ms^{-1}$
The θ_w of the moist slantwise ascent into cloud heads A & A2	9 - 10.5°C
The slope of the cloud head flow	~ 1/50-70
Difference in speed between the cross-frontal flow component ascending into the cloud head and descending beneath	~ $10ms^{-1}$ +/-$5ms^{-1}$
Estimated vertical velocity of slantwise ascent	~$15cms^{-1}$+/-$5cms^{-1}$

Table 2.3 Quantitative measurements of cloud heads A & A2

b) Cloud head B

Cloud head B was the result of rearward slantwise ascent from a second frontal zone, parallel to and on the warm-air side of the first (front frB in Figure 2.5). Figure 2.4 shows the flow (dashed arrows) and precipitation (labelled B) associated with cloud head B, at the early stage when the cloud head had not yet emerged from beneath the PFCB. At a later stage cloud head B was stacked on top of cloud head A and extruded from beneath the edge of the PFCB more rapidly. Table 2.4 shows the quantitative measurements of cloud head B and Table 2.5 shows the relationship between cloud heads A/A2 and B.

Time of emergence from beneath the PFCB	06Z
Speed of the outer edge separation from the PFCB	$20ms^{-1}$ +/- $2ms^{-1}$
The θ_w of the moist slantwise ascent into cloud head	11.5 - 13°C
The slope of the cloud head flow	~ 1/120
Difference in speed between the cross-frontal flow component ascending into the cloud head and descending beneath	~ $13ms^{-1}$ +/-$5ms^{-1}$
Estimated vertical velocity of slantwise ascent	~ $8cms^{-1}$ +/-$4cms^{-1}$

Table 2.4 Quantitative measurements of cloud head B.

Vertical separation between ascending flows	~ 2 -3km
Horizontal separation between fronts frA and frB	~200km

Table 2.5 Relationship between cloud head A/A2 and B.

c) Cloud head C

Cloud head C was mostly concealed below cloud head A2 and associated with the ascent from a third frontal zone (frC in Figure 2.5) on the cold side of frA during the later well developed stage of the cyclone. The evidence for this cloud head comes from only a few dropsondes, so there is insufficient information to determine the slope and magnitude of the cross-frontal flow, but we can find the θ_w of the moist ascent (Table 2.6). We are unable to say, on the basis of the observations, whether front frC pre-existed cloud head C or was created in situ, but it is likely that frontal intensification occurred as the cloud head developed.

The θ_w of the moist ascent into cloud head	6 - 8°C

Table 2.6 Quantitative measurements of cloud head C.

2.4 The Low-level Jet and Frontal Zone frB

Dropsonde measurements from the later flight tracks 5 and 6 revealed a low-level wind speed maximum within the warm air ahead of the cold frontal section of frontal zone frB. This low-level jet core (Fig. 2.6) was located at a height of around 1.2km (850hPa) with wind speeds of between 42 and 46m/s. Above this maximum, a minimum in wind speed of between 34 and 39m/s was observed at a height of around 1.7km (740hPa).

The part of frontal zone frB that was observed in Figure 2.6 was complex. The radar reflectivity shows two precipitation cores 60km apart; one at 360km along the section and extending up to 700hPa; the other 300km along the section, more intense and extending up to 650hPa. It is likely that the more intense core was the main Narrow Cold Frontal Rainband (NCFR) that fed cloud head B and the other core was a weaker pre-frontal rainband. There were no dropsonde wind measurements (only temperature measurements) between the two precipitation cores, so we are unable to say whether the low-level jet existed in that region, or only to the right of the core at 360km. The flow into cloud head B could be identified as a maximum in the along section, right to left, wind component and a minimum in the absolute wind speed which coincided with the top of the two precipitation cores. This rearward flow broke up into middle level convection (lumpy appearance in reflectivity) as the moist ascending region was overrun by lower-θ_w air associated with the dry intrusion at the back of the cyclone. The minimum in wind speed also extended slantwise downwards from the top of the precipitation cores into the warm air as the region which separated the low-level jet from the stronger winds at higher levels.

The cross-section in Figure 2.6 has allowed us to examine some of the details of the cross-frontal structure at a point on the front frB. We have much less information about along front variations, however there is sufficient observational evidence to conclude that the low-level jet, narrow frontal rainband(s) and mid-level convection existed along a significant length of the cold frontal section of front frB.

2.5 Upper-level Vorticity Anomaly

An upper level vorticity anomaly could be identified above 550hPa in dropsonde winds and from doppler radar, in runs 5 & 6 between 11Z and 12Z. The continuity of movement of a dark zone in the WV imagery (a signature of an upper-level vorticity anomaly), suggests that the vorticity anomaly was catching up the frontal wave and becoming coupled with the emergence of cloud head A2. The evolution of cloud heads A and B did not appear to be strongly coupled to this particular vorticity feature. Figure 2.2(d) shows the 12Z position of the upper-level vorticity anomaly at 500hPa.

3. Low Resolution Models

3.1 Introduction

The primary focus of this report is the representation of the case with high horizontal resolution models (approximately 12km). Some work has also been done at lower resolution (approximately 50km). This was partly motivated by the need to provide boundary conditions to drive the high resolution runs, but also to provide some information on the effect of model resolution. The work on low resolution models is briefly described in this section.

3.2 LAM

At the time of FASTEX the highest resolution operational model over the area of interest was the "Limited Area Model" (LAM) at 50km, 19 level resolution over a domain covering the North Atlantic and much of the surrounding land. For the purposes of this study, in order to get the required diagnostics, the operational output was not used but the model was rerun from the operational analysis and boundary files (although checks were made that the output was the same). The model was rerun at version 4.4 in as close as possible to the operational configuration at the time of FASTEX. The main physics schemes used were the 1B SW radiation code, the 1A Slingo and Wilderspin LW radiation scheme, the 3A standard implicit boundary scheme, 3A convection scheme with standard local buoyancy closure, 3A gravity wave drag scheme and the single phase precipitation scheme (2D). This last should be particularly noted since it is the old scheme with diagnosed ice as opposed to the newer scheme with prognostic ice used in the model configurations discussed in the rest of this report. (A test run of the LAM was in fact carried out with the new mixed phase precipitation scheme but it made very little difference to the results shown here). As with all the model data discussed in this report the model output was post processed with the MDIAG program (Panagi and Dicks 1997) to produce the various diagnostics required.

Figure 3.1 shows the representation of the IOP16 system by this model at 12Z from the 18Z and 0Z LAM runs. Overall the system, as represented by the surface pressure, appears to develop as expected in both simulations. It is important to note that the surface system is not developed at all by the start time of the forecast runs, being simply a sharp trough (Fig. 3.2). The system therefore develops entirely during the model forecast run. At 9Z the system centre is about 120km NE of the position analysed from the observations in the 18Z run with a similar, but somewhat smaller, error in the 0Z run (see Table 3.1). Similar positional errors are seen at 12Z. The system is, however, much weaker in the 0Z run. At the time of FASTEX this lead to the impression, which became accepted wisdom, that the 18Z run was a more accurate representation of the system than the 0Z one. It is difficult to rely too much on the central surface pressure of the system in order to verify the model since, in the case of a secondary cyclone such as this, it depends on the position and depth of the parent low and the system position relative to the parent low as well as the relative depth of the system of interest. With these reservations it is interesting that the depth of the system is within the error bars of the analysis for the 18Z run but about 8hPa too high in the 0Z run which appears to confirm the conclusion that the 18Z run is better. This

comparison, however, illustrates the problems with using the central pressure because over half this difference between the two runs is accounted for by a difference in the depth of the parent low.

Also shown in Figure 3.1 is the temperature of the topmost $2x10^{-5}$ kg/kg cloud ice concentration threshold which gives an approximate cloud top temperature i.e. an idea of what the IR image would look like. This threshold was chosen to make the cloud top temperatures similar to those estimated from the top of atmosphere outgoing long wave radiation diagnostic although the cloud top temperature charts obtained are not very sensitive to what threshold is used (which is encouraging from the point of view of their usefulness). Comparison of these figures with the observed IR image (Fig. 2.1(b)) shows that the model makes some attempt to represent the real cloud head although it is obviously severely limited by the 50km resolution. The cloud head in the 0Z run looks very weak which is consistent with the generally weaker nature of the system in this run – this tends to reinforce the idea that the 18Z run is a better representation. It is not clear from the IR imagery that the system is too far north east as mentioned above; this is likely to be another consequence of the poor representation of the cloud head due to the resolution.

It is interesting to note that the LAM runs have lower RMS differences from the sonde data than any of the mesoscale runs (Table 3.2) but this reflects the fact that the fields are lacking in any high resolution detail (as is well known RMS errors tend to be lower for not having a feature at all rather than having the feature but with a positional error – a wave with a phase error of 60° gives an RMS error equivalent to no wave at all). Cross sections taken through the LAM output show, in general, rather bland fields as would be expected from the relatively low resolution compared to the dropsonde data. In particular there is no sign of the multiple cross frontal circulations described in section 2.3.3 and, as is obvious from Figure 3.1, no sign of the multiple cloud heads. Despite the lack of detailed mesoscale structure, however, the overall evolution of the system with regard to surface pressure does not appear too bad.

3.3 High Resolution Global Model

At the time of FASTEX the operational Met Office models consisted of the approximately 100km resolution global model, the 50km LAM and the 17km UK Mesoscale. About a year later the LAM and global models were replaced by the "High Resolution Global model" with a grid size 432x325, which corresponds to a gridlength of 45km in the east-west direction at 60°N. It was felt important to rerun IOP16 with this model since it was the new operational model and also, since it is a 30 level model, it is expected to be better for driving the mesoscale model. This model was initialised by running with assimilation for 72 hours (starting from 12Z on the 13th) in order to obtain a genuinely high resolution starting point. These runs used similar physics options to the LAM but with the mixed phase (prognostic ice) precipitation scheme. Surprisingly the results were rather different from those obtained with the LAM. As can be seen in Figure 3.3/Table 3.1 for runs with an 18Z 16th data cut off the high resolution global representation has the system much weaker and differently positioned. As discussed in section 4.2 being weaker may not in itself indicate a bad forecast although the central pressure is now 6hPa too high. The low centre at 9Z 17th is somewhat closer to the analysed position than the LAM forecast (although still too far to the NE). It may be noted that the 12Z 16th high resolution

global run has the system again very weak (no closed isobars) but further to the north than the LAM (i.e. in this case the position is even more incorrect than the LAM).

It is clear that something is very different about the high resolution global reruns of this system. In order to investigate the reasons for the differences, experiments were carried out starting from a 50km LAM dump implanted into a 100km global dump. Figure 3.4 shows the system at 12Z 17th obtained by carrying out the implantation in the 18Z 16th analysis (very similar results are seen if it is done at 12Z). In this case the high resolution global model produces a very similar system to the LAM (albeit somewhat to the NE) which implies that the difference is with the analysis system rather than the model. This is confirmed by the result that if just one cycle of (global) assimilation is added to the 12Z LAM implantation run the system reverts to being extremely weak (Fig. 3.5). Figure 3.6 illustrates the difference between the 18Z analysis in the LAM implantation run plus one (6 hour) assimilation cycle with the 18Z LAM analysis. The southern trough which becomes the system is deeper in the LAM and the ridge ahead is sharper. The generally distributed nature of the difference field gives the impression that the difference is not simply due to one or two different observations. Investigation of the observations available in the two sets of runs reveals that satellite derived winds were not included in the global run. This is because, for the global runs, the OPS was unable to extract these observations from the MetDB, probably because they were not there. The reasons for this are under investigation although it is probably relevant that the operational runs would have used data from the old SDB which was subsequently replaced by the MetDB. Although it would seem likely that these differences in the observations assimilated account for the differences between the global and LAM models it is also possible that there are contributions from differences in the assimilation system (e.g. different correlation scales or filtering of observations). It should be noted that relatively few observations were available in the region of interest being mostly aircraft and satellite data. Further studies are required to establish the roles of the assimilation system and different observations in these runs.

3.4 ECMWF Initialised Runs

Runs of the High Resolution Global model were also carried out starting from ECMWF analyses. In general the system develops much less rapidly in these runs compared to the corresponding LAM runs (but about the same as the High Resolution Global) – the central pressure is about 4hPa too high by 9Z but the system position is better than from the UM analysis agreeing with the observational analysis within the error bars. These runs are consistent with the LAM in the sense that comparison of the system in the 18Z and 0Z runs shows little change in system position but a marked weakening of the system. The main conclusion from these runs is, again, that the system is very sensitive to initial conditions.

Table 3.1 Summary of the cyclone characteristics for the low and high resolution model runs.

	9Z central pmsl (hPa)	9Z centre position	9Z centre position error (km)	12Z Number of 1hPa closed isobars	No of cloud heads (12Z)[1]	Cross frontal circulation velocity at 9Z (m/s)[2]	Cross frontal vertical shear between maxima of opposing flows at 9Z (m/s/100hPa)[2]	θw (C) of cross frontal circulations[2,3]	Slope of slantwise flows into cloud heads[2]
Observations	**967.5±1.0**	**54.5N,18W**	**0±60**	-	**3**	**10±5, 15±5**	**32±8, 32±8**	**9-10.5, 12-13, (6-8)**	**~1/60, ~1/120**
18Z LAM	967.8	55.5N, 16.2W	120±60	3	1	17.5±1	10	10±1	~1/40
0Z LAM	973	55N, 16W	80±60	1	1	10±1	10	10±1	~1/40
18Z HRG	973.2	53.9N, 17.3W	70±60	1	1	18±1	10	9-11	~1/40
HRG from 18Z EC	971.5	54.7N, 17.9W	20±60	1	1	10±1	10	9-11	~1/40
0Z Meso	969.8	54.2N, 17.8W	30±60	1	2	16±1, 14±1	32	(5±1) 8±1, 11±1	~1/40,~1/80
18Z Meso	964.0	54.2N, 16.7W	50±60	5	1	10±2	30	(5±1) 9±1	
Meso from 18Z HRG	972.0	54.5N, 17W	30±60	1	1				
Meso from HRG from 18Z EC	973.0	53.0N,56.5W	170±60	1	1				
Meso anal with sondes	964.5	54.6N, 17.7W	10±60	3	1	16±1, 12±1	30	11.0±0.5, 13.0±0.5	~1/35
Meso anal without sondes	965.2	54.5N, 17.9W	0±60	3	1	16±1, 12±1	30	11.0±0.5, 13.0±0.5	~1/35
Meso from 18Z LAM (45LEV24)	966.0	56.06N 15.3W	190±60	4	2	15±1, 10±1	30	8±1, 11±1	~1/50

Notes:

1. Number of cloud heads on distinct isentropic surfaces
2. Where more than one number appears each refers to a separate circulation
3. Values in brackets are for less clear circulations

Model Run	Temperature (°C)		Rel. Hum. wrt Water (%)		Wind magnitude (m/s)	
	Mean	RMS	Mean	RMS	Mean	RMS
18Z LAM	-1.9	2.5	-3.3	16.5	-1.2	4.7
0Z Mesoscale	-1.3	2.0	-5.4	22.8	-0.8	6.0
18Z Mesoscale	-1.7	2.4	-9.7	26.3	-0.8	6.6
Meso analysis (with sondes)	-0.5	1.1	-2.3	18.5	-0.4	4.8
Meso from 18Z LAM analysis	-1.2	2.1	-7.3	23.7	-0.4	6.0

Table 3.2 This table shows the mean difference and RMS difference between the model runs and the sonde data calculated for time windows 60 mins either side of 6Z,9Z and 12Z on the 17th for the quantities listed.

4. Mesoscale Model

4.1 Introduction

This section describes the work on rerunning the IOP16 case with mesoscale (12km) resolution versions of the Unified Model. Since the standard UK mesoscale model domain does not cover the area of the Atlantic of interest this work required the definition of new domains and finding the best way to initialise the model from the low resolution model data and the observations available. Section 4.2 describes the model configuration and section 4.3 gives an overview of the results. Some problems encountered with the model are described in section 4.4, section 4.5 discusses the likely mechanism for the cross frontal circulation, section 4.6 describes mesoscale runs from other initial conditions and section 4.7 describes the results of running the model forward with assimilation to obtain analyses.

4.2 Description

The main requirement for the mesoscale runs was to capture as much as possible of the development of the system within the domain of the model. Two associated needs were to have minimal spinup effects during the period of interest and to minimise the influence of the low resolution boundary conditions on the evolution. This section describes the configurations of the model used to address these aims.

The Unified Model was run at version 4.5 with physics as close as possible to that used operationally at the time of FASTEX. The physics and dynamics timesteps were both halved from the operational values to 2.5 mins and 30s respectively for reasons discussed in section 4.4.1. The physics sections were equivalent to those used in the LAM except for gravity wave drag being switched off, 3C convection and the inclusion of the 3B mixed phase precipitation scheme with prognostic ice as described by Wilson and Ballard (1999). All the runs described here used the AC assimilation scheme (which was the operational scheme at the time of FASTEX). The horizontal resolution used was 0.105 degrees which is very close to the 0.11 degrees used operationally and represents a spacing of approximately 12km. The horizontal grid was a non-standard rotated lat-long grid as described below. The sea surface temperature and also the orography and other land based ancillary fields were interpolated from the 50km data. This means that these fields are rather smoother than they could be at 12km resolution but this was not considered important since the SST was not expected to have much structure on shorter scales than 50km and the various land fields do not have too much effect in this case since the development of interest takes place over the ocean.

The early runs used the standard operational set of 38 mesoscale levels in the vertical but most used a 45 level set which gave a much more constant spacing through the mid troposphere (see Fig. 4.1). This change was motivated by interest in ice processes in the mid troposphere where the maximum spacing of the 38 levels is over 50hPa, the 45 levels bring this down to about 25hPa. The increase in vertical resolution from 38 to 45 levels did significantly improve the representation of certain aspects of the mesoscale structure of the system. The impact of changes in vertical resolution from 38 to 45 to 70 levels is discussed in detail in section 5.3.2.

Since the mesoscale model was not operational at the time of FASTEX over the area of interest an important question was how to initialise these reruns. The early runs in this study were initialised from a T+3 50km LAM forecast dump at 21Z. This allowed the use of the 18Z LAM run which was thought to be the best one but the start at 21Z (rather than 18Z) allowed a somewhat smaller domain to be used which still contained the precursor trough. It is important to note that since IOP16 was a relatively fast moving system the domains used were simply determined by the desire to keep the system within the domain (and not too close to the edges) for the time of interest – hence the shorter runs allowed smaller domains. Although the models initialised from the T+3 LAM in this way produced reasonably good representations of the system they suffered from spin up problems in that it took 6-9 hours for the initial fields at 50km resolution to develop high resolution structure.

In order to obtain a high resolution representation of the system without spin up problems the model was initialised from a 50km LAM dump at 9Z on the 16th and run forward with assimilation until the data cut off time (18 or 0Z in the runs described here). The main drawback of this approach was that a large domain was required in order to keep the system within the model from 9Z until 12Z the following day. This domain is shown in Figure 4.2 and had a size of 394x247 (the total number of 3D gridpoints in this model is comparable to the high resolution global model which is close to the limit of what may be handled with current computer resources). The runs described in the next section were initialised in this way.

The boundary conditions for these runs were either generated by a LAM forecast run from 9Z or generated from the operational LAM dumps at 3 hourly intervals. The difference between these two approaches is discussed further in the following section.

4.3 Results

Figure 4.3 shows 12Z pmsl and cloud top temperature charts for the 12km, 45 level runs with data cut off times of 18 and 0Z using operational LAM boundary conditions. It should first be noted that the results are consistent with the LAM results in the sense that as the data time moves forward the system stays in approximately the same position but weakens. However it now appears that the 0Z run, although it still has a weaker system has the most realistic looking cloud heads. In the 18Z run the cloud heads look overdeveloped and the dry slot is correspondingly too prominent (this is still the case in the 0Z run but less so). In addition the area in front of the cloud head (the leading edge) is represented better in the 0Z run. As a result of this the rest of this section will relate to the 0Z run.

We now look in more detail at various aspects of the results. Starting with the large scale features, the overall development of the system appears to be good with the system appearing to be reasonably placed compared to the satellite imagery. At 9Z the centre of the surface system is at 54N,17.75W which agrees, within the likely errors, with the analysed position given in Table 2.1. Similar consistency with the observations is seen at 12Z. This agreement represents a significant improvement over the LAM forecasts discussed in section 3.2 (Table 3.1). The central surface pressure of the low is about 2hPa above what is seen in the observations at both times. The shape of the cloud shield appears to be generally good although the cloud shield seems to have the wrong curvature in some places. The use of boundary conditions

generated from the operational 50km analyses appears to improve some aspects of this, for example the curve in the cloud shield edge at the front of the cloud head at 12Z (Fig. 4.4) is more correctly represented. However the incorrect curvature at earlier stages is apparently due to the over development of the system and is not affected by the boundary conditions.

A double frontal structure is very noticeable in the earlier stages of the development of the model system and can be seen clearly in a number of diagnostics, including cloud ice and, as shown in Figure 4.5, the 800hPa vertical velocity. This corresponds to a double trough structure in the initial fields (similar to that shown in Figure 3.2). This double feature is also present in observational data. Figure 2.4(b) shows the radar reflectivity in a cross section perpendicular to the fronts and Figure 4.6 shows a similar cross section through the model data. Detailed comparison with the observations is difficult because the model variables do not directly correspond to the radar reflectivity however the double frontal structure seen in the radar data is clearly similar to the double structure seen in the model. It can also be seen in Figure 4.6 that the double vertical velocity features correspond to double cross frontal circulations which look similar to the multiple circulations seen in the observations (section 2.3.3).

From Figure 4.3 it can be seen that the model makes a good attempt to represent the double nature of the observed cloud head. Furthermore, as is the case with the observations, it can be shown that the two circulations correspond to the two cloud heads. The flows have again been analysed on isentropic surfaces chosen to be those on which the cross frontal flow velocities are greatest. Figure 4.7 shows the cloud head at 9Z and how it can be split into components on the 8 and 11C θ_w surfaces. The cloud ice on the 8C θ_w surface corresponds to the rearward cloud head and that on the 11C θ_w surface the forward one. Also shown on the plots are the system relative velocities on the two surfaces and it can be seen that the general direction and curvature of the flows into the cloud heads correspond well to what is seen in observations (Fig. 2.3(a)). The main difference is that in the observations the cloud heads are at 10 and 12C values of θ_w which implies that although the model has the right type of cloud head development it is taking place in the wrong places relative to the θ_w structure. It should, however, be noted that the mean temperature in this run is 1.6 degrees below that seen in the dropsondes (Table 3.2); this overall bias is consistent with this difference in the θ_w values. Although the double cloud head looks qualitatively good overall, it is wrong in detail. Both cloud heads are larger than they should be and the dry slot is too pronounced. Also it is noticeable that the relative size of the secondary and primary cloud heads is wrong with the secondary cloud head (i.e. the western most one) being larger in the model but smaller in the observations.

Figure 4.8 shows that the model represents well the low level jet which was discussed in section 2.4 – an along front velocity maximum is seen just on the southern side of the southernmost front. The magnitude of this jet at 42m/s is similar to that seen in the observations and the height of the jet maximum (850hPa) is also in good agreement.

To summarise, the mesoscale forecast runs of IOP16 appear to give an encouragingly good representation of the system. Much of the mesoscale structure observed in the observational dataset is seen in the model runs although there are some important differences in the details.

4.4 Model Problems

This section briefly describes some problems encountered with the model in the course of these reruns.

4.4.1 Boundary Waves

When work on these runs was started spurious wave like structures were seen in a number of fields emanating from the boundaries of the model. This phenomenon is most noticeable as a checkerboard pattern in the vertical velocity field (Fig. 4.9) or as wiggles in the pmsl. It was found that they could be eliminated by halving the timesteps (both dynamics and physics) from the usual operational value (1 minute dynamics timestep, 5 mins for physics). J. Radcliffe (pers. comm.) has found that these waves can also be eliminated by the use of 8 point rather than 4 point boundaries. This solution is now used operationally in the UK mesoscale model but this turned out not to be possible with the large domain used in this work due to computing constraints. In practice, solutions with half timestep looked very similar to those without (apart from the boundary waves) but it should be borne in mind that there is, in principle, some timestep dependence present in the model physics and dynamics.

4.4.2 Break up of Slanted Structures

Another problem with the model representation which was encountered is illustrated in Figure 4.10 which shows the vertical velocity along a cross section perpendicular to the aircraft sections (i.e. along the front) in a run initialised from the 21Z 50km T+3 forecast. It can be seen that there is a slanted structure which is, probably unphysically, broken up into separate maxima. This sort of feature was described by Persson and Warner (1991) who saw similar looking effects in a simulation of conditional symmetric instability (CSI) and ascribed it to the effect of trying to represent a slanted structure on a finite grid. The cores of the maxima correspond to the model levels (except at the lower levels) in agreement with this idea. The generation of spurious gravity waves by these structures is minimised by increasing the vertical resolution with respect to the horizontal – Persson and Warner show that the aspect ratio of the grid should be of the same order as the slanted structure being represented. For the structure illustrated this implies that for 12km resolution the levels should be spaced closer than 10hPa which implies more than 100 levels, more than were used in any of these runs. It should be noted that the case illustrated was with a run using the operational timestep (5 mins) and the problem is reduced, but not eliminated, when the timestep is halved as it was in most of the runs discussed here.

4.5 Mechanism for Circulations

Figure 4.11 shows a cross section of the PV structure corresponding to Figure 4.6. It can be seen that there is a good deal of diabatically generated PV – positive in the regions of ascent and negative at higher levels being advected in the circulations. The double circulation corresponds to a double tropopause fold structure. An interesting question is what is responsible for the circulations. Given the significant amount of negative PV (and moist PV) observed one might expect the atmosphere to be unstable to CSI and, indeed, a SCAPE calculation (Shutts 1990) shows that there is a large

amount of SCAPE present. However calculations of the frontogenesis function show that frontogenesis is taking place and so these circulations could be simply frontogenesis circulations forced by large scale dynamics. It is interesting to note that the double vertical velocity structure (as shown in Figure 4.5) fits extremely well with that predicted by the QG omega equation diagnostic (inverse Laplacian of div-Q) which implies that large scale forcing is important. As discussed by Thorpe and Emanuel (1985) it may be difficult to distinguish which of the two mechanisms frontogenesis or CSI is responsible for the circulations. In addition there is also evidence that the circulations are strongly enhanced by diabatic cooling due to the evaporation of ice. This will not be discussed any further here since it is the subject of section 5.4.2.

4.6 Mesoscale Runs from other Initial Conditions

In this section the results of running the mesoscale model in the configuration discussed in 4.1 from other initial data are briefly discussed. An overview of these results may be seen in table 3.1.

4.6.1 High Resolution Global

A 12km mesoscale run has been carried out driven from the 18Z high resolution global run described in Section 3.3 (Fig. 4.12). The system centre is ill defined and although correctly positioned to within the observational errors looks very weak in pmsl. The cloud head size is about the right size although the dry slot is again too prominent and there is no sign of splitting

4.6.2 ECMWF Analyses

The 12km mesoscale model was also run from ECMWF analyses at 12 and 18Z using boundary conditions obtained from a High Resolution Global model run. The results are shown in Figure 4.13 and are somewhat similar to the results from the high resolution global analysis driven run discussed in the last section. Once again the system appears weakened without any sign of splitting in the cloud head but too far to the south east (Table 3.1).

4.6.3 ARPEGE Analyses

Mesoscale runs have also been carried out direct from ARPEGE analyses interpolated to a regional 0.4° grid. These runs are less comparable to those above since they used a different (smaller) domain, a different set of levels and 24km resolution. It is, however, interesting to note that the central pressure is in agreement with the observations at 9 and 12Z but the position is about a degree too far NW at 9Z and several degrees in the same direction at 12Z. Similarly to the runs from ECMWF data the cloud head appears smaller and without any sign of splitting.

4.6.4 Summary of Runs from different Initial Conditions

In summary, it can be seen that the effect of different initial conditions is to make big changes to the system which the model develops. This highlights the importance of the analysis system in producing good forecasts in cases such as this. This is not

surprising since a rapidly developing system would be expected to be very sensitive to initial conditions. The common factor is that all the runs discussed in this section have relatively weak systems compared to the runs carried out using assimilation in the 12km model – since those runs appear to have the system overdeveloped this could be regarded as more realistic.

4.7 Mesoscale Analyses

This section briefly discusses the results of continuing the assimilation in the 12km, 45 level mesoscale model right up to 12Z including (and excluding) the FASTEX sondes themselves. The motivation for doing this was to see how well the analysis at this resolution compares to the observations; it is not clear, for example, how well the assimilation system can cope with relatively closely spaced observations such as from the FASTEX dropsondes. It needs to be stated at the outset, however, that the results reported in this section should be regarded as preliminary – one set of runs have been done carrying the mesoscale assimilation forward until 12Z. A more thorough study would be possible investigating the effects of varying various assimilation parameters and repeating the work with the now operational 3D VAR scheme and, when possible, 4D VAR.

The model runs described in this section were carried out on the large 394x247 domain (Fig. 4.2) by running the model forward until 12Z with assimilation. All the FASTEX dropsondes whose data were transmitted to the GTS were included in the assimilation. This is in contrast to the LAM runs in which many of the dropsondes were rejected by the Observations Processing System. Presumably at 50km resolution many of the observations which were closer together were interpreted as inconsistent and rejected – this problem did not arise at 12km resolution.

Figure 4.14 shows the 12Z analysis from this run and, for comparison the analysis from a run which excluded the observations from the FASTEX dropsondes. Both these runs look rather different from the 0Z forecast (Fig. 4.3) showing that including observations up to 12Z has a big impact on the system. In addition the analysis including the FASTEX dropsondes is different from that without. Table 3.1 shows that the surface low is close to the analysed position in both cases (although there are significant differences between the two). The analysis including the FASTEX sondes has a central pressure of below 962hPa which is in marginal agreement with the observational analysis at the low end of the estimated errors. The analysis without the FASTEX data has a central pressure which is lower still (below 960hPa).

The analysed cloud top temperature charts (both with and without the FASTEX data) look very different from the T+12 forecast. Both have a more realistic looking cloud head shape (with splitting) and are less overdeveloped than the forecast. The inclusion of FASTEX sondes further increased the realism of the cloud pattern compared to the analysis without sondes. However, although each analysis improves the shape of the cloud heads, the associated cross-frontal flows appear somewhat less distinct and coherent and more difficult to relate to the model cloud ice (diagnostic used to visualise the model cloud head(s)) than in the T+12 forecast (see Figure 4.15). The analysis including FASTEX dropsondes is slightly worse in this respect. Despite this, the cross frontal flows in the analysis are closer to the observed isentropic surfaces than those in the forecast (table 3.1), with the analysis including the dropsondes the

closest. However in this case the southern (warmer) circulation is producing virtually no cloud head.

The RMS errors between the analyses including the FASTEX sondes and the sonde observations are lower than in any other case at 12km resolution (Table 3.2) which is encouraging in the sense that the assimilation is, indeed, improving the overall fit to the observations. For the analysis excluding the FASTEX sondes the RMS errors are generally larger but still rather less than for the forecast. In the light of the low RMS errors, the fact that the mesoscale structure in both analyses appears less clear as regards the cross-frontal flows associated with the cloud heads than in the forecast could be viewed as surprising. One possible explanation is that there is a positional error between the model and observed mesoscale features which results in the observations smearing out the structure. It also needs to be remembered that the horizontal correlation lengths were set to the standard value of 61km when some of the sondes were 40km apart so its to be expected that some of the structure would be smeared out for that reason. The fact that, of the two observed cross frontal circulations one does not appear to be producing a cloud head could be a consequence of winds being nudged into the model by assimilation and the cloud ice not having had a chance to become consistent with it. In fact the ice distribution looks more consistent with the circulations at 12Z than at 9Z which encourages this view. As mentioned earlier further work would be desirable in order to answer these questions. This case could provide a useful test bed for understanding the behaviour of the assimilation system – in particular with closely spaced observations.

5. Sensitivity to Grid Resolution and Cloud Microphysics Parametrization

5.1 Introduction

One approach for finding deficiencies in the formulation of numerical weather prediction models is to look at the sensitivity of the model to changes in the formulation and to assess the impact of these changes on the forecast. This could be, for example, a change of a major component of the model (e.g. the dynamics advection scheme), a change to the resolution of the model, or a modification of particular parameters in one particular parametrization scheme. The number of degrees of freedom in a typical NWP model is vast, but only a limited number of model sensitivity integrations can realistically be performed so the changes to the model need to be chosen carefully. It is possible to use the model adjoint equations to perform a sensitivity analysis for model parameter changes (Courtier and Rabier 1995) and this is now feasible for complex NWP models with the advent of methods such as four-dimensional variational assimilation (Talagrand and Courtier 1987). Such a method is not yet available for the Unified Model, but useful information can be gained from a series of model forecasts in which parts of the model formulation are modified. Any trends in the sensitivity of the model can then be identified. Changing a particular model parameter may improve or degrade the model forecast, but understanding the sensitivity of the forecast to parameter changes is of key importance.

Section 4 highlighted the fact that the model has a large sensitivity to initial conditions. A further aspect of the model formulation that is of particular interest for future mesoscale models is the sensitivity to horizontal and vertical grid resolution. The current operational mesoscale model has 38 levels with a mid-troposphere resolution of about 50hPa. One issue is whether this is high enough resolution to resolve the important processes associated with the development of mesoscale structure in mid-latitude cyclones, particularly those processes associated with cloud.

The second issue is the sensitivity of the development of mid-latitude cyclones to various aspects of the physics parametrizations in the model. The focus of this report is on short range forecasts of mid-latitude cyclones developing over the ocean and these systems are generally dominated by large scale cloud processes. The importance of sub-grid scale convection associated with the developing frontal zones is small relative to the resolved scale cloud from large scale ascent; less than 10% of the total rainfall in the model simulation of IOP 16 is due to the convective parametrization. Whether this is a correct proportion is open to question and requires further study. The boundary layer parametrization is also expected to have a relatively small impact on the mesoscale structure, as the system develops entirely over the ocean and only large scale gradients are represented in the sea surface temperature field. The sensitivity of the system evolution to the radiation parametrization is also expected to be small. Thus, the sensitivity to parameters in the large scale cloud and precipitation microphysics parametrization are of particular interest.

Section 5.2 describes the model used in the sensitivity experiments. Section 5.3 looks at model sensitivity to horizontal and vertical resolution and section 5.4 looks at sensitivity to cloud and precipitation microphysics parameters.

5.2 Model Description and Forecast Evolution

5.2.1 Model Description

The sensitivity studies were performed with version 4.5 of the Unified Model with the same dynamics and physics options for the mesoscale model runs described in section 4.2. In particular, the model included the 3B version of the mixed-phase precipitation microphysics scheme (Wilson and Ballard 1999). The horizontal resolution was either 0.105° (approximately 12km) or 0.21° (approximately 24km) with a domain covering much of the North Atlantic (Fig. 4.2). The model had either 38, 45, or 70 levels with the increase in vertical resolution concentrated in the mid-troposphere (Fig. 4.1). All other model parameters were kept the same, including the timestep which was set to 2.5 minutes (half the operational value - see section 4.1.1 for a discussion). All model integrations were initialised from the operational LAM analysis (50km resolution) valid at 18Z on 16/02/97 and run forward in forecast mode for 18 hours to 12Z on 17/02/97 with lateral boundary conditions from the operational LAM analyses. By using the analysis and boundary conditions from the lower resolution LAM rather than a previously spun-up higher resolution mesoscale model we can be sure that all the higher resolution mesoscale structure in the sensitivity experiments develops during the 18 hour period of the forecast. Table 5.1 provides a summary of all the model sensitivity runs.

Experiment ID	*Experiment Description*
REF / 45LEV12	Reference run, 12km resolution, 45 levels, RH_{crit}=0.85
38LEV24	24km resolution, 38 levels
45LEV24	24km resolution, 45 levels
70LEV24	24km resolution, 70 levels
NOICECOOL	As REF but no cooling due to ice evaporation
RATEHALF	As REF but half ice evaporation/deposition rate
RATEDBL	As REF but double ice evaporation/deposition rate
FALLHALF	As REF but half ice fall speed
FALLDBL	As REF but double ice fall speed
RH75	As REF but RH_{crit}=0.75
RH95	As REF but RH_{crit}=0.95

Table 5.1 Summary of model sensitivity experiments.

5.2.2 Forecast Evolution

Figure 5.1 shows the evolution of the surface pressure, ice cloud top temperature and vertical velocity fields from the 45 level, 12km resolution model run (REF) for the period of rapid system development near the end of the forecast period (06Z to 12Z). From a comparison with the observed infra-red satellite imagery the model appears to give a remarkably good forecast of the cloud distribution and development of the system (Fig. 5.1(a,b)). In particular the development of the cloud head appears to be captured well, although the details of the circulations in the cloud head do differ from observations in a similar way to the model forecasts discussed in section 4. There is a clear double trough structure at 06Z (Fig. 5.1(c)) which is associated with fronts frA and frB in the observations (see section 2.3) and the double front seen in the model runs described in sections 3 and 4. Front frB weakens as the forecast proceeds which is contrary to front frB seen in the observations which remains strong throughout the period. It is the main trough frA that is producing the main cloud head in the model although the warm front part of frB near the low centre is feeding into a smaller cloud head B overlying cloud head A. A third trough, frC, develops in the model to the north-west of the main trough during the 6 hour period (Fig. 5.1(c)). This produces a cloud band which is underneath the cloud head produced by the front frA and so is not directly visible in the cloud top temperature field. An indication of the frC front is evident in the observations although the observations did not extend far enough west to sample the front in full.

5.3 Sensitivity to Horizontal and Vertical Grid Resolution

5.3.1 Sensitivity to Horizontal Resolution

From the work presented in sections 3 and 4 it is clear that great benefits in terms of the representation of the type of systems under consideration are obtained by increasing the model resolution from 50km to 12km. In this section we briefly mention some work comparing an intermediate 24km resolution model with the 12km resolution model, both with 45 levels in the vertical. Two sets of runs were compared. The first runs were initialised from the 18Z LAM analyses as described in the section 5.2, and the second set were initialised from the 0Z 12km analysis described in section 4. We can then determine whether there is any difference in the sensitivity to resolution when the model is spinning up from low resolution (50km) or high resolution (12km) analyses.

Figure 5.2 shows the ice cloud top temperature, surface pressure, vertical velocity and surface rainfall for the 12km (45LEV12/REF) and 24km (45LEV24) model runs initialised from the 18Z LAM analysis. Overall the simulations are very similar in the synoptic structure and cloud and pressure patterns and the central low pressures are the same in both runs. The main difference is in the strength of the secondary cold front trough which is slightly weaker in the 12km run. However, the higher resolution model tends to have locally more intense peaks in the vertical velocity and surface rainfall fields. The same is true of the cross frontal circulations which look similar but more intense in the 12km runs (not shown). Also, as expected, there is generally higher resolution structure in the 12km run in all fields.

The results from the runs initialised from the 0Z 12km analysis are broadly similar but with slightly larger differences in the pressure field (not shown). The 12km run has the central pressure about 1hPa lower than the 24km run.

The overall conclusion is that increasing model resolution from 24km to 12km does not change the overall evolution and structure of this type of system but there are differences in the detail regarding the greater magnitude of the circulations and rainfall, and higher variability in the higher resolution run. Of particular importance is the much larger difference in the representation of the system between the 50km and 24km runs than between the 24km and 12km runs.

5.3.2 Sensitivity to Vertical Resolution

A series of 24km resolution runs have been compared with different vertical resolution with the emphasis on mid-troposphere resolution and the effect on the model dynamic and moisture fields. The resolutions are 38 levels with a spacing of about 50hPa in mid-troposphere (current operational mesoscale levels), 45 levels with a spacing of about 25hPa in mid-troposphere (operational mesoscale set with extra levels in the mid-troposphere) and 70 levels with a spacing of about 15hPa in mid-troposphere. Figure 4.1 illustrates the spacing of the levels for the three resolutions.

The results show some systematic differences in the model moisture fields. Figure 5.3 shows scatter plots of the 45 level model vs. the 38 level model, and the 45 level model vs. the 70 level model for the ice mixing ratio, liquid water mixing ratio and relative humidity with respect to ice. The vertical profiles of the mean bias between the 38 level model, 70 level model and the 45 level model over the domain are also shown. Between 700hPa and 300hPa (where the resolution changes most) the amount of ice in the model decreases with increasing vertical resolution with the largest difference between the 38 level and the 45 level model. However, below 700hPa there is slightly more ice in the 70 level model than in the 45 level model. The low-level difference is perhaps not seen between the 38 and 45 level models because the levels spacing is identical below about 750hPa. There is a corresponding change in the liquid water content, with more liquid water below 750hPa in the 70 level model but little difference between the 38 and 45 level models. There is a sharp transition to less liquid water in both the 38 and 70 level models at 750hPa. The relative humidity differences have a different vertical structure with higher humidities below 500hPa and lower humidities above as the vertical resolution increases.

Figure 5.4 shows a plan view of ice cloud top temperature, surface pressure, vertical velocity and rainfall at 12Z for the three models. Changing the vertical resolution has little effect on the overall evolution of the system and the system position and depth is virtually unchanged (Fig. 5.4(a)). The vertical velocity and large scale rainfall have similar peak magnitudes in all the runs, but the horizontal coherence of the troughs is stronger as vertical resolution increases. The rainfall pattern around the low centre and in the cold and warm front troughs is more elongated as vertical resolution increases.

The cross-sections in Figure 5.5 show the slight decrease in ice at higher levels as the resolution increases. Also the ice content maxima in the updraughts tend to be lower in the troposphere as the resolution increases which could account for the increased ice seen the average in Figure 5.3. In the cold front cross-section there is a

strengthening of the secondary cold front trough with increasing resolution (Fig. 5.5(a,b,c)) which can also be seen in Fig. 5.4(b). In the warm front trough (Fig. 5.5(d,e,f)) there is a shallower band of increased evaporation of ice below the cloud as the resolution increases which leads to increased descent in this region. The shallow band of dry air above the main region of warm frontal ascent and below the main cloud shield is also more distinct as the resolution increases.

In summary there generally appears to be a greater difference between the 38 and 45 level models, than between the 45 and 70 level models which suggests the model is converging as the vertical resolution is increased. As expected, there is some evidence of improved resolution of shallow features as the level spacing decreases, but the reasons for the sensitivity of the ice, liquid water and relative humidity to vertical resolution is not clear at the present time. One possible reason is the numerical treatment of the fall of ice in the mixed-phase precipitation scheme which may effectively increase the fall speed when ice falls through more than the depth of a model layer in a timestep. This will increasingly be the case as the vertical resolution is increased and would result in less ice higher in the troposphere and more ice lower down; a similar pattern to that observed in the model runs. However, further model integrations with a different ice advection scheme (Rotstayn 1997) show a similar sensitivity to vertical resolution. Another possible reason for the sensitivity is the non-linear dependence of the ice deposition rate on temperature resulting in a slight systematic bias for calculations over thicker layers. The vertical resolution sensitivity requires further investigation.

5.4 Sensitivity to Cloud and Precipitation Microphysics

5.4.1 Relative Importance of Microphysical Terms

The version 3B mixed-phase microphysics scheme in the model (Wilson and Ballard 1999) contains parametrizations of the main transfer terms between the four "water" quantities in the model; vapour, liquid droplets, raindrops, and ice particles. Note that the condensation term (vapour to liquid), which dominates the diabatic heating, is treated separately in the cloud scheme (Smith 1990). The transfer terms in the microphysics parametrization are:

1. Homogeneous nucleation of ice from liquid droplets
2. Heterogeneous nucleation of ice from vapour (and liquid droplets)
3. Deposition/evaporation of ice from/to vapour (and liquid droplets)
4. Riming of ice by liquid droplets
5. Capture of rain by ice particles
6. Evaporation of melting ice
7. Melting of ice to raindrops
8. Evaporation of raindrops
9. Accretion of liquid droplets by raindrops
10. Autoconversion of liquid droplets to raindrops

The first eight of these microphysical transfer terms involve a phase change and they have a direct impact on the model through the release or take up of latent heat. To investigate the sensitivity of the model to the microphysics we first need to assess the relative importance in the model of each of the transfer terms. Figure 5.6 shows instantaneous vertical profiles of the domain averaged latent heating rates for the reference 12km, 45 level model at 12Z. The ice deposition/evaporation rate is the largest term through most of the troposphere (the condensation term is generally larger but is not shown here). The cooling due to melting ice is also significant but is restricted to the melting layer and so is fairly localised in vertical extent. Similarly the cooling due to evaporating rain is significant but restricted to a layer close to the ground beneath the cloud base. There is a small amount of heating due to riming lower in the troposphere where there is liquid water present, but the effects of nucleation of ice, the capture of rain by ice, and the evaporation of melting ice are negligible in this case.

The dominant term in the microphysics scheme is the deposition and evaporation of ice and the choice of parameters for this term in the model could influence the development of mesoscale structure in the system. In particular the evaporation of ice beneath frontal cloud bands could have a significant impact on the evolution of these bands (Clough and Franks, 1991) and this impact needs to be evaluated to help understand the sensitivity to microphysical parameter variations. The dynamical impact of cooling due to ice evaporation in the model is described in section 5.4.2. Three cloud microphysical parameters which should have the most significant impact on the model forecast are chosen for the sensitivity studies; the deposition/evaporation rate, the fall speed of ice and the subgrid scale assumptions in the cloud scheme. These experiments are described in turn in sections 5.4.3, 5.4.4 and 5.4.5. To identify clear trends in the model sensitivity two experiments are performed for each parameter change with values chosen either side of the reference but within the

bounds of uncertainty. Table 5.1 summarises the sensitivity runs. Section 5.4.6 compares the sensitivity forecasts with observations. Section 5.4.7 summarises the results and attempts to produce an improved forecast with the indicated parameter changes.

5.4.2 The Dynamical Impact of Diabatic Cooling Due to Evaporating Ice

The diabatic cooling associated with the evaporation of ice phase hydrometeors may have a dynamical impact which acts to maintain or initiate frontal bands (Rutledge 1989, Clough and Franks 1991). To investigate the role of ice evaporative cooling in the development of the IOP16 cyclone a model experiment is performed in which the cooling due to evaporating ice is turned off (i.e. the ice is still allowed to fall and evaporate but the evaporation has no diabatic cooling effect). Although this is an unphysical experiment it should highlight the importance of this process on the mesoscale dynamics of the system.

Figure 5.7 shows a plan view of the ice cloud top temperature, vertical velocity at 800hPa, and the surface rainfall for the reference run (REF) and the run with ice evaporative cooling turned off (NOICECOOL). The low central surface pressure is 2hPa deeper when the evaporative cooling is turned off and is 40km further south (Fig. 5.7(a)). In contrast, the trailing cold front troughs are much weaker (Fig. 5.7 (a,b)). The elongated region of ascent around the low centre has a similar magnitude at 800hPa but is higher between 700hPa and 400hPa (not shown) for the model simulation with no evaporative cooling. The rainfall pattern is modified due to the different shape and position of the low centre and cloud head. The deeper low and higher vertical velocity around the low centre could be due to increased energy in the system due to the asymmetry in the diabatic processes; heat is released as ice forms but is not removed when the ice evaporates.

Figure 5.8 shows vertical cross sections across the cold and warm fronts (along the lines marked A and B in Figure 5.7(b)). There is a significant difference in the vertical velocity and ice content in the primary cold front between 700hPa and 400hPa (Fig. 5.8(b)) but this is largely a sampling problem. The system is displaced further to the south in the NOICECOOL run and the cross section is closer to the low centre. Generally the ice content and liquid water content are similar in both runs. The relative humidity is also similar except where there are diabatically forced downdraughts. Without the evaporative cooling beneath the cloud bands in the NOICECOOL model run, the downdraughts are weak or non-existent and the dry slots do not develop (Fig. 5.8(b) and (d)).

The largest impact of the evaporative cooling on the mesoscale structure is in the region of the cold front troughs. In particular the secondary ridge and trough is very weak without evaporative cooling. Figure 5.8(b) shows the much weaker downdraught beneath the primary cold front cloud between 600hPa and 900hPa at 200-300km, and the weaker low level ascent either side. Figure 5.9 shows the same cross section across the cold front with the heating/cooling rate due to ice deposition/evaporation in the REF run. Overlayed are the wind velocity difference vectors, in the plane of the section, of the REF run minus the NOICECOOL run. In the region of evaporative cooling there is much greater descent in the REF run. This

descent continues to the surface and diverges to produce two regions of increased convergence either side. This convergence acts to reinforce the initial updraught (at 350km) as well as strengthen the secondary updraught (at 200km) at low levels. There are also regions where the wind vector differences are large but are not locally associated with the evaporation of ice (between 700hPa and 400hPa in the centre of Fig. 5.9); these differences are related to the different position and shape of the system.

Although this experiment was unphysical, changes to parameters in the microphysics parametrization will affect the amount of evaporative cooling and thus change the mesoscale dynamics of the system through the mechanism described above. Further work is required to fully understand the importance of evaporative cooling on frontal system mesoscale dynamics.

5.4.3 Sensitivity to Ice Deposition/Evaporation Rate

a) Rationale

The rate of change of mass of a single ice particle due to vapour deposition or evaporation can be written as

$$\frac{\partial m}{\partial t} = \frac{4\pi C(S_i - 1)F}{\left(\frac{L_s}{RT} - 1\right)\frac{L_s}{k_a T} + \frac{RT}{Xe_{si}}} \qquad (5.1)$$

where C is the capacitance term, $(S_i\text{-}1)$ is the supersaturation of the atmosphere with respect to ice, F is the ventilation coefficient, R is the gas constant for water vapour, L_s is the latent heat of evaporation of ice, X is the diffusivity of water vapour in air, e_{si} is the saturated vapour pressure over ice and k_a is the thermal conductivity of air at temperature, T. The ice particles are assumed to be spheres so the capacitance, C, is equal to the particle radius, $D/2$. The ventilation coefficient is given by Pruppacher and Klett (1978) as

$$F = 0.65 + 0.44Sc^{1/3}\left(\frac{v(D)\rho D}{\mu}\right)^{1/2} \qquad (5.2)$$

where Sc is the Schmidt number equal to 0.6, $v(D)$ is the fall speed of the ice particle, ρ is the air density and μ is the dynamic viscosity of air.

Equation 5.1 is integrated over the particle size distribution which is parametrized as an exponential function dependent on ice particle diameter and temperature. Parametrized fall velocity diameter and mass diameter relationships are also required (Equations 5.4 and 5.5 in section 5.4.4). For further details see the Appendix in Wilson and Ballard (1999).

The main uncertainty in the integrated deposition/evaporation rate equation lies in the assumption of the sub-gridscale heterogeneity. In particular, the supersaturation may change significantly over the volume of a model grid box. This is parametrized in the

model by replacing the grid-box mean ice supersaturation, $(S_i\text{-}1)$, with an effective supersaturation:

$$(S_i - 1)_{eff} = \frac{q + q_{cl} - \alpha q_{satice}}{q_{satice}} \qquad (5.3)$$

where q is the vapour mixing ratio, q_{cl} is the liquid water mixing ratio, q_{satice} is the saturation mixing ratio with respect to ice, and α is a function of ice cloud fraction, cf_{ice}, and a critical relative humidity for cloud formation, RH_{crit}.

$$\alpha = RH_{crit}(1 - cf_{ice}) + cf_{ice}$$

The equation is complicated further by the fact that cf_{ice} also depends on RH_{crit}. However, note that the effective supersaturation $(S_i\text{-}1)_{eff}$ is always greater than $(S_i\text{-}1)$. The effective supersaturation is a relatively crude method of accounting for subgrid-scale variations, as pointed out by Wilson and Ballard (1999), and different assumptions could be made here.

The other area of uncertainty is in the capacitance and ventilation terms which depend on ice crystal habit. The model does not represent different habits (all ice crystals are assumed to be spherical), so these two terms are likely to introduce some error into the model. The ventilation coefficient, F, is dependent on the terminal velocity and length scale of an ice crystal. For an ice particle with a length scale of 1mm, the ventilation coefficient can differ by a factor of up to two depending on the assumption of crystal habit (Hall and Pruppacher, 1976). For example, bullet rosettes have twice the ventilation coefficient of dendrites, partly due to the higher terminal velocity but also to the higher characteristic length scale. The capacitance term, C, also depends on the length scale and morphology of an ice crystal and can vary by a factor of two between bullet rosettes and columns, essentially because of the larger diameter to mass ratio.

Each of these factors will vary with location (both horizontally and vertically) but it is conceivable that there is also a systematic error in the parametrization of the ice deposition/evaporation rate equation and therefore reasonable to look at the sensitivity of the model to changes to this term. Two integrations in which the deposition/evaporation term is multiplied by 0.5 and 2.0 are performed to investigate this sensitivity.

b) Results

Figure 5.10 shows the domain averaged impact of multiplying the rate equation by 0.5 and 2.0 (the whole domain is shown in Fig. 5.11). Although there is some scatter between the model runs in all fields (Fig. 5.10(a,b)), there are systematic changes to the moisture fields (Fig. 5.10(c)). The effect on cloud ice is small, but there is a trend with increasing deposition rate towards higher ice contents below 500hPa. Also with a doubling of the deposition rate, the liquid water content is reduced and relative humidity with respect to ice is reduced through most of the troposphere. Much of the impact on the relative humidity is where the air is supersaturated with respect to ice; doubling the deposition rate, roughly halves the ice supersaturation.

Figure 5.11 shows ice cloud top temperature, surface pressure, vertical velocity and large scale rainfall for the three runs. There is negligible impact on the low centre position and the integrations all have the same surface low pressure magnitude to within a fraction of an hPa. The ice cloud top temperature shows similar amounts and heights of ice cloud but more variability in the structure as the deposition rate is increased (Fig 5.11(a)). The ridge and secondary cold front trough are deeper and have a more coherent structure with increasing deposition rate (Fig 5.11(b)). There are higher extremes of rainfall close to the low centre and in the secondary trough, but decreased rainfall in the primary trough as the deposition rate increases (Fig. 5.11(c)).

A representative cross-section across the primary and secondary cold front troughs (Fig 5.12(a)) shows the ice and liquid water associated with the main cloud shield (on the far right of the cross-section) and cloud heads (towards the left of the cross section). The largest differences are in the updraughts into the cloud head where there is more ice and less liquid water between 900hPa and 600hPa as the deposition rate is increased. Figure 5.12(b) shows the relative humidity with respect to ice and the vertical velocity along the same section. The supersaturation is reduced significantly both in the cloud shield and cloud head as the deposition rate increases, and the downdraught beneath the main ascent into the cloud head is stronger. The deposition rate in Figure 5.12(c) clearly shows the increased deposition and evaporation in the updraught and downdraught associated with the cloud head. Similar trends are evident in the cross-section across the warm front in Figure 5.12(d,e,f). One further point to note from Figure 5.12(d) is the increased amount of supercooled liquid water in a layer above the main ice cloud when the deposition rate is reduced. Both the cross-sections are marked on Figure 5.11.

c) Discussion

Most of the results can be directly related to the deposition rate change. As the factor multiplying the deposition rate is increased, the model is more efficient at converting water vapour (and liquid water via the Bergeron-Findeison mechanism) to ice, and a new phase equilibrium is reached with lower supersaturation, lower liquid water content, and higher ice content. However the phase equilibrium is also affected by the fact that the deposition rate is dependent on the ice content (through the capacitance and ventilation terms) so the more ice there is in a grid box the higher the deposition rate. This acts as a positive feedback which is only counteracted by the tendency to reduce the deposition rate through reduced ice supersaturation.

The largest differences on the mesoscale are in the cold front trough-ridge-trough part of the system associated with the cloud head. This region is more energetic due to the increased latent heating in the updraught and increased latent cooling in the dry region as falling ice evaporates. Along much of the trough there is also increased descent in the dry region which acts to enhance the secondary circulation. This can be seen most clearly in the deposition cross-section developing at low levels in Figure 5.12(c). The increased rainfall close to the surface low centre can be explained by the higher ice content and resulting larger flux of falling ice which melts to rain before it reaches the ground. The surface rainfall in the primary trough is reduced because the ice falling into the dry region is evaporated more quickly and less reaches the ground as rainfall. The secondary trough has not developed enough to have a significant slope so the increased ice flux falls without much evaporation and the surface rainfall increases.

There are also implications for the depth scale of features, particularly in the region of frontal slope. Ice falling out of a frontal sloping region of ascent into a dry region beneath will only fall half the distance before it evaporates if the evaporation rate is doubled. If this depth is not resolved sufficiently by the model then there could be implications for the vertical resolution of models. In some areas there is evidence that the depth of the downdraught regions are slightly shallower with increased deposition/evaporation rate (Fig. 5.12(f)). This aspect of the results requires further investigation.

5.4.4 Sensitivity to Ice Particle Fall Speed

a) Rationale

The fall speed of an ice crystal, v, is parametrized in the model as a function of ice crystal diameter, D:

$$v(D) = cD^d \tag{5.4}$$

where $c = 25.2m^{0.473}$ s^{-1} and $d = 0.527$ at a pressure of 1000hPa. The mass diameter relationship is also required:

$$m(D) = aD^b \tag{5.5}$$

where $a = 0.069$ kg m^{-3} and $b = 2.0$. The bulk (mass-weighted) fall speed is calculated for each grid point by integrating the above equations over the ice crystal spectrum. The fall speed coefficient, c, is 1.5 times the Heymsfield (1977) value which was chosen to represent the bulk-icefall rate over a wide range of ice contents. Ice crystal fall speed strongly depends on the morphology of an ice particle and there can be significant sub-grid scale variability and a wide spectrum of particle sizes and crystal types falling at different fall speeds. For example the fall speed of ice crystal columns can be up to four times that of dendrites of a similar size (Heymsfield 1972; Kajikawa 1972). The present bulk parametrization in the model does not include the crystal habit or the sub-grid variability in a detailed way and there is certainly scope for improving the fall of ice in the model. To investigate the sensitivity of the model to ice crystal fall speed two integrations are performed in which the coefficient, c, is halved and doubled.

b) Results

Figure 5.13 highlights the domain-averaged impact of changing the fall speed on the moisture and vertical velocity fields. The largest impact is, as expected, on the cloud ice content and Figure 5.13 (a) and (b) show a fairly linear correspondence between fall speed and ice content, i.e. doubling the fall speed halves the amount of ice. Fig. 5.13 (c) shows the vertical coherence of this relation. The impact on the other fields is smaller and less coherent in the vertical. However, for a greater fall speed there is generally more cloud water and higher relative humidity (particularly when the air is supersaturated with respect to ice).

Figure 5.14 shows ice cloud top temperature, surface pressure, vertical velocity and large scale rainfall for the three runs. There is clearly less ice cloud as the fall speed increases (Fig. 5.14(a)) and the low centre surface pressure is slightly deeper; doubling the fall speed deepens the low by about 0.5hPa. However the troughs associated with the cloud head are weaker; doubling the fall speed weakens the trough by about 0.5hPa. A corresponding pattern can be seen in the vertical velocity in Figure 5.14(b) with stronger low level ascent close to the low centre and along the warm front, but weaker ascent in the cold front troughs as the fall speed increases. Associated with the deeper low and weaker cold front troughs, there is 20% more large scale rainfall close to the low and approximately half the rainfall in the trough (Fig. 5.14(c)).

Figure 5.15 shows the same cross-section as Figure 5.12 for ice and water cloud, relative humidity, vertical velocity, and ice deposition/evaporation rate. There is less ice in both the cloud shield and cloud head as the fall speed increases and an increased tongue of supercooled liquid water at the top edge of the ice cloud in the main frontal updraughts (Fig. 5.15(a,d)). The relative humidity and ice supersaturation both increase with increasing fall speed, but the vertical velocity in the frontal updraughts decreases (Fig. 5.15(b,e)). Both the deposition and evaporation in the frontal circulations are reduced as the fall speed increases (Fig. 5.15(c,f)). The trend in depth scale in the evaporation rate beneath the warm front is particularly evident, increasing with increasing fallspeed (Fig. 5.15(f)), but the same trend is not evident in the cold front cross-section.

c) Discussion

The reduced amount of ice with increased fall speed can simply be explained by the mass flux divergence argument:

Change of ice content in a grid box in a timestep =
production term + flux of ice into the grid box – flux of ice out of the grid box

Take the case of a grid box with no ice falling into the top of the box and assume the ice production term remains constant. If the fall speed is doubled, the flux out of the box is doubled, so the ice content decreases with time. Equilibrium between the production term and flux out of the box is reached when there is half the amount of ice in the grid box.

As described in the previous section 5.4.3 the deposition rate depends on the amount of ice so the less ice there is in a grid box the lower the deposition rate. This represents a positive feedback which acts to reduce the ice content further and increase the relative humidity and liquid water contents. But the deposition rate also has a strong dependence on relative humidity and as this increases the deposition rate increases, providing a negative feedback. These two feedbacks create a new equilibrium with reduced ice content, reduced deposition rate and higher supercooled cloud water and water vapour contents. The reduced ascent and descent associated with the weaker cold front trough is due to the reduced deposition/evaporation rate which reduces the diabatic heating.

One slightly surprising result is the asymmetry between the cold frontal trough and the warm frontal trough where the trends in the 800hPa vertical velocity and large scale surface rainfall are of opposite signs (Fig. 5.14(b,c)). The cold frontal trough is a fairly narrow sloping region of ascent and much of the ice that falls evaporates in the layer of dry air below (Fig. 5.15(b,c)). As the ice fall speed is reduced the amount of cooling due to evaporation increases and enhances the descending slantwise flow, which then acts to reinforce the ascending flows associated with the primary and secondary troughs. However, in the low centre and warm frontal trough there is wider region of ascent, the ice maximum is lower in the troposphere and the relative humidity is higher than for the cold front (Fig. 5.15(d,e)). Much of the ice falls through the region of high relative humidity and reaches the surface as rain. The surface precipitation therefore increases with increasing fall speed and less heat is taken out of the atmosphere (because the ice melts but does not evaporate) so there is more energy in this part of the system which results in higher vertical velocities and a lower central surface pressure.

The ice fall speed also appears explicitly in the riming (liquid water to ice) and raindrop capture (rain to ice) terms. There is a slight increase in riming rate as the fall speed is increased (not shown) but the effects of these terms on the mesoscale structure of the system are small in comparison to the direct effect of the fall speed on the ice advection.

5.4.5 Sensitivity to Critical Relative Humidity

a) Rationale

The cloud scheme in the model is a diagnostic scheme described by Smith (1990). The scheme diagnoses the amount of condensate in a grid box and the fraction of the grid box covered by the condensate and allows condensation to occur before grid-scale supersaturation. The scheme requires a critical relative humidity, RH_{crit}, which defines the grid-box mean relative humidity at which cloud condensate can form. The critical relative humidity concept is also applied to ice cloud and is used in the mixed-phase microphysics scheme for the ice deposition/evaporation (see equation 5.3 in section 5.4.3) and melting terms. The value of RH_{crit} can depend on both the vertical and horizontal resolution of the model and should generally increase with increasing resolution. The current model has a similar horizontal resolution to the operational mesoscale model but twice the vertical resolution in the mid-troposphere so a higher RH_{crit} may be desirable. A model integration was performed with RH_{crit} increased from 0.85 through most of the troposphere to 0.95. A further integration with RH_{crit} decreased to 0.75 was performed to highlight the trend in the sensitivity of the model to this parameter.

b) Results

Figure 5.16 shows the domain average results. The largest impact is on the relative humidity and liquid water content. For a higher value of RH_{crit} the relative humidity and liquid water contents are higher above 800hPa but generally lower below 800hPa. There is also a signal in the ice content variation with slightly more ice for a higher RH_{crit}.

Figure 5.17 shows the ice cloud top temperature, surface pressure, vertical velocity and surface rainfall. The ice cloud top temperature in Figure 5.17(a) shows the slightly increased amount of ice at high levels and reduced at low levels as RH_{crit} is increased. The central low surface pressure changes very little. The vertical velocity close to the low and in the warm front trough increases as RH_{crit} is increased, but the descent beneath the primary cold front trough and the ascent in the secondary trough become weaker (Fig. 5.17(b)). There is a corresponding rainfall pattern with 30% increased rainfall close to the low and in the warm front, and weaker rainfall in the cold fronts.

Figure 5.18 shows the cross-sections through the cold and warm frontal troughs. There is a decrease in ice content and low level liquid water content in the cold front trough (Fig. 5.18(a)) as RH_{crit} is increased, but an increase in ice in the cloud shield (Fig. 5.18(a)) and in the warm front trough (Fig. 5.18(d)). Associated with the higher ice contents are higher ice deposition and evaporation rates beneath the sloping frontal cloud (Fig. 5.18(c,f)). The relative humidity generally increases as RH_{crit} increases (Fig. 5.18(b,e)).

c) Discussion

The higher the value of RH_{crit} the higher the relative humidity needs to be for condensation and ice deposition to occur in an updraught, so generally higher relative humidity is expected. However, it is not immediately obvious what the other impacts of increasing RH_{crit} will be. The impact on the vertical velocity, ice and liquid water contents do not appear to be straight forward. The stronger ascent, higher ice deposition rate and higher ice contents in the main cloud shield and warm front are all consistent, but contrast with the weaker ascent, lower ice and deposition rate in the cold fronts.

One possible impact is as follows: assuming the cloud fraction is less than one in a particular region and stays the same as RH_{crit} increases (i.e. an increase in RH_{crit} will decrease the cloud fraction but there will be a compensating increase in cloud fraction due to the increase in relative humidity in the model), then the effective supersaturation for ice deposition (calculated from equation 5.3) will decrease. The result is a lower deposition rate in the updraught and therefore lower ice content and lower evaporation rate in the downdraught below. This could explain the weakening of the trough and lower ice content in the cold front as RH_{crit} increases, and may not apply to the cloud shield and warm frontal regions where the cloud fraction is likely to be close to one. Questions still remain on the exact reasons for the sensitivity to RH_{crit} in the model and of some concern is the significant sensitivity of the model evolution given the uncertainty in this parameter.

5.4.6 Comparison of Moisture Fields with Observations

The aim of the preceding sections has been to understand the impact of parameter changes on the dynamics of the mesoscale structure in a mid-latitude cyclone and the next logical step is to use this information to modify the parameters to improve the model forecast. Verification against observations is therefore required and this section describes a comparison between the model moisture fields and available observations.

a) Comparison against in situ aircraft ice water contents and size spectra

Figure 5.19 shows the observed ice water content from the aircraft 2D-C probe and the ice content extracted from the model simulations for flight legs 2, 4 and 6 (corresponding model times are 06Z, 09Z and 12Z respectively). The aircraft flight level was 360hPa throughout the flight and the model values are taken from the closest pressure level at 350hPa. The first point to note is the lack of variability in the model compared to the observations. Variability on scales around or smaller than the grid resolution (12km) will not be resolved by the model and some of the variability will be due to convective processes that are not represented in the large scale ice field. However, we might expect variability on scales of about 50km and although there are variations in the ice content on this scale the magnitude of the variations is too small.

The diffusion in the model will play a significant role in determining the variability, but other model parameters may also have an effect. The deposition rate sensitivity model runs (Fig. 5.19(a)) show there is little variation in the ice content as the deposition rate is varied. However, there is a slight increase in variability as the deposition rate is increased. The ice fall speed model sensitivity runs (Fig. 5.19(b)) show a large variation in ice content, but it is not possible with this limited amount of data at one specific level to say which model run is the best fit to the observations. In flight leg 2 there is too much ice in the reference run near the edge of the polar cloud band, but in flight leg 6 there is too little ice. The RH_{crit} model runs (Fig. 5.19(c)) show little variation in ice content but increasing variability for higher RH_{crit}.

The ice size spectra parametrization in the model is based on the exponential Marshall-Palmer distribution and can be compared against the ice crystal size spectra observed by the 2D-C probe on the aircraft at flight level. Figure 5.20 shows the observed and parametrized ice size spectra for different ice water contents. The agreement is generally good for diameters greater than 200μm, considering there is likely to be an underestimate of the number of large particles in the observational data as the maximum limit of the probe resolution is approached (800μm). For ice particle diameters less than 200μm the Marshall-Palmer distribution in the model generally underestimates the number of crystals. This change in the spectrum slope with ice particle diameter has been reported by other authors and in particular Field (1999), who describes the evolution of the bi-modal spectrum and suggests the different modes are due to aggregation processes. Parametrization of the bi-modal ice spectrum in the mixed phase precipitation is being investigated (Wilson, pers. comm.).

b) Comparison against radar reflectivity

The Doppler radar on the P3 aircraft provided reflectivity data along a similar track to the C130 (except for leg 6 which was cut short). Vertical cross-sections of reflectivity

along three of the six flight legs are shown in Figure 5.21(a). The locations of the three sections are marked on Figure 5.1(c) at the closest hour to their time of validity, i.e. 06Z, 09Z and 12Z. As has already been shown, the ice fall speed has the largest impact on the ice content so only the reflectivity cross-sections for these sensitivity runs are considered here. Figure 5.21(b,c,d) shows the corresponding cross-sections for the model with half fall speed, the reference run, and the model with double fall speed. Only data above the 0°C isotherm are shown. Although the mesoscale structures in the model and observations are not exactly the same, they are similar in many respects and useful information can be gained from a comparison. The magnitude of the reflectivity in the reference model is generally too high in the main body of cloud. In fact nowhere in the observations does the reflectivity reach the high values of over 20dBz seen in the reference model. This suggests that the model has generally too much ice which can be reduced by increasing the fall speed; the model with double fall speed in Figure 5.21 (c) is closer to the observations. Although the model overestimates the reflectivity in the main updraughts, it clearly underestimates regions of very low reflectivity (less than –10dBZ). This may be because all ice in the model has an effective fall speed so low ice concentrations with very small ice crystals are not being maintained in the model. The main problem with the comparison of reflectivity between the model and observations is the representivity of the model calculation of reflectivity which, although consistent with the model ice microphysics parametrization, can only be calculated from the simple representation of ice characteristics in the model. Further work is needed on this method of validation and the alternative method of estimating ice water content from the observed reflectivity data.

c) Comparison against dropsonde relative humidity

A comparison can be made between the model and the dropsonde temperature, relative humidity and horizontal wind observations (Fig. 5.22). The model has a vertically averaged cold bias through the troposphere of 1°C and a dry bias in the relative humidity of 8%, and there is a general trend from near zero bias close to the surface to larger errors higher in the troposphere. If the cold bias is taken into account in the relative humidity calculation, the model will have an even greater dry bias. It is possible there is a small bias of a few percent in the dropsonde relative humidity observations due to the difficulty of absolute calibration of the instrument. There is also vertical structure to the wind component errors but the vertically averaged bias turns out to be close to zero. Figure 5.23 shows the impact of the deposition rate and RH_{crit} sensitivity changes on the model minus dropsonde differences. The impact on the temperature and wind fields in the model is small in the region of the sondes and the root mean square errors for temperature and wind are not sufficiently different to be of interest. However, the relative humidity is affected by the sensitivity changes. Table 5.2 shows the standard deviation and mean of the differences (i.e. the bias) between the model and dropsonde relative humidity. There is little sensitivity in the fall speed experiments (not shown), but there is sensitivity in the deposition rate experiments in which the half deposition rate has the lowest bias (but also the largest standard deviation). The RH_{crit} experiments also show a significant sensitivity with a lower bias as RH_{crit} increases.

Experiment ID	*Model – Obs Standard Deviation (%)*	*Model – Obs Mean (%)*
REF	22.5	-8.1
RATEHALF	24.2	-6.5
RATEDBL	22.6	-8.7
FALLHALF	23.5	-8.3
FALLDBL	22.7	-8.3
RH75	23.2	-11.1
RH95	23.8	-7.1

Table 5.2 The mean and standard deviation of model minus dropsonde relative humidity (with respect to water) differences for the reference and sensitivity experiments.

5.4.7 Summary of Sensitivity Experiments and Parameter Prediction

The last section described the validation of the model sensitivity experiments with observations with emphasis on the moisture fields. The question to ask now is whether this information can be used to modify the parameter choices (or even parametrization methods) to improve the model forecast of the system. An answer to the first question can be attempted but must be approached with some caution. There is certainly a need to reduce uncertainty in the observations further and find improved ways for validation. However, an attempt is made to improve the model forecast by modifying the parameters and the results are described in this section.

There is a further question as to the generality of the results for model forecasts of mid-latitude cyclones. This report has only looked at one case study, but many aspects of the results should have a validity that extends to mid-latitude cyclones in general. Further case studies are needed to confirm this.

The results of the sensitivity experiments are summarised in Table 5.3. Combined with the validation against observations we can suggest changes to the three parameters that should improve the model forecast of the developing cyclone. The model run used for the sensitivity experiments started from the lower resolution LAM analysis so that it could spin up mesoscale structure, and is not necessarily the "best" forecast of the system. The best available forecast with current physics (see sections 4.2 and 4.3) is thought to be the 12 km 45 level model starting from the 0Z mesoscale analysis on the 17th after 15 hours of assimilation at mesoscale resolution from a LAM initial field at 09Z on the 16th (0Z MESO). The following is a summary of the perceived problems with the forecast from this model with suggested changes to the cloud and precipitation parameters.

a) The secondary cloud head is over-developed.
The trough that leads to the second cloud head (denoted A2 in the observational analysis in section 2) is believed to be overdeveloped in the model and it is hypothesised that one way of decreasing the development is to reduce the evaporative cooling beneath the frontal cloud band (denoted frB in section 2, see Fig. 2.5). Decreasing the deposition/evaporation rate, increasing the fall speed, and increasing

RH_{crit} should weaken the development of the trough and lead to a less developed secondary cloud head.

b) The central low surface pressure is too shallow by about 2hPa
The low may be too shallow for many reasons and it does depend on the magnitude of the parent low central pressure. However, in the context of these sensitivity experiments, increasing the ice fall speed should give a lower central surface pressure.

c) There is too much ice at high ice water contents.
From a comparison based on satellite imagery and the radar reflectivity there appears to be too much ice in the model. Decreasing the deposition/evaporation rate, and increasing the fall speed should reduce the amount of ice present.

d) The relative humidity is too low by a few percent.
Based on the comparison with the dropsondes, the relative humidity is too low. Decreasing the deposition/evaporation rate, increasing the fall speed, and increasing RH_{crit} should all increase the relative humidity in the model.

e) There is too little variability in the mesoscale cloud structure.
There is generally too little variability in the model, particularly in the ice cloud structure. There is little sensitivity to ice fall speed, but increasing RH_{crit} and the deposition rate should lead to a slight increase in the ice cloud variability.

Apart from the deposition rate in *(e)* all the sensitivity experiments point towards a consistent direction for each of the three parameters, i.e. decreasing the deposition/evaporation rate, increasing the fall speed, and increasing RH_{crit}. The model configuration used to test the combined effect of the parameter changes is the same as the 0Z MESO run described earlier, but the parameter changes are only introduced from 18Z (rather than 9 hours earlier at 09Z) for the last 6 hours of assimilation and the 12 hour forecast. The following parameter changes are made:

- Half the ice deposition/evaporation rate
- Double the ice fall speed (c = 33.6 rather than 16.8)
- RH_{crit} = 0.95

Figure 5.24 shows the ice cloud top temperature, vertical velocity and rainfall for the original and modified model runs at 12Z. There is less low level ice cloud in the modified run but more supercooled liquid water which does not show up in the ice cloud top temperature field (Fig. 5.24(a)). However, the cloud head is slightly smaller in the modified run consistent with expectation. The low central pressure is actually very similar in both runs but the trailing cold fronts are more coherent and elongated in the north-south direction in the modified run, showing up particularly in the vertical velocity field (Fig. 5.24(b)). These fronts (frA to the west and frB to the east) correspond to the fronts seen in the observations (section 2.3) and, although still not positioned correctly, the modified run is closer to the observed structures. The rainfall in the cold front trough shows a similar pattern to the vertical velocity but the modified run has lower extreme rainfall. Cross sections through the model show there is about half the amount of ice in the modified run with reflectivities closer to those observed, as well as higher liquid water contents and relative humidities (not shown).

	Increasing ice deposition/ evaporation rate	Increasing ice fall speed	Increasing RHcrit
Ice water content	Increase	Decrease	Increase
Liquid water content	Decrease	Increase	Increase above 800hPa Decrease below 800hPa
Relative humidity	Decrease	Increase 650hPa to 300hPa	Increase above 800hPa Decrease below 800hPa
Deposition/Evaporation rate	Increase	Decrease	Increase in warm front Decrease in cold front
Low centre	No effect on surface pressure Higher rainfall	Deeper surface pressure Higher rainfall	No effect on surface pressure Higher rainfall
Warm front trough	Little effect on trough Similar rainfall	Deeper trough Higher rainfall	Deeper trough Higher rainfall
Primary cold front trough	Similar strength trough Similar rainfall	Weaker trough Lower rainfall	Weaker trough Lower rainfall
Secondary cold front trough/ridge	Deeper trough/ridge Higher rainfall	Weaker trough/ridge Lower rainfall	Weaker trough/ridge Lower rainfall

Table 5.3 Summary of the cloud and precipitation microphysics parameter sensitivity experiments.

Table 5.4 shows the standard deviations and means for the model minus dropsonde observation differences. The model errors are similar in both runs for temperature (within 0.1°C) and wind (within 0.4 m/s), but the relative humidity bias is reduced from 5.5% to less than 2% in the modified run. Figure 5.25 shows the vertical profiles of the model bias. The relative humidity bias is reduced over most of the troposphere.

The parameter changes may not be the right changes to make for a general mid-latitude cyclone and certainly more evidence of model bias is needed before any such change is implemented. However, the exercise illustrates that knowledge of the sensitivities can be used to improve the model forecast fit to observations, and shows that the model moisture fields and mesoscale structure can be significantly changed by modifying the parameters within their bounds of uncertainty.

Experiment ID	*Model – Obs Temperature*		*Model – Obs Rel. Hum.*		*Model – Obs u-wind*		*Model – Obs v-wind*	
	s.d.	*mean*	*s.d.*	*mean*	*s.d.*	*mean*	*s.d.*	*mean*
0Z MESO	1.4	-1.4	22.1	-5.4	5.8	-0.2	5.5	-0.8
MODIFIED 0Z MESO	1.4	-1.5	22.2	-2.0	5.4	0.0	5.7	-0.8

Table 5.4 The mean and standard deviation of model minus dropsonde temperature, relative humidity and wind differences for the 0Z mesoscale run and same run with modified parameters.

6. Concluding Summary

A detailed observational and modelling study has been performed for FASTEX Intensive Observing Period 16 in which a mid-latitude frontal wave cyclone rapidly developed over the North Atlantic. The main focus of the report is the development of mesoscale structure in the system and how aspects of the model formulation and configuration influence the development of this structure. This is a vital step on the way to improving the formulation of the model at mesoscale resolution. The main conclusions from the study are summarised below.

- The initial conditions for the model have by far the largest impact on the synoptic evolution of the system in the model.

- The 12km mesoscale model on a large domain produces a better forecast from a 12km mesoscale analysis than the 50km LAM analysis. There is at least a 9 hour spin up time for the 12km model from the 50km resolution LAM analysis field.

- Overall, the 12km mesoscale model produces a good forecast of system. The intensity and location of the cloud heads and associated circulations are qualitatively correct but quantitatively could fit the observations better.

- A mesoscale data assimilation including the FASTEX dropsondes gives the best r.m.s. fit to the observations (as expected) but the mesoscale structure within the system appears to be less coherent than the 12 hour forecast.

- Increasing the horizontal resolution from 50km to 24km significantly improves the evolution of the mesoscale structure of the system. There is more variability on the mesoscale in the model when the horizontal resolution is increased from 24km to 12km but it does not have much of an impact on the overall evolution and structure of the system. This suggests that more benefit would be obtained from a 24km model on a large domain than a 12km model on a small domain for this kind of rapidly moving system.

- Increasing the vertical resolution from 50hPa (38 levels) to 25hPa (45 levels) in the mid-troposphere significantly improves the representation of the mesoscale structure. There is less of an impact when the vertical resolution is increased further to 15hPa (70 levels). However, there are systematic changes in the moisture fields as the vertical resolution increases which are possibly due to the ice advection scheme but this needs to be confirmed.

- The main sensitivities of the model forecast to uncertainties in the current mixed-phase precipitation scheme are described. There are systematic changes in the moisture fields with changes to the ice deposition/evaporation rate, ice fall speed and RH_{crit}. There is little impact on the track of the system, and only a small impact on the system depth, but the changes to the microphysics do affect the distribution between water phases and can significantly modify the mesoscale structure through dynamical interaction. There is particular sensitivity of the development of cold frontal troughs and associated cloud heads through the evaporation of ice which affects the mesoscale patterns of cloud and precipitation.

- The model forecast has a cold, dry bias compared to dropsonde observations and generally too much ice compared to radar reflectivity observations. The moisture field errors for this system can be reduced by changing the deposition/evaporation rate and ice fall speed in the current mixed-phase microphysics scheme. The particular parameter changes made here may not apply in general, and of course more complex changes to the formulation of the parametrization schemes may be required, but the experiments have illustrated how changing the parameters within their bounds of uncertainty can affect the model fields. Further case studies and verification are required.

- The indication from this study is that when forecasting fast-moving rapidly-developing frontal wave cyclones, a model with 24km horizontal resolution and 25hPa mid-tropospheric vertical resolution (45 levels) is sufficient to resolve the important mesoscale dynamics, and resources should concentrate on achieving as large a domain as possible. However, other considerations may apply to different systems and different meteorological regimes.

The results suggest that we may benefit from further work in a number of areas. Firstly, there is a question as to the generality of the cloud and microphysical sensitivity results and further case studies are needed to answer this question. FASTEX IOP 16 is a strongly forced dynamic system and the impacts may in fact be greater for a weakly forced slow moving system. Secondly, further validation of the model moisture fields against observations is required to determine any model systematic errors in mid-latitude cyclone forecasts. This could include new observation sources as well as improving the validation techniques (e.g. comparison of radar reflectivity and model ice fields). Thirdly, there is a need to improve our understanding of the dynamical effects of microphysical processes, particularly the evaporation of ice, and how the wider formulation of the cloud and microphysical schemes affects the model forecasts. Finally, this report has described the Unified Model with split-explicit Eulerian hydrostatic dynamics at a horizontal resolution not too far from the limits of using the hydrostatic approximation. The performance of the new semi-implicit semi-Lagrangian non-hydrostatic dynamics will be investigated and will enable model forecasts to be performed at higher resolution.

Acknowledgements

We wish to thank everyone that helped to make the FASTEX observational campaign such a success and in particular our colleagues at the Joint Centre for Mesoscale Meteorology and Meteorological Research Flight for their involvement in collecting and processing the data and our collaborators at CETP who processed the Doppler radar data. We would like to acknowledge the contribution from Sid Clough who initiated much of the work in this report. We would also like to thank Keith Browning and Damian Wilson for valuable discussions and are grateful to Peter Panagi for help with MDIAG and Richard Dixon for providing the SCAPE calculations.

References

Browning K. A., Roberts, N. M., 1994. Structure of a frontal cyclone. *Q. J. R. Meteorol. Soc.*, **120**, 1535-1557.

Clough, S. A., Franks, R. A. A., 1991. The evaporation of frontal and other stratiform precpitation. *Q. J. R. Meteorl. Soc.*, **117**, 1057-1080.

Courtier, P., Rabier, F., 1995. The use of adjoint equations in numerical weather prediction. ECMWF Seminar Proceedings, Parametrization of sub-grid scale physical processes, 5-9 September 1994, Shinfield Park, Reading. pp325-356.

Forbes, R. M., Clough, S. A., Dixon, M. A. G., Macallan, A. K., Roberts, N. M., 2000. The Objective Analysis of Dropsonde Data from FASTEX. JCMM Internal Report No. 106, U.K. Met. Office.

Field, P. R., 1999. Aircraft observations of ice crystal evolution in an altostratus cloud. *J. Atmos. Sci.*, **56**, 1925-1941.

Hall, W. D., and Pruppacher, H. R., 1976. The survival of ice particles falling from cirrus clouds in subsaturated air. *J. Atmos. Sci.*, **33**, 1195-.

Heymsfield, A. J., 1972. Ice crystal terminal velocities. *J. Atmos. Sci.*, **29**, 1348-.

Heymsfield, A. J., 1977. Precipitation development in stratiform ice clouds: A microphysical and dynamical study. *J. Atmos. Sci.*, **34**, 367-381.

Kajikawa, M., 1972. Measurement of falling velocity of individual snow crystals. *J. Meteor. Soc. Japan*, **50**, 577-.

Panagi, P., Dicks, E., 1997. Met. Office Unified Model data, diagnostic graphics programs and other observational data available from the JCMM through the aegis of the Universities Weather Research Network (UWERN). JCMM Internal Report No. 69, U.K. Met. Office.

Persson, P. O. G., Warner, T. T., 1991. Model generation of spurious gravity waves due to inconsistency of the vertical and horizontal resolution. *Mon. Wea. Rev.*, **119**, 917-935.

Pruppacher, H. R, Klett, J. D., 1978. Microphysics of clouds and precipitation. D. Reidel Publishing Company, Boston, USA.

Rotstayn, L. D., 1997. A physically based scheme for the treatment of stratiform clouds and precipitation in large-scale models. Part I. Description and evaluation of the microphysical processes. *Quart. J. Roy. Meteor. Soc.*, **123**, 1227-1282.

Rutledge, S. A., 1989: A severe frontal rainband Part IV: precipitation mechanisms, diabatic processes and rainband maintenance, *J. Atmos. Sci.*, **46**, 3570-3594.

Shutts, G. J., 1990. SCAPE charts from numerical weather prediction model fields. *Mon. Wea. Rev.*, **118**, 2745-2751.

Smith, R. N. B.,1990. A scheme for predicting layer clouds and their water content in a general circulation model. *Q. J. R. Meteorol. Soc.*, **116**, 435-460.

Talagrand, O., Courtier, P., 1987. Variational assimilation of meteorological observations with the adjoint vorticity equations. Part I. Theory. *Quart. J. Roy. Meteor. Soc.*, **113**, 1311-1328.

Thorpe, A. J., Emanuel, K. A., 1985. Frontogenesis in the presence of small stability to slantwise convection. *J. Atmos. Sci.*, **42**, 1809-1824.

Wilson, D. R., Ballard, S. P., 1999. A microphysically based precipitation scheme for the UK Meteorological Office Unified Model. *Quart. J. Roy. Meteor. Soc.*, **125**, 1607-1636.

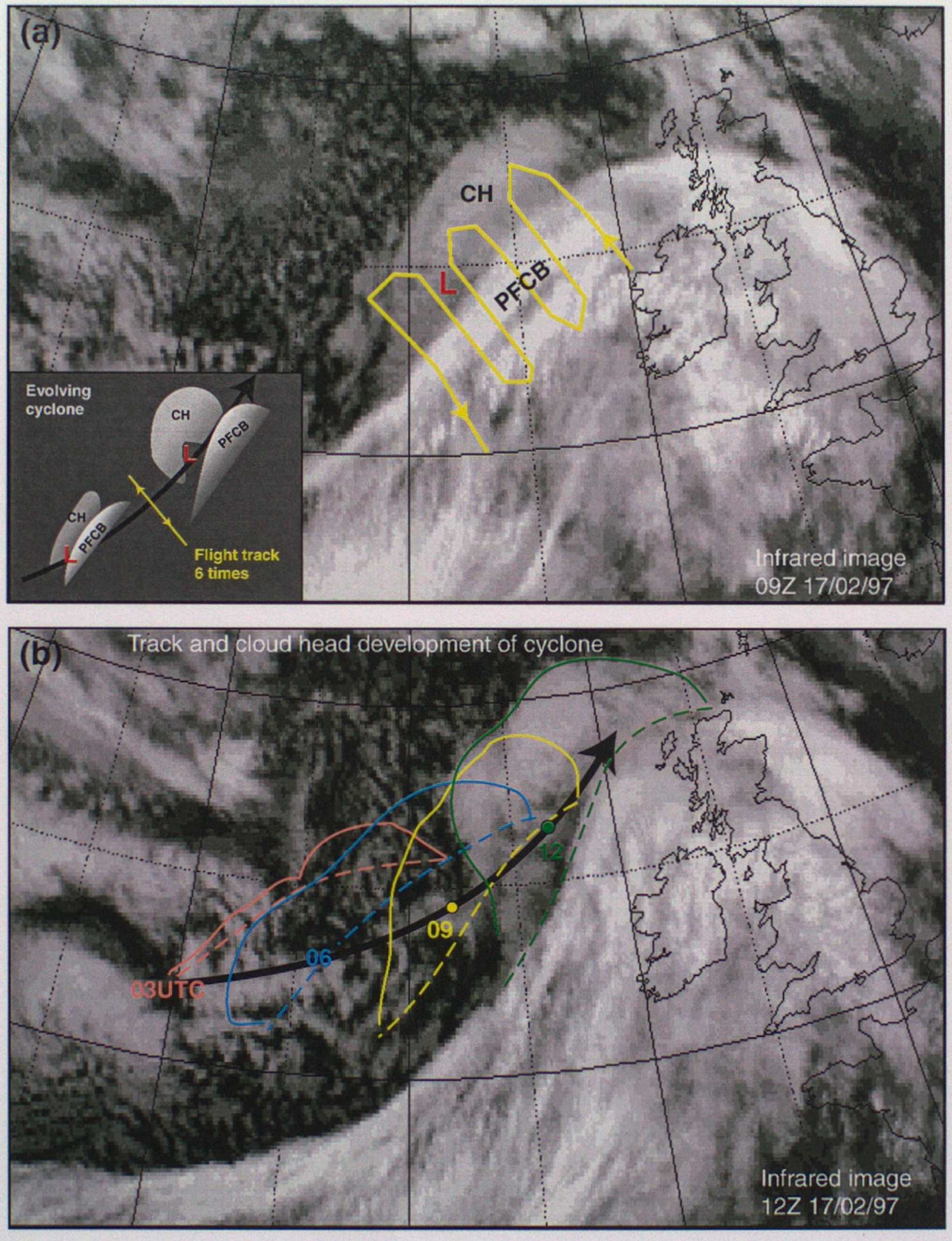

Figure 2.1 (a) Meteosat infrared image for 09Z, 17 Feb 1997. The Polar Front Cloud Band is labelled PFCB and the emerging cloud head CH. The red 'L' marks the low centre. Superimposed on the image is the track of the UK C-130 aircraft (yellow line) spread out in a frame relative to the velocity of the moving system (table 2.2) around 09Z. The bottom left panel in (a) shows schematically how the cloud pattern evolved during the period when low tracked across the aircraft flight legs.
(b) Meteosat infrared image for 12Z, 17 Feb 1997. The solid lines mark the edge of the cloud head(s) at 12Z (green), 09Z (yellow), 06Z (blue) and 03Z (pink). The dashed lines mark the edge of the PFCB at the same times. The black arrow shows the track of the low. Low centre locations are marked with dots for 09 and 12Z. At 03 and 06Z the low centre can not easily be defined.

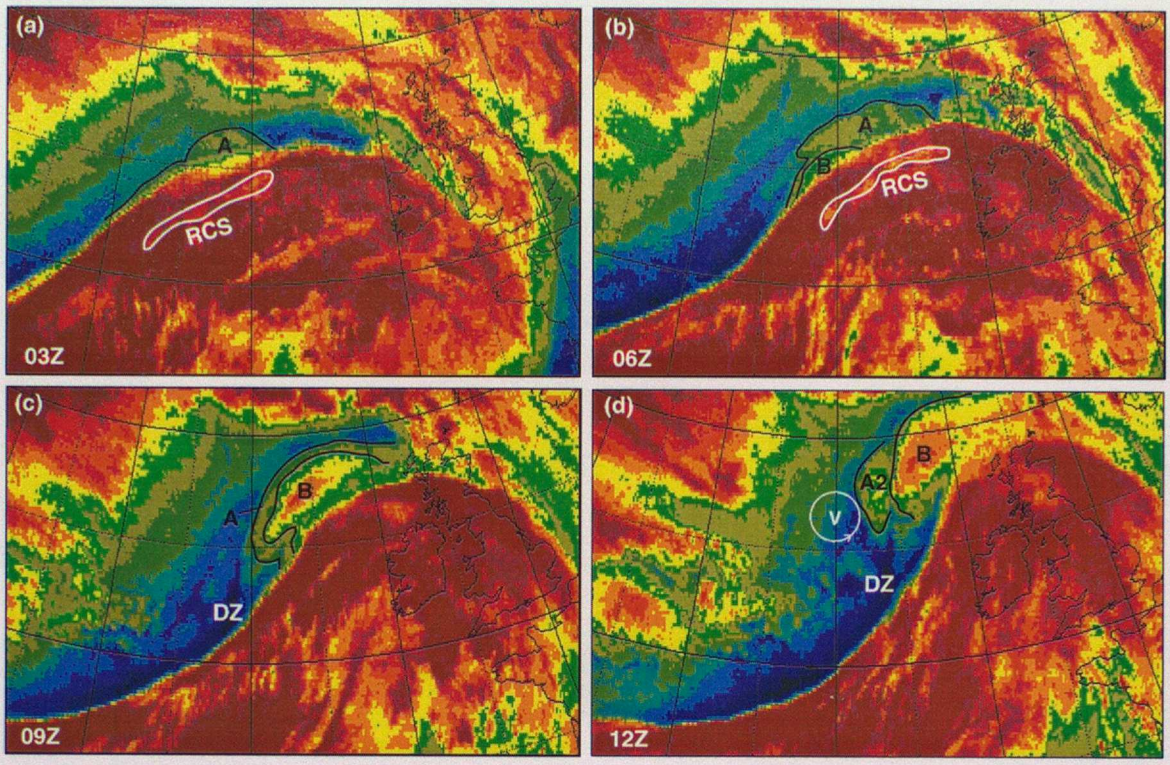

Figure 2.2 A sequence of Meteosat water vapour images for 03,06,09 and 12Z, 17 Feb 1997. Upper tropospheric cloudy regions are shown red/orange, moist/cloudy regions are yellow/green and the driest regions blue. Black lines mark the edges of emerging cloud heads A, B and A2. The white line in (a) &(b) encloses a strip of lower cloud tops (or Reduced Cloudiness Strip 'RCS'). The centre of a 500hPa vorticity anomaly at 12Z is labelled 'V' in (d) and the driest part of the blue dry intrusion region, associated with a region of upper/mid tropospheric descent to the southeast of the upper-level vorticity anomaly, is labelled 'DZ' in (c) and (d).

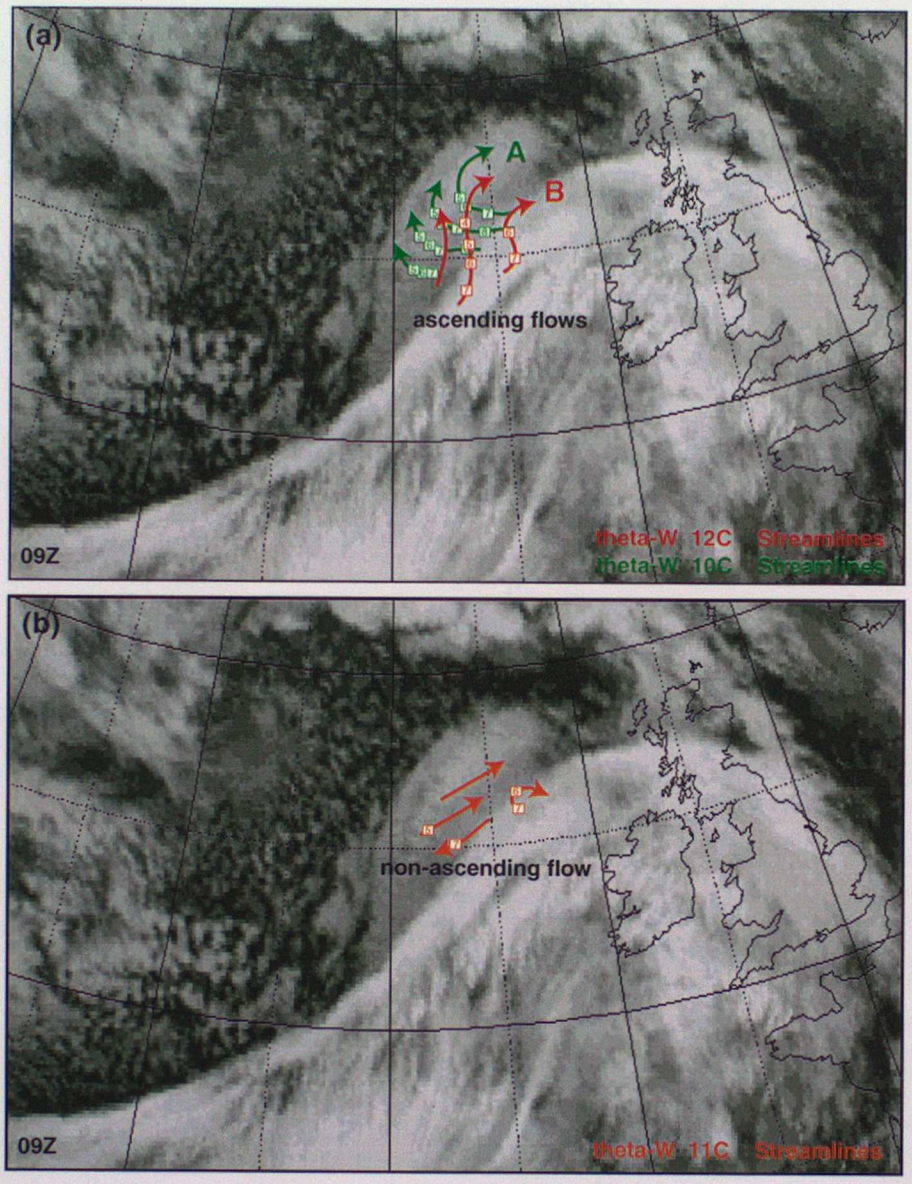

Figure 2.3 Meteosat infrared images for 09Z, 17 Feb 1997. Superimposed on each picture are streamlines depicting the system relative flow in the cloud head region on the 10, 11 and 12°C θ_w surfaces. The green streamlines in (a) show the ascending flow into cloud head A on the θ_w=10°C surface. The red streamlines in (a) show the ascending flow into cloud head B (above cloud head A) on the θ_w=12°C surface. The orange streamlines in (b) show the non-ascending flow between cloud heads A & B. Streamlines were constructed by first spreading out the dropsonde measurements from the UK C-130 aircraft relative to the velocity of the system around 09Z as in figure 1(a), then the relevant θ_w surfaces were located and the system relative winds on those surfaces were plotted. The arrows were drawn by hand on the basis of the system relative winds, only where the relative humidity exceeded 85% below 500mb and exceeded 60% above 500mb. The system velocity used here is a compromise between the individual velocity of each cloud head - cloud head B moved faster than cloud head A. Numbers in boxes along the streamlines indicate the pressure level (hPa/100) of the θ_w surface - e.g. 7 = 700hPa.

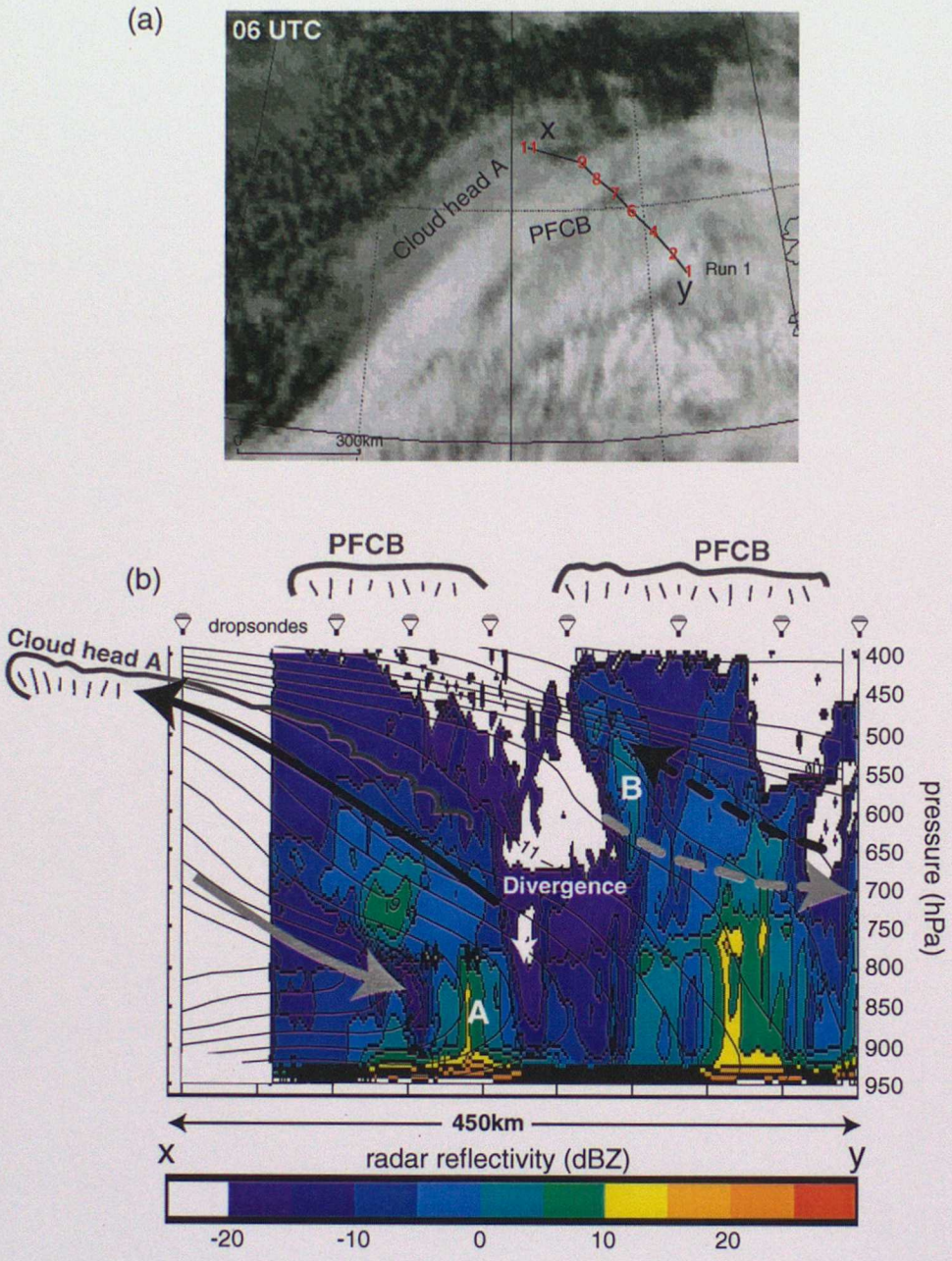

Figure 2.4 (a) Meteosat IR imagery for 06Z, 17 Feb 1997 showing cloud-head A and the Polar Front Cloud Band (PFCB). X, Y shows the ends of the cross-section in (b). Red numbers indicate the position of dropsondes shifted relative to the velocity of the moving cyclone around 06Z (and adjusted 20km north to account for parallax error) to get the correct position relative to the imagery at that time.
(b) Run 1 cross-section from X to Y in (a), with projected dropsonde locations indicated by parachute symbols. Colours show radar reflectivity from the P3 aircraft projected on to the cross-section. Black contours show θ_w every 0.5°C derived from the objective analysis (Forbes et al. 2000) of dropsonde measurements. The solid arrows indicate the along-section component of the maximum flow into cloud head A (black) and descent beneath (grey) derived from objective analysis and scrutiny of the raw data. The dashed arrows show the flow couplet associated with cloud head B. Label 'A' marks the precipitation core associated with front frA (figure 2.5). Label 'B' marks the location of precipitation from the slantwise ascent part of cloud head B. The top of the PFCB and cloud head A is shown by the curvy grey lines.

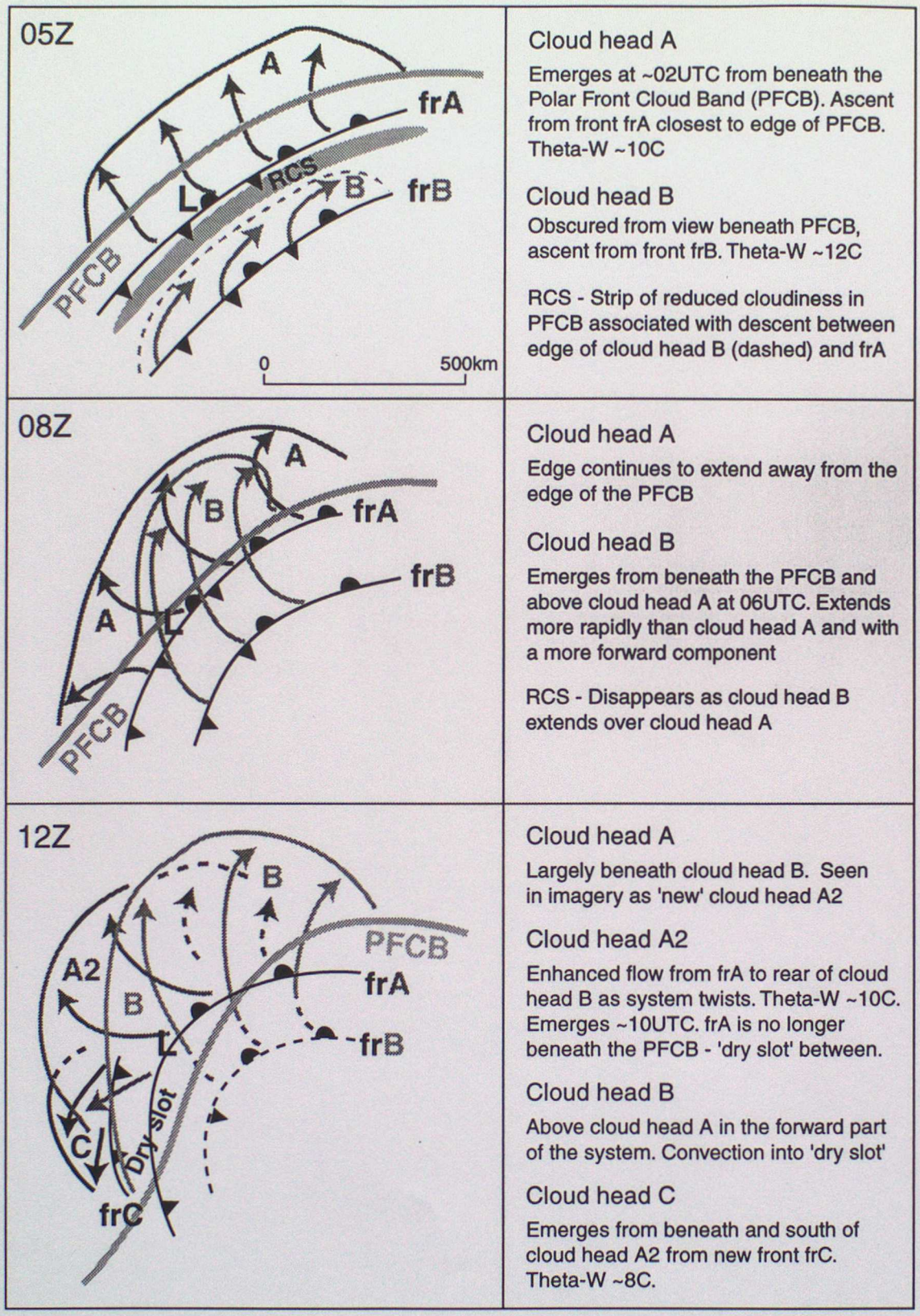

Figure 2.5 A sequence of three schematic diagrams to show the evolution of multiple cloud heads and fronts during the FASTEX IOP16 cyclone development. The frames represent an attempt to summarise the cyclone structure on the basis of a synthesis of the satellite, dropsonde and radar data available.

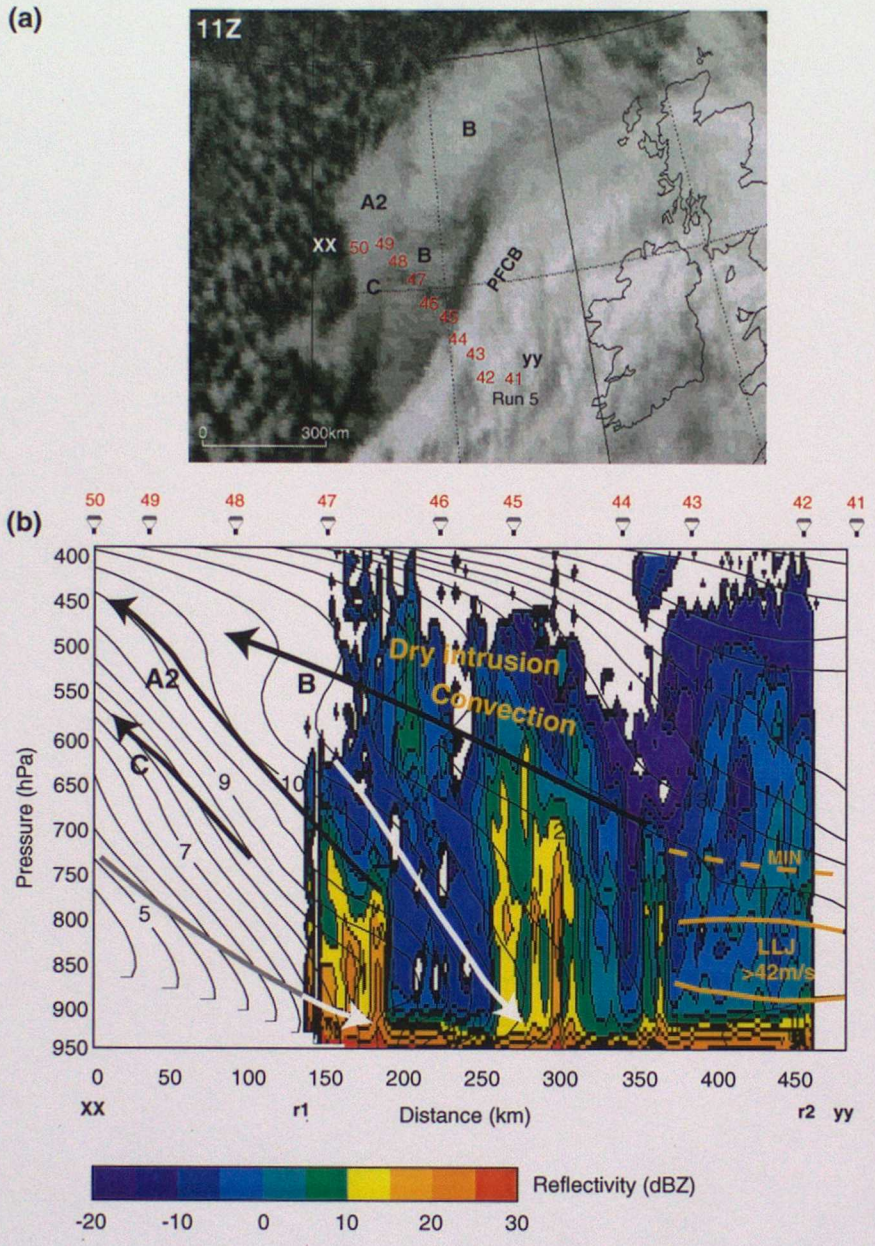

Figure 2.6 (a) Meteosat infrared imagery for 11Z, 17 Feb 1997 showing cloud heads B, A2 and C and the Polar Front Cloud Band (PFCB). XX, YY shows the ends of the cross-section in (b). The red numbers indicate the position of dropsondes (released from the UK C-130 aircraft) shifted relative to the moving cyclone in order to get the correct position relative to the imagery at 11Z.
(b) Run 5 cross-section from XX to YY in (a), with projected dropsonde locations indicated by the parachute symbols and red numbers. Colours show radar reflectivity from the P3 aircraft projected on to the cross-section from r1 to r2. (The P3 flew a track nearly parallel to the C-130). Black contours show wet-bulb potential temperature derived from the objective analysis of dropsonde measurements. Black arrows indicate the along-section component of the maximum flows into cloud heads B, A2 and C derived from objective analysis and a detailed subjective evaluation of the raw data. Above flow B, convection is identified penetrating into the dry-intrusion region. White arrows show the descending flow components beneath the cloud heads. The solid yellow lines enclose a low-level jet (LLJ) region of wind speeds in excess of 42m/s. The dashed yellow line above the LLJ marks the axis of a wind speed minimum.

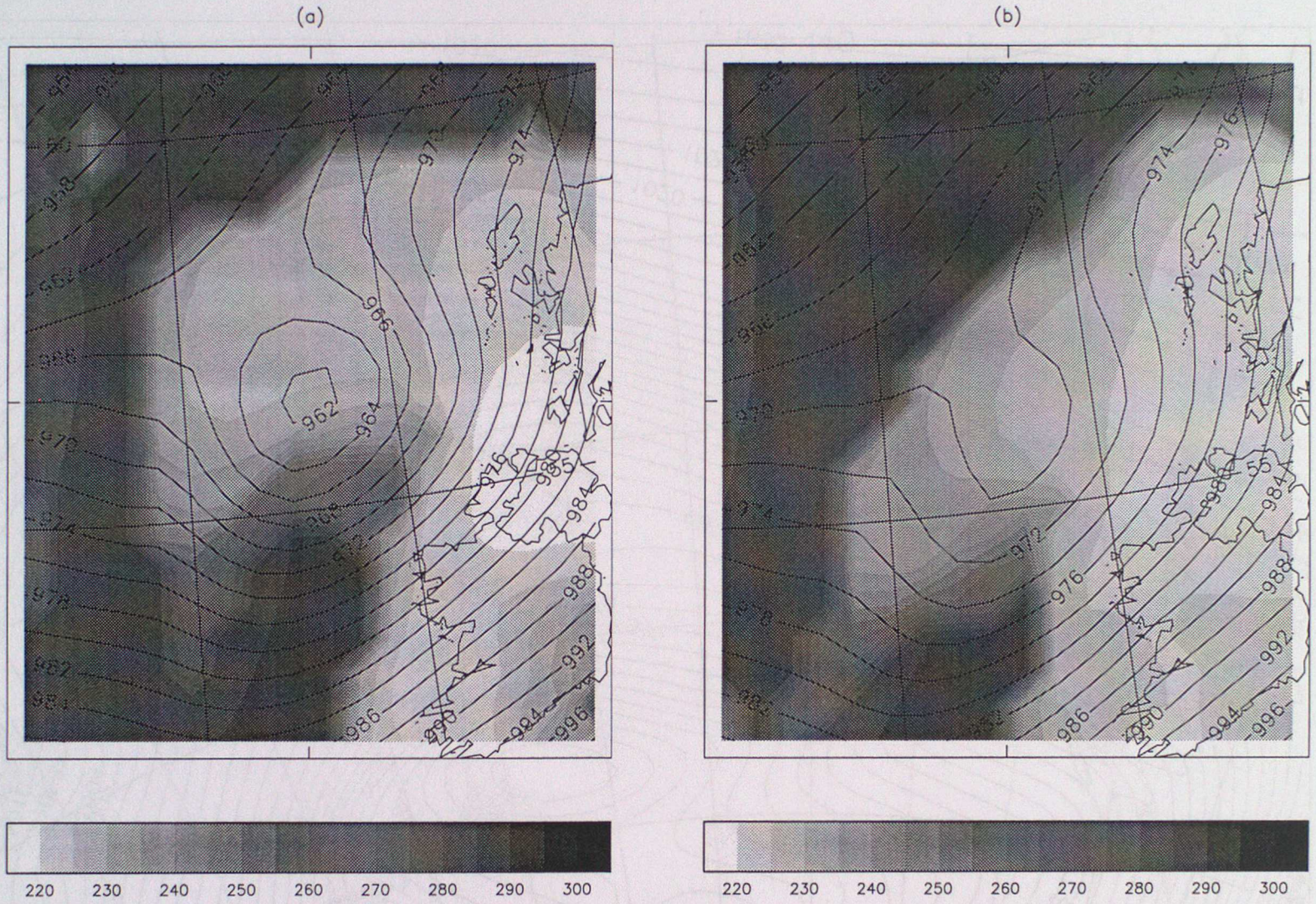

Figure 3.1 12Z 17th pmsl (hPa) and cloud top temperature (K) for (a) 18Z 16th and (b) 0Z 17th LAM runs.

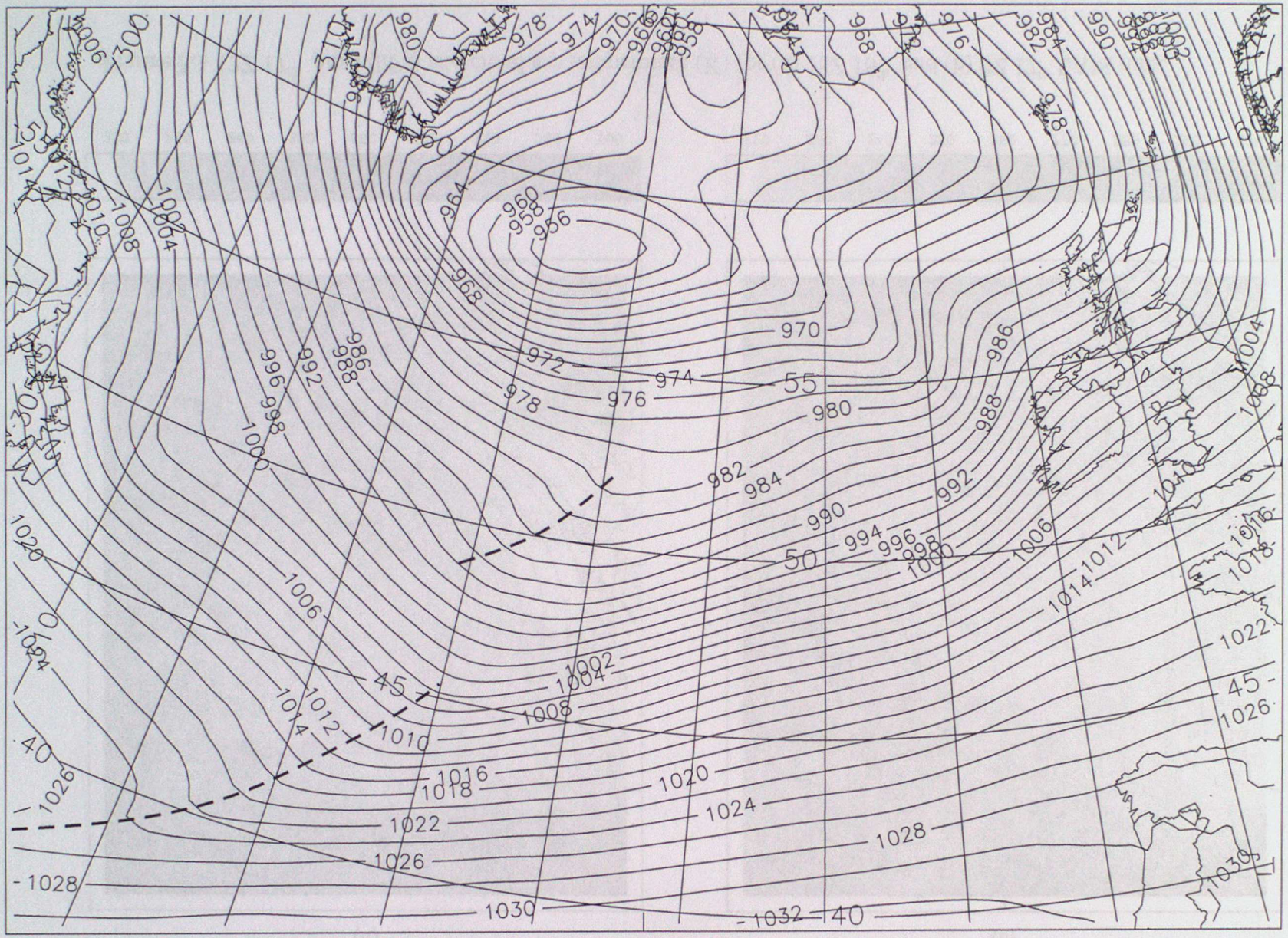

Figure 3.2 LAM pmsl (hPa) at 18Z 16th. Dotted lines indicate the positions of the troughs.

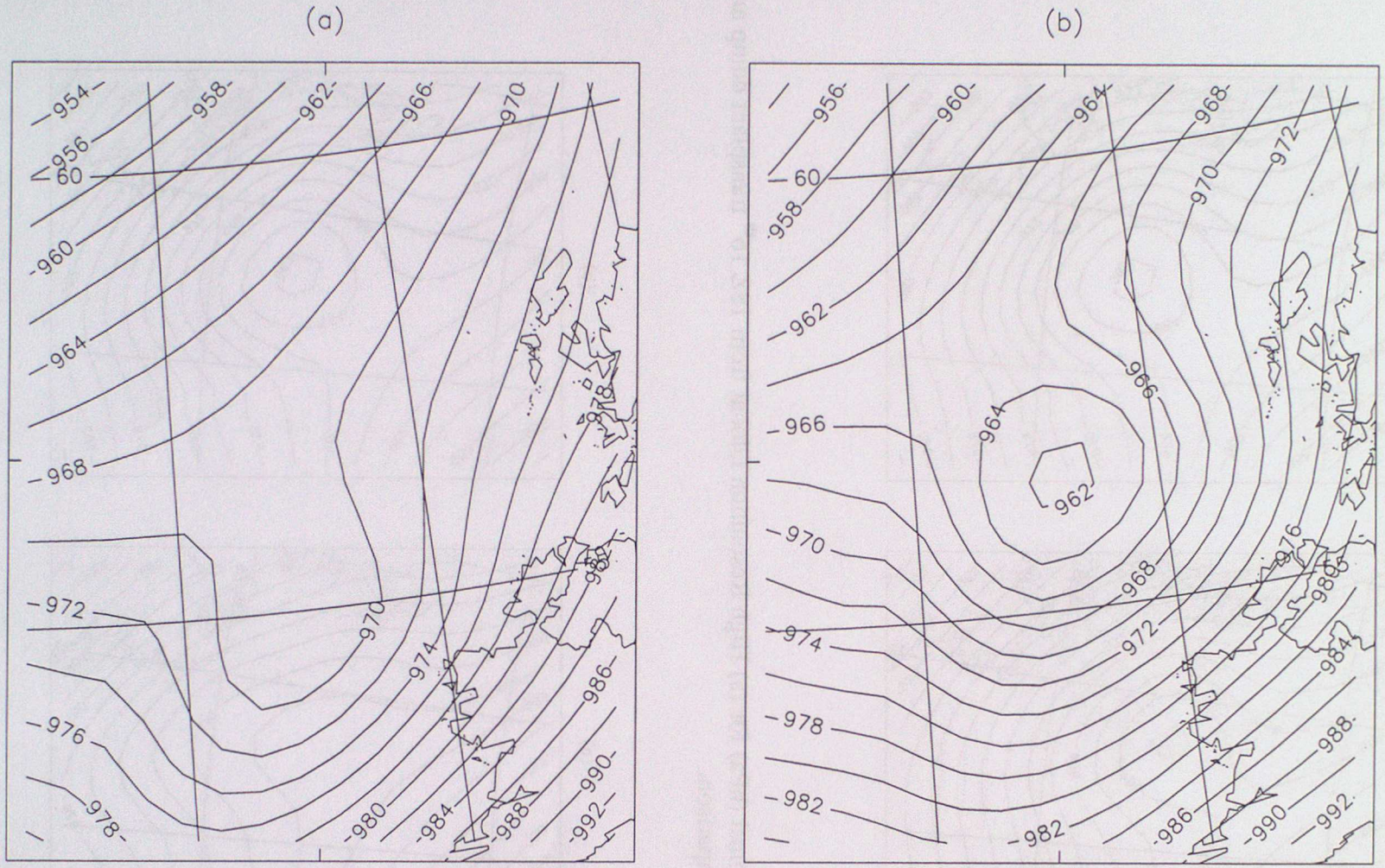

Figure 3.3 pmsl (hPa) at 12Z for 18Z 16th for (a) High Resolution Global (b) LAM

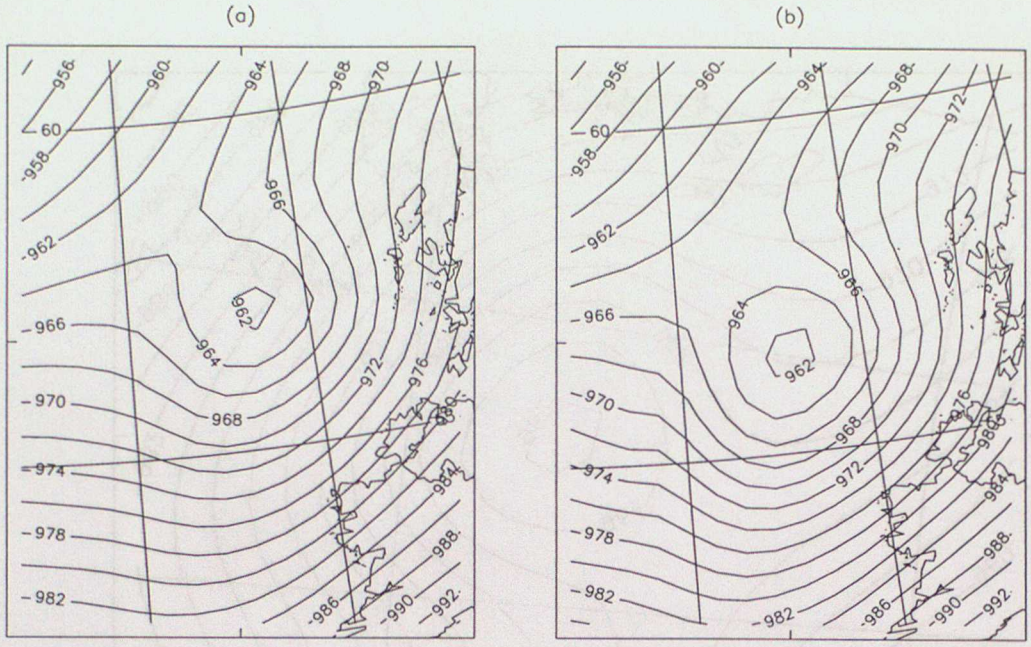

Figure 3.4 12Z 17th pmsl (hPa) for (a) High Resolution Global from 18Z 16th transplant dump and (b) 18Z LAM for comparison.

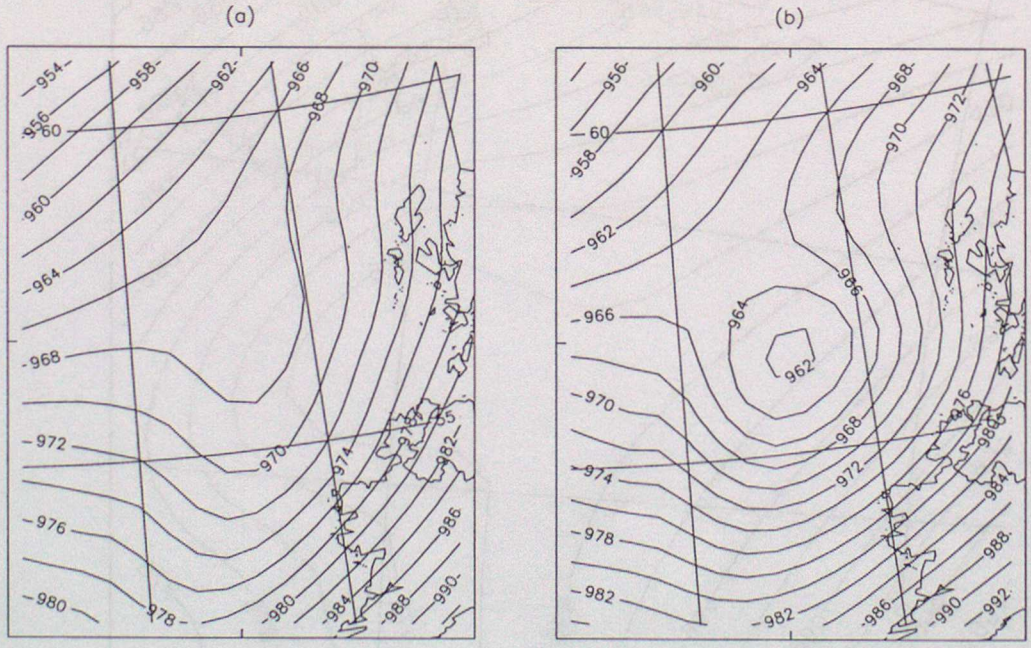

Figure 3.5 12Z 17th pmsl (hPa) from (a) High Resolution Global from 12Z 16th transplant plus 1 assimilation cycle (to 18Z) with (b) 18Z 16th LAM for comparison.

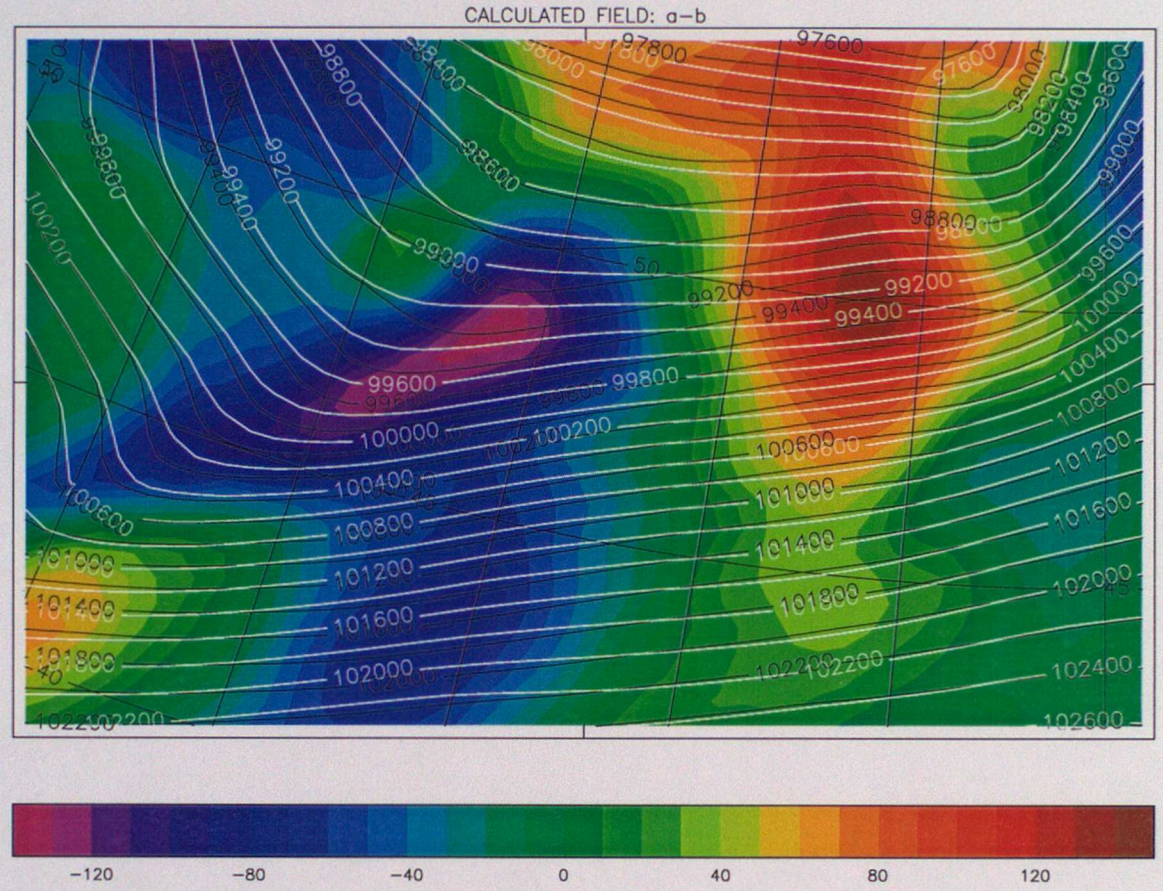

Figure 3.6 pmsl (Pa) at 18Z 16th for LAM analysis (black contours) and transplanted 12Z high resolution global + 1 cycle of assimilation to 18Z (white contours). Colours show the difference (in Pa) between these two fields.

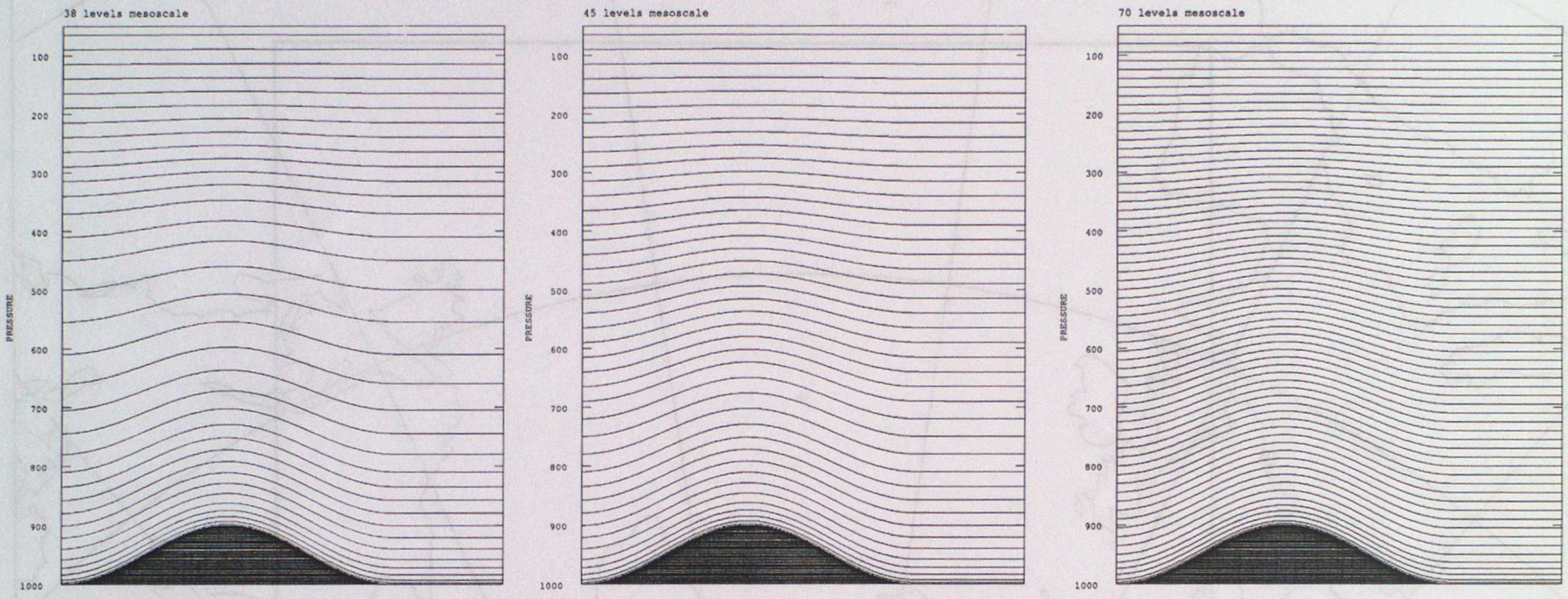

Figure 4.1 Mesoscale model levels for 38, 45 and 70 level models.

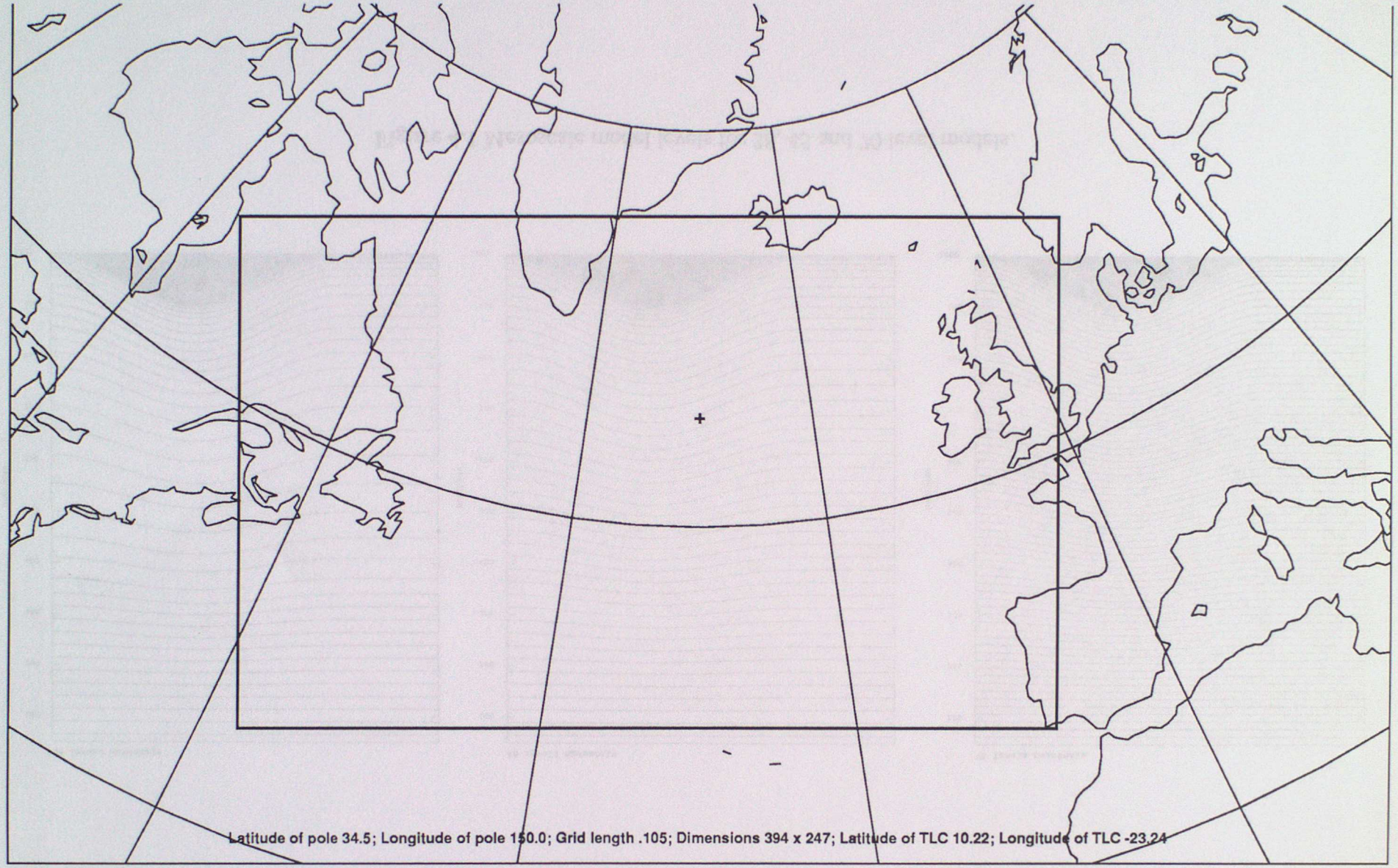

Figure 4.2 The box shows the domain used for the 12km mesoscale simulations with assimilation starting at 9Z 16th.

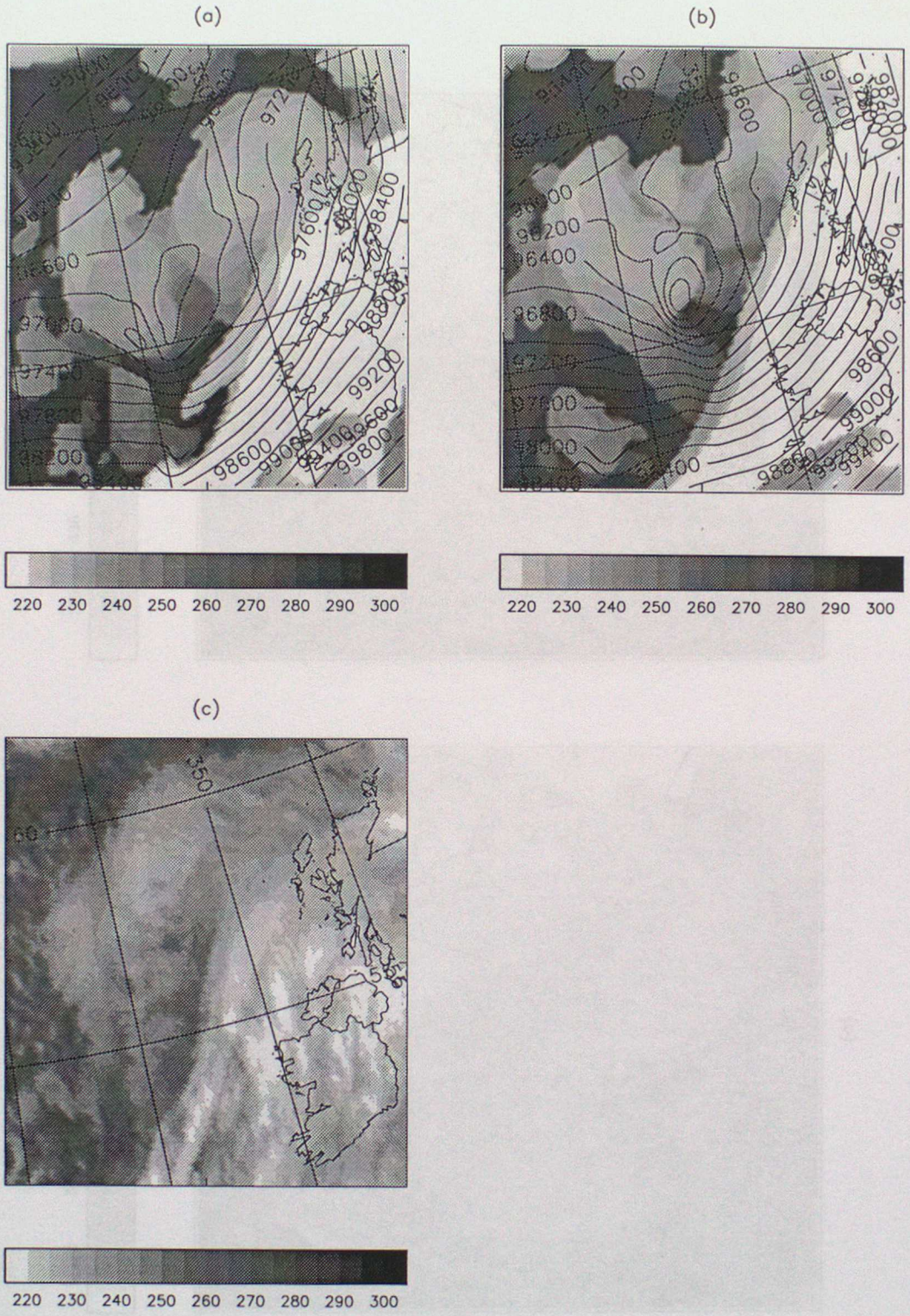

Figure 4.3 12Z 17th Cloud top temperature (K) and pmsl (Pa) for mesoscale forecasts from (a) 0Z 17th and (b) 18Z 16th, and (c) the satellite infra-red image for comparison.

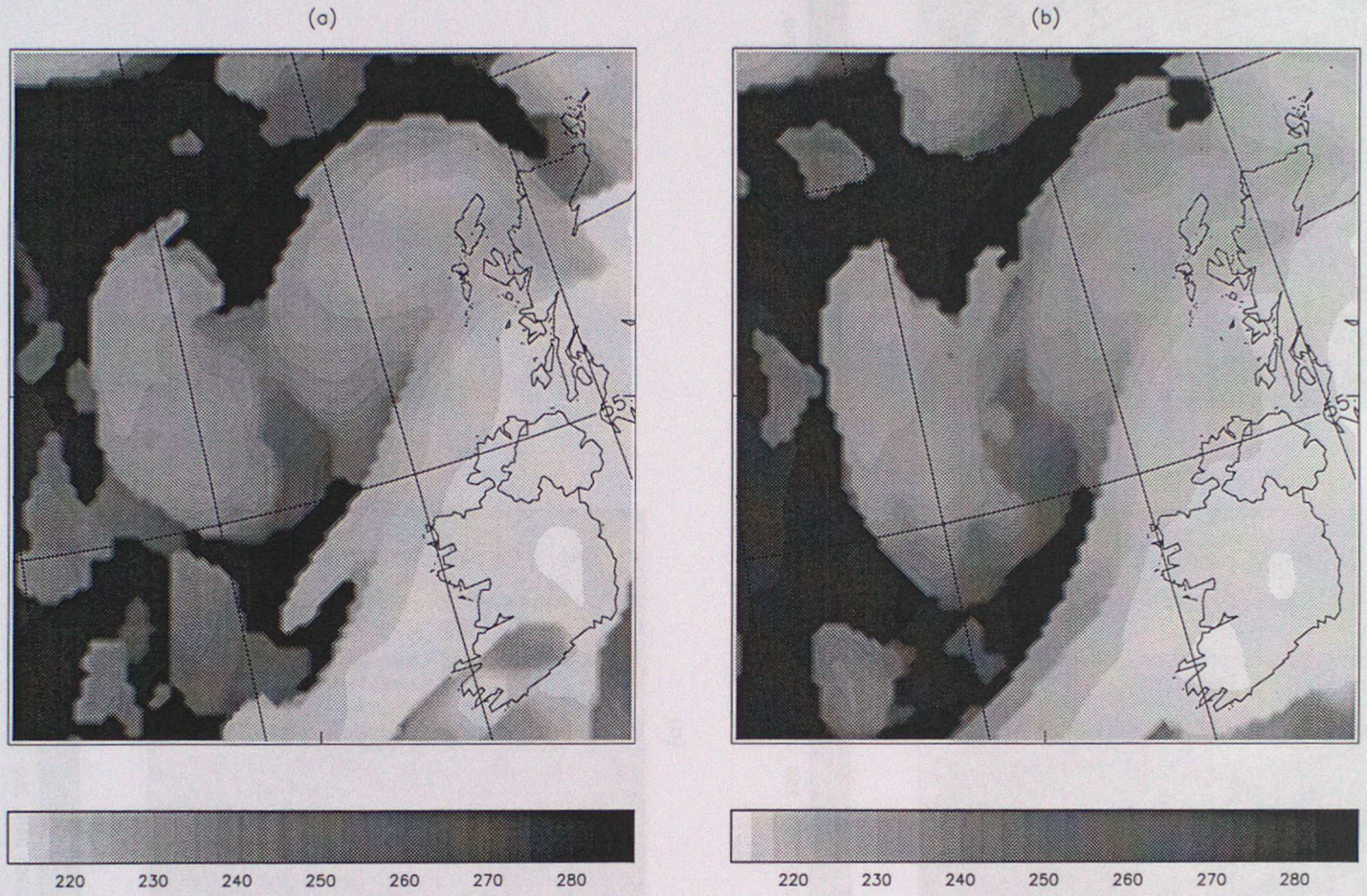

Figure 4.4 12Z 17th Cloud top temperature (K) from 0Z forecast showing shape of cloud shield for boundary conditions taken from (a) LAM analyses and (b) 18Z LAM forecast.

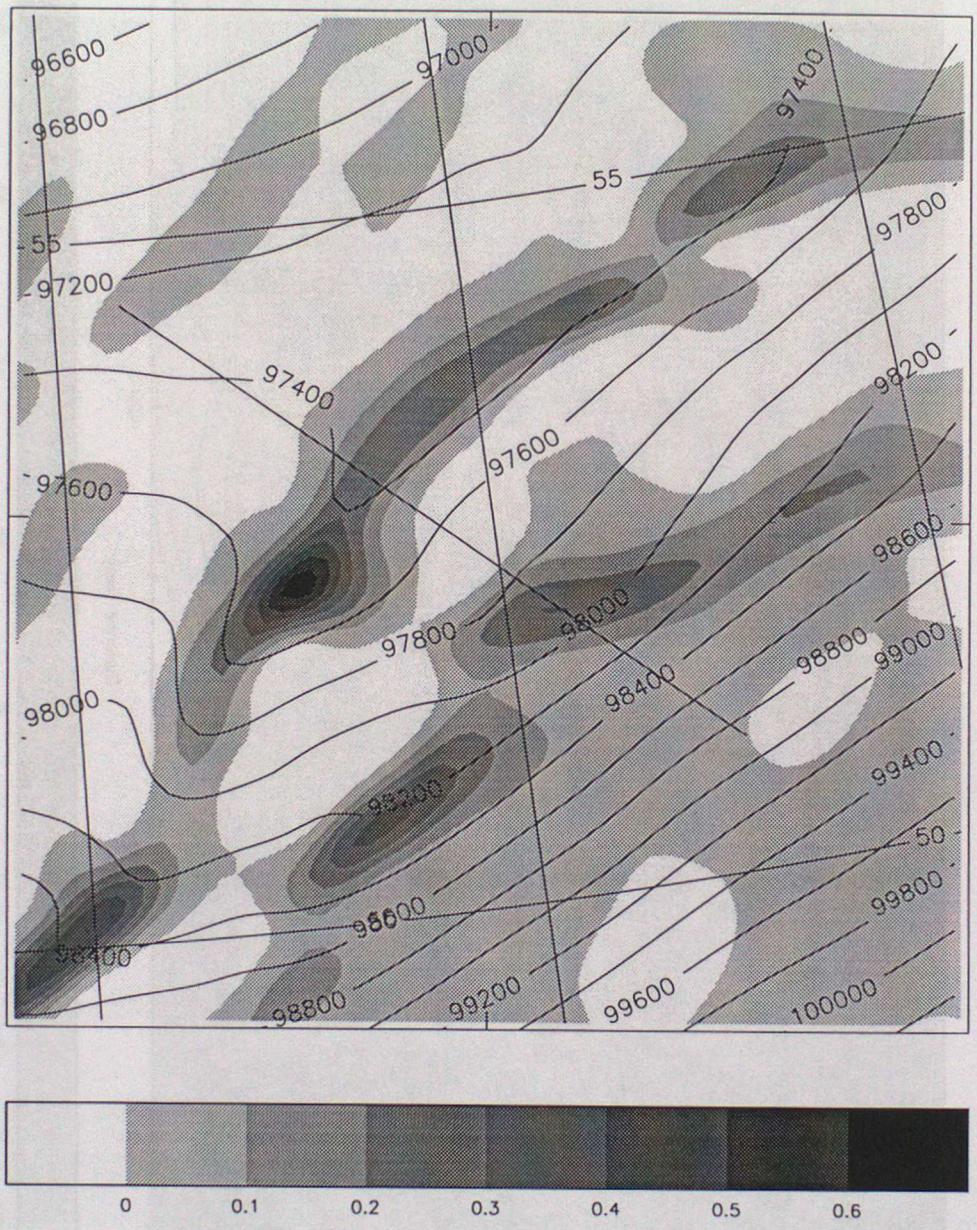

Figure 4.5 Plan view of 0Z 17th 12km, 45 level mesoscale run fields at 6Z: Contoured pmsl (Pa) and shaded 800hPa vertical velocity (m/s) showing double structure.

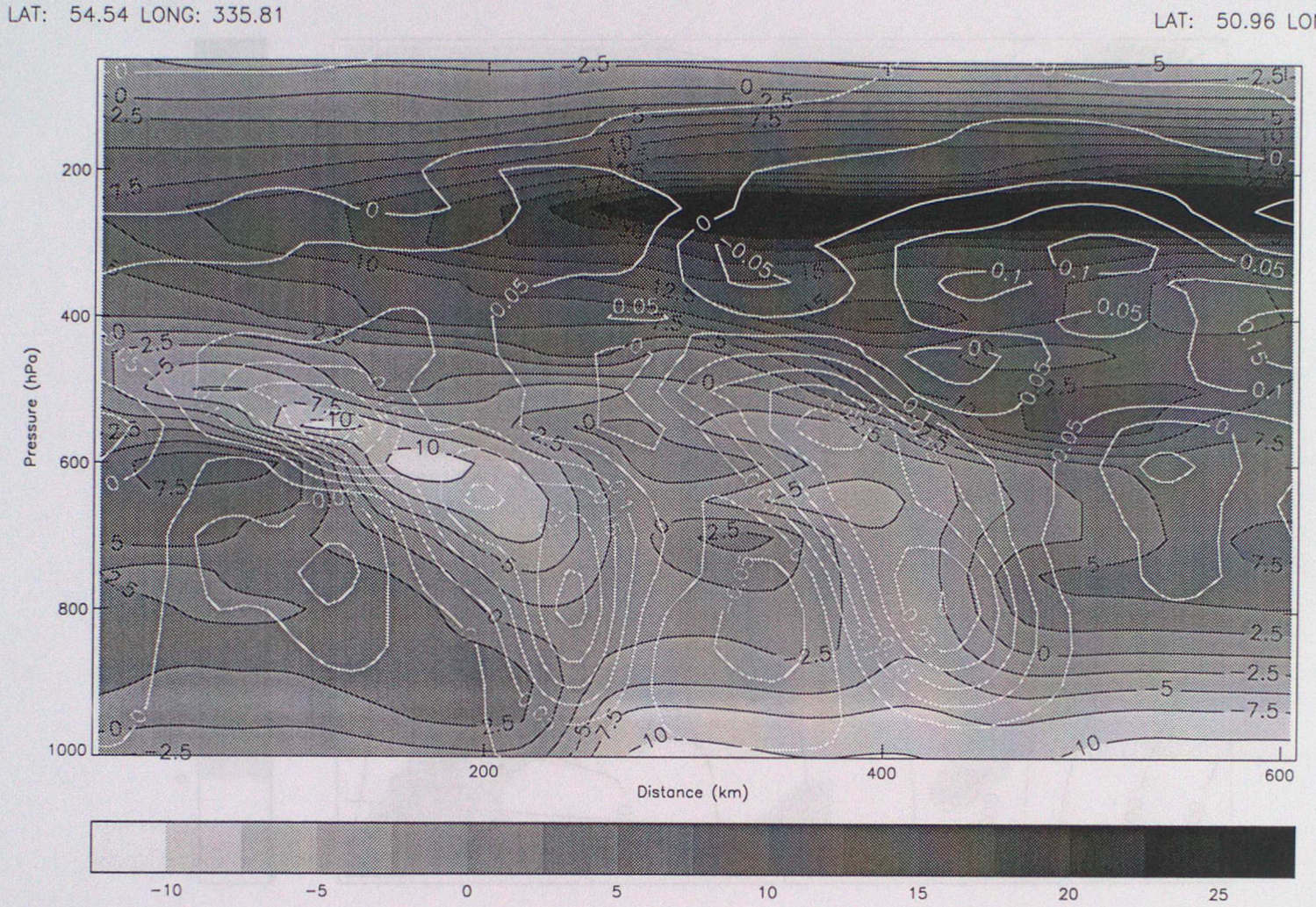

Figure 4.6 Cross section across the double frontal structure at 6Z along the line shown in Figure 4.5 showing cross-frontal velocity (shaded) and vertical velocity (contoured). Units are m/s.

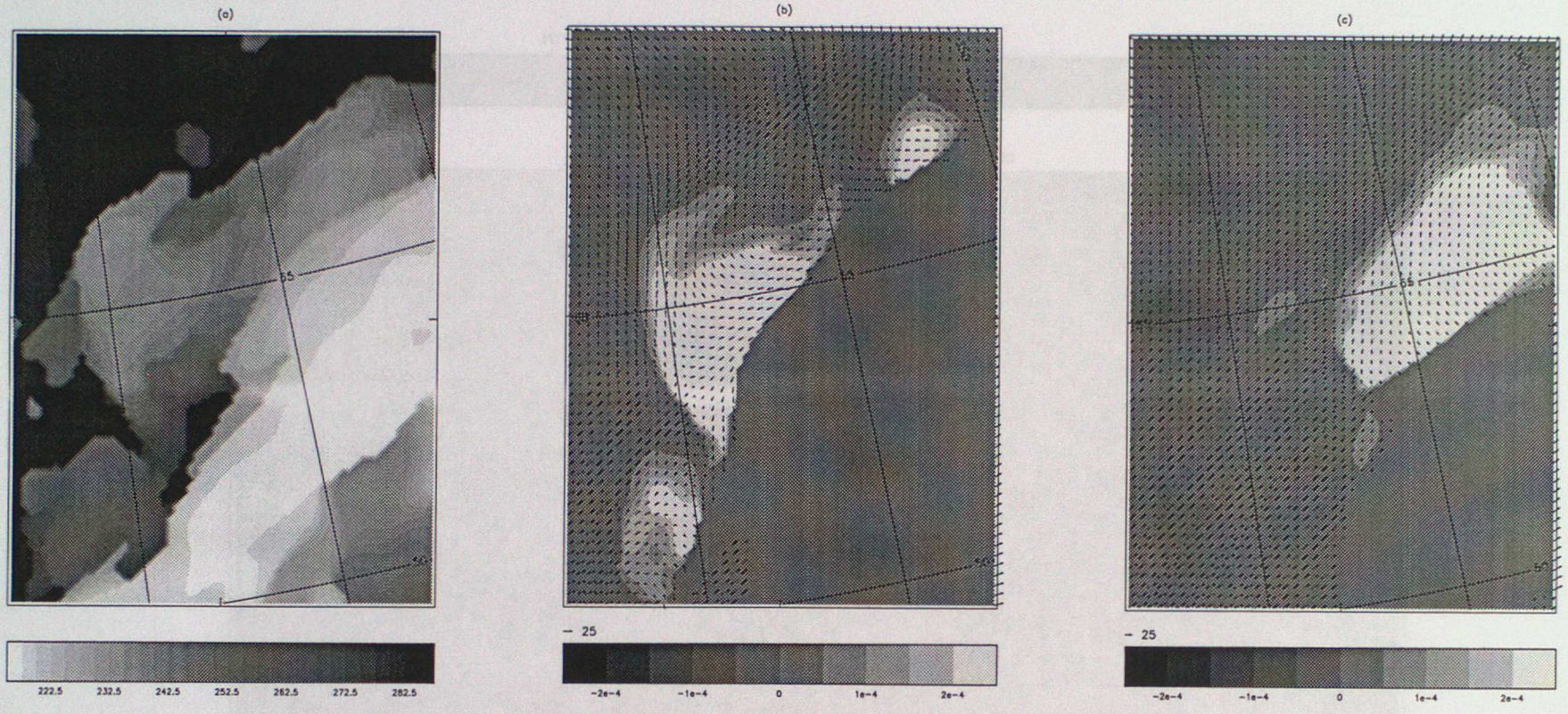

Figure 4.7 (a) Cloud top temperature (K) of cloud head at 9Z 17th for 0Z 12km, 45 level mesoscale run. (b) and (c) show the corresponding cloud ice mixing ratio (kg/kg) (shaded) and system relative velocity (m/s) (arrows) on the 8°C and 11°C theta-w surfaces.

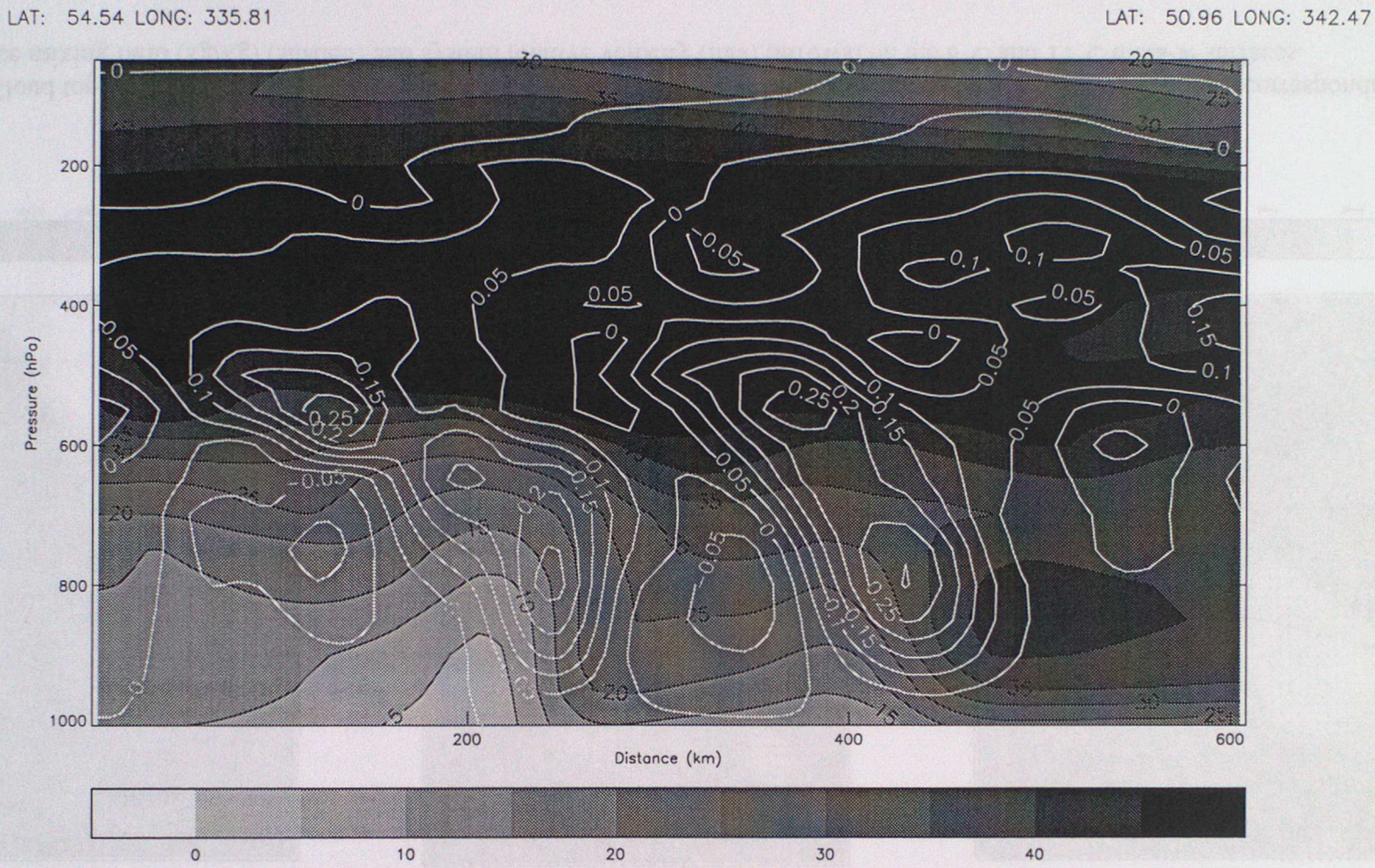

Figure 4.8 Cross section across the double frontal structure at 6Z along the line shown in Figure 4.5 showing along-front velocity (shaded) and vertical velocity (contoured). Units are m/s. There is a distinct low-level jet at 500km, 800hPa.

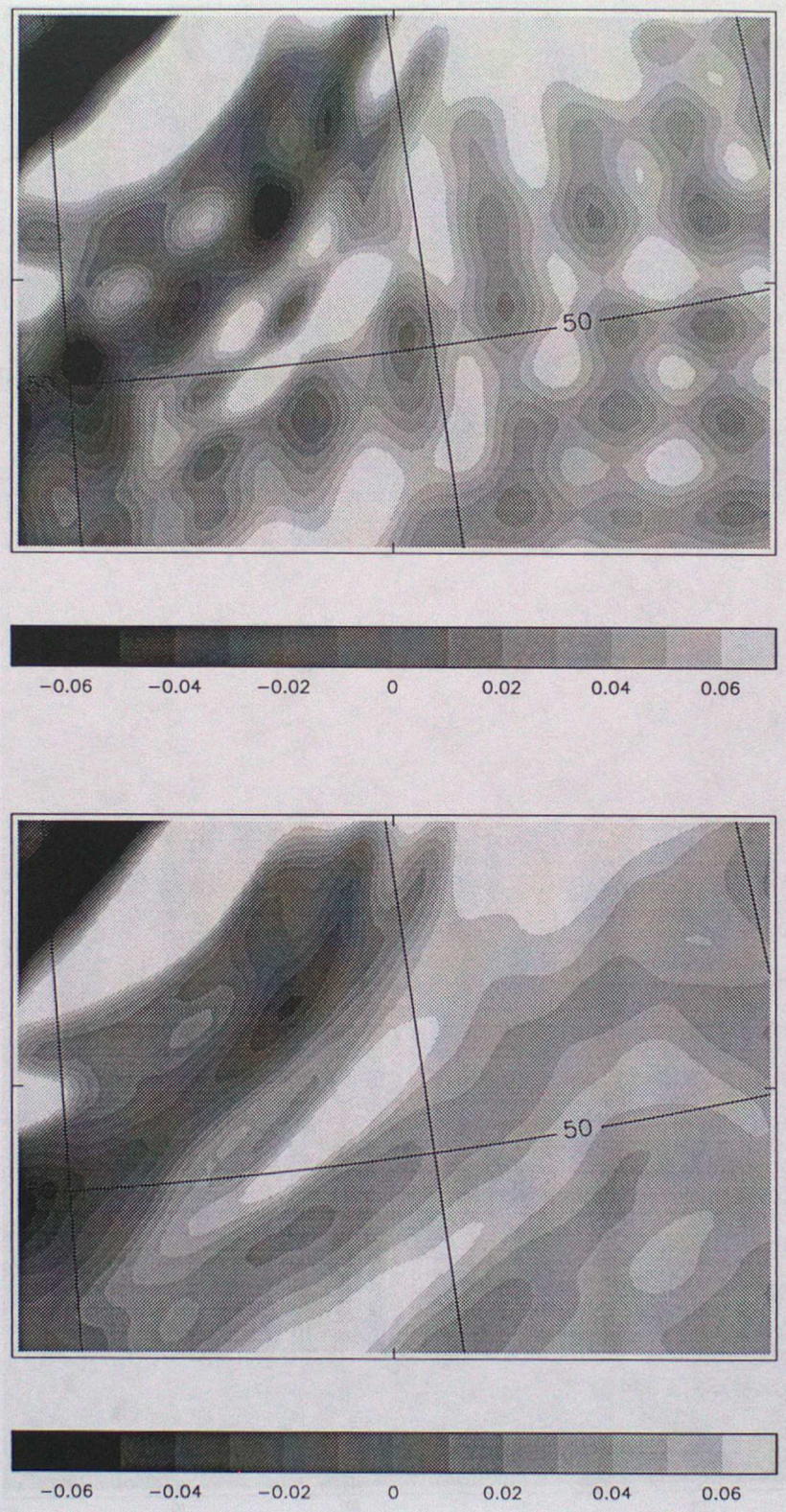

Figure 4.9 800hPa vertical velocity (m/s) fields with (a) operational timestep and (b) half operational timestep.

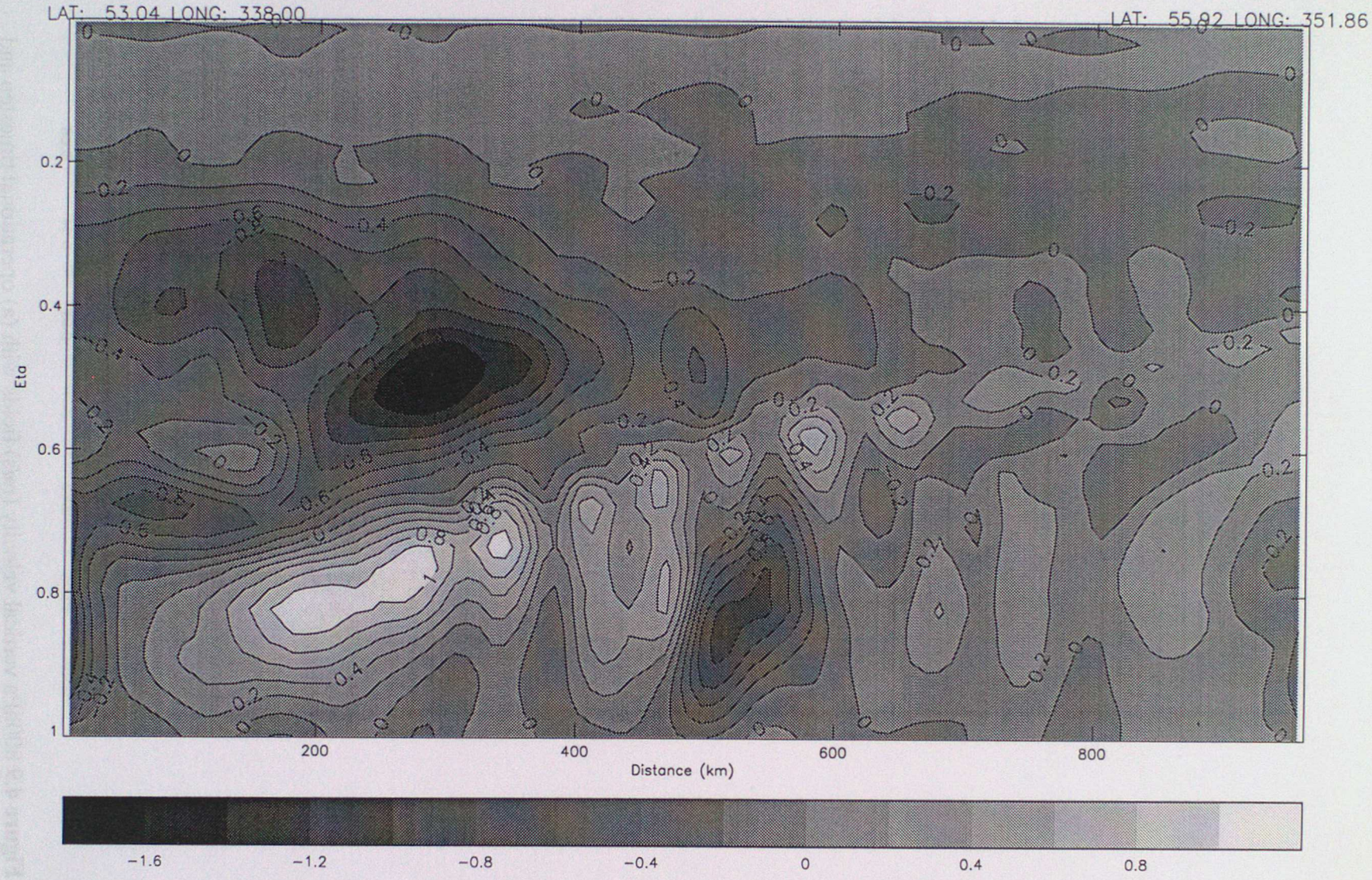

Figure 4.10 Along-front cross section of vertical velocity (m/s) showing breaking up of slanted structure.

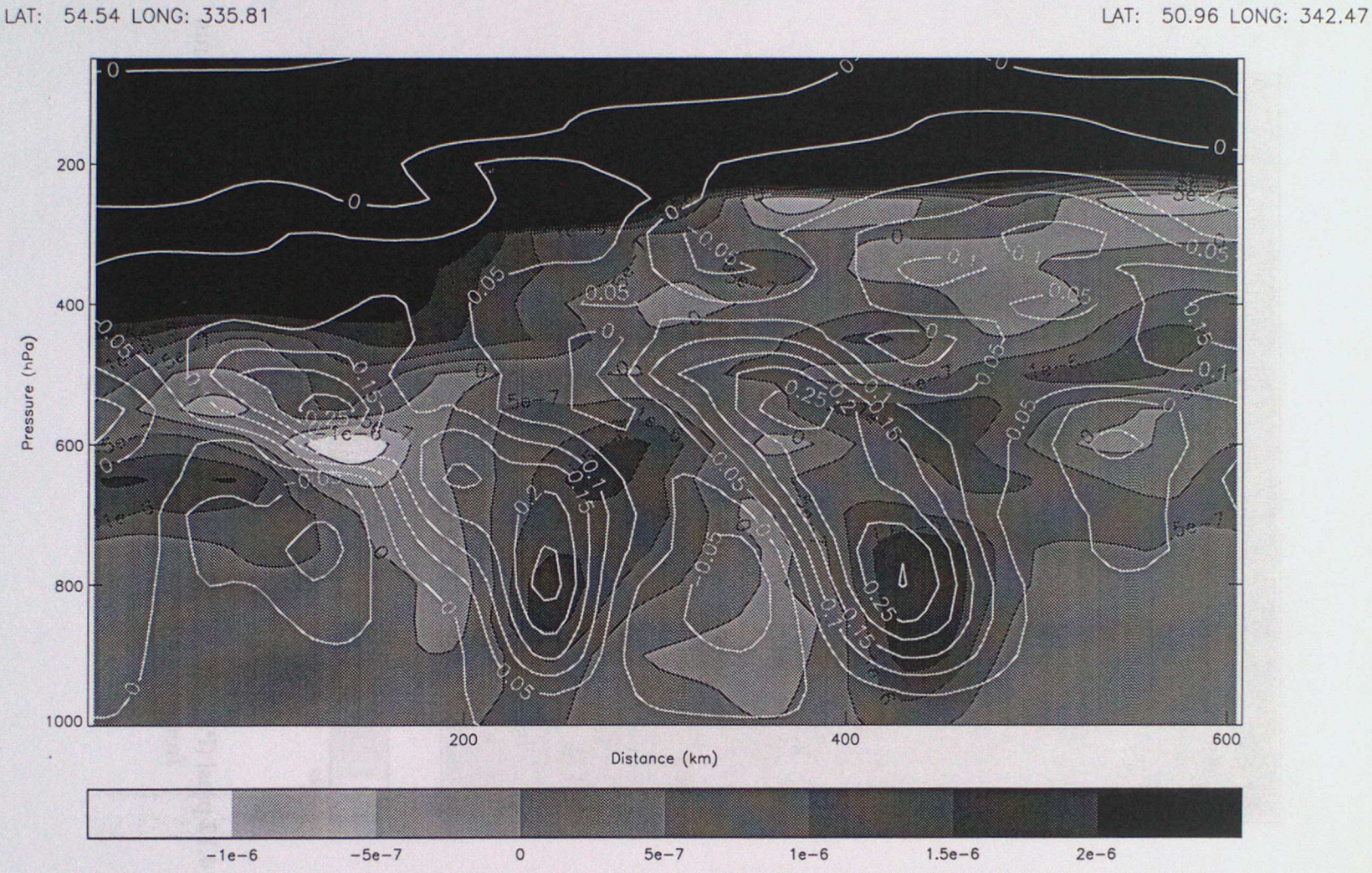

Figure 4.11 Potential vorticity (shaded) and vertical velocity (m/s) (contoured) for the same cross section as Figure 4.6

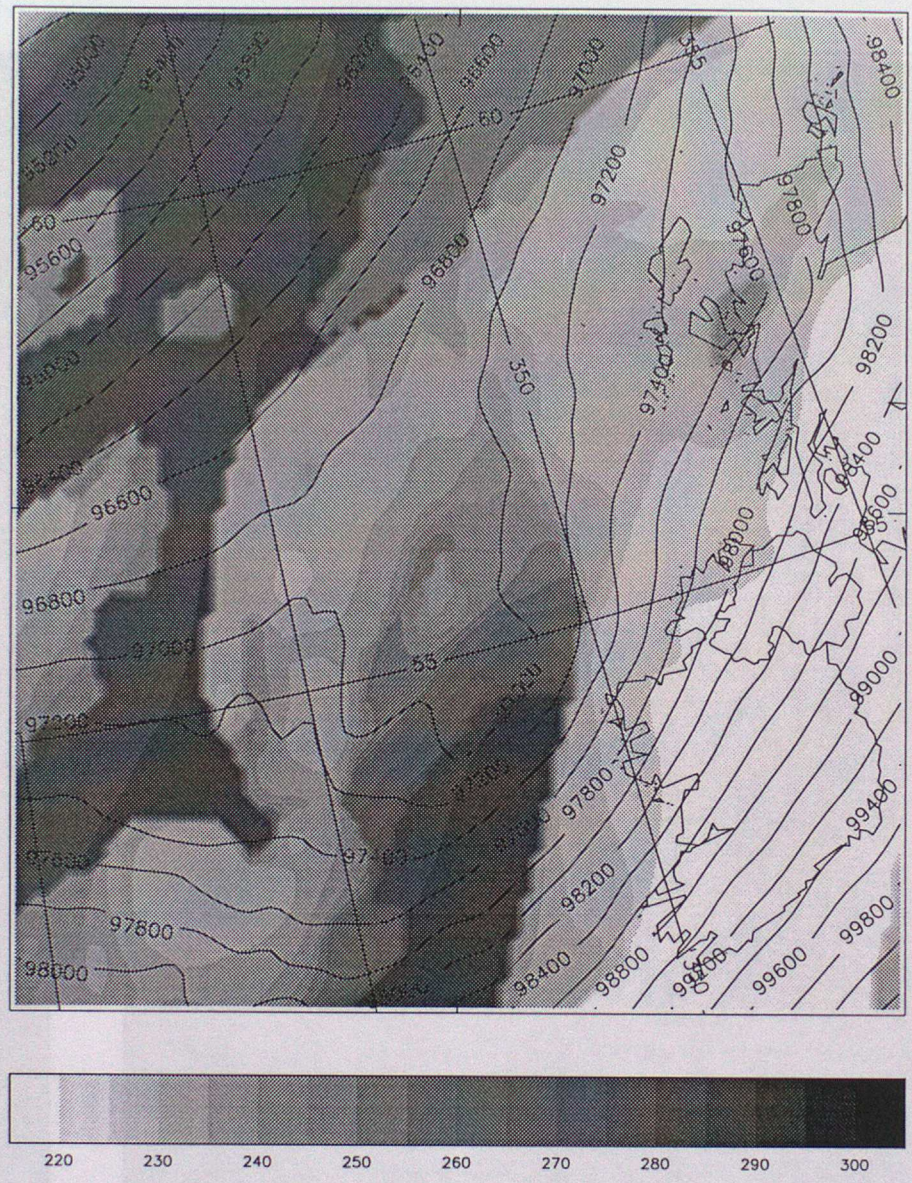

Figure 4.12 pmsl (Pa) and cloud top temperature (K) at 12Z 17th in the mesoscale run from the 18Z 16th High Resolution Global analysis.

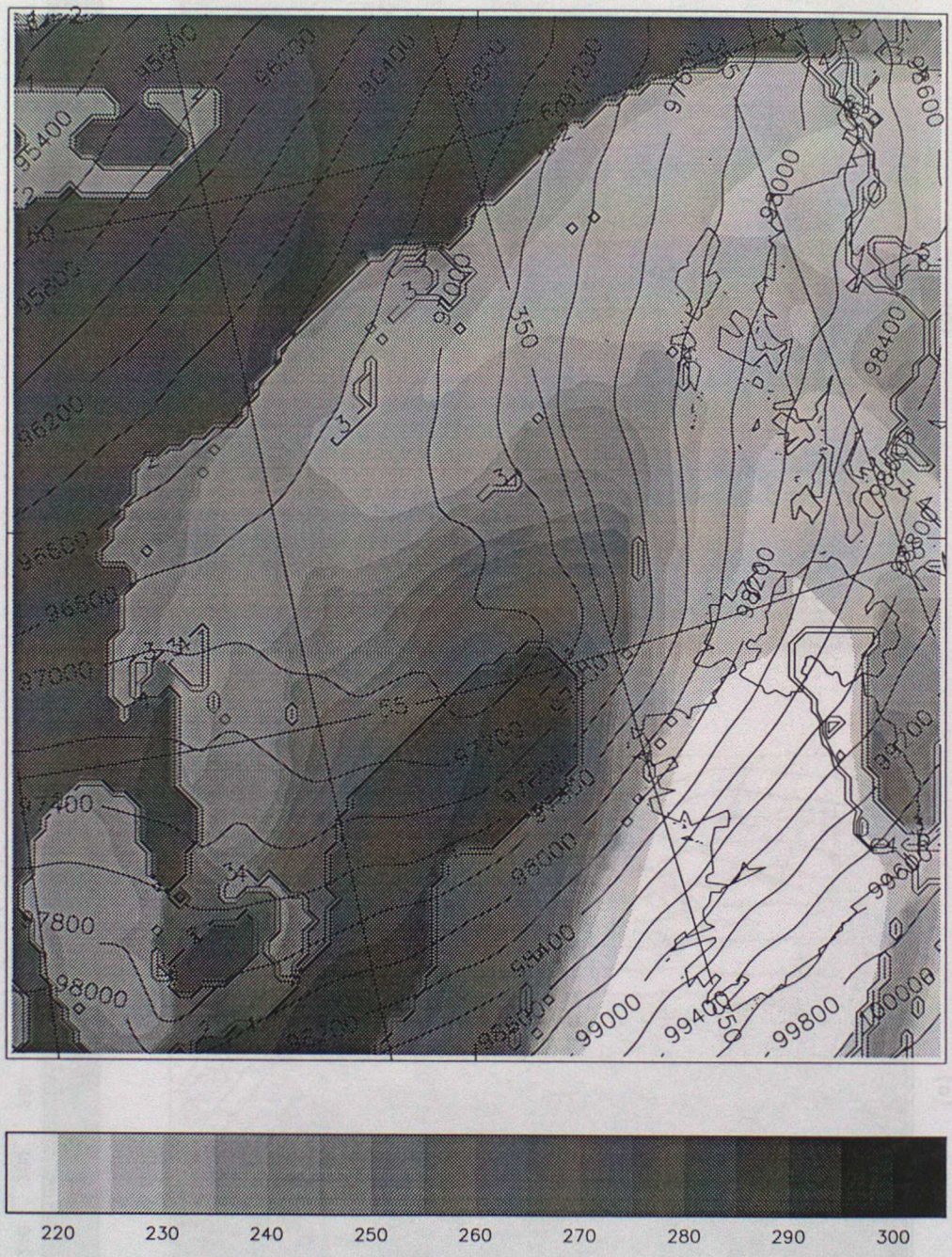

Figure 4.13 pmsl (Pa) and cloud top temperature (K) at 12Z 17th in the mesoscale run from the 18Z 16th ECMWF analysis (with High Resolution Global boundary conditions).

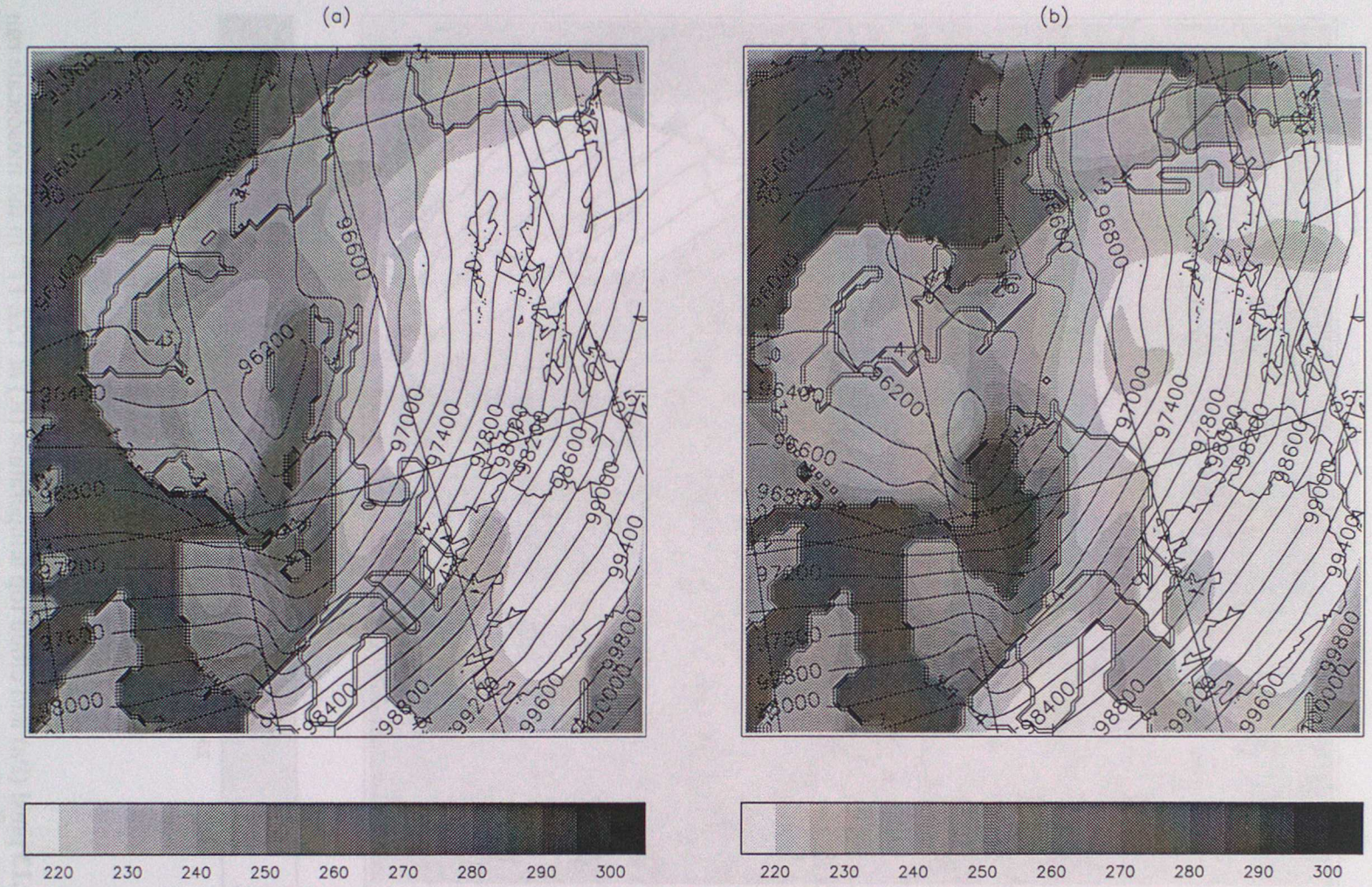

Figure 4.14 12Z 17th pmsl (Pa) and cloud top temperature (K) for the mesoscale analyses (a) with and (b) without FASTEX sondes.

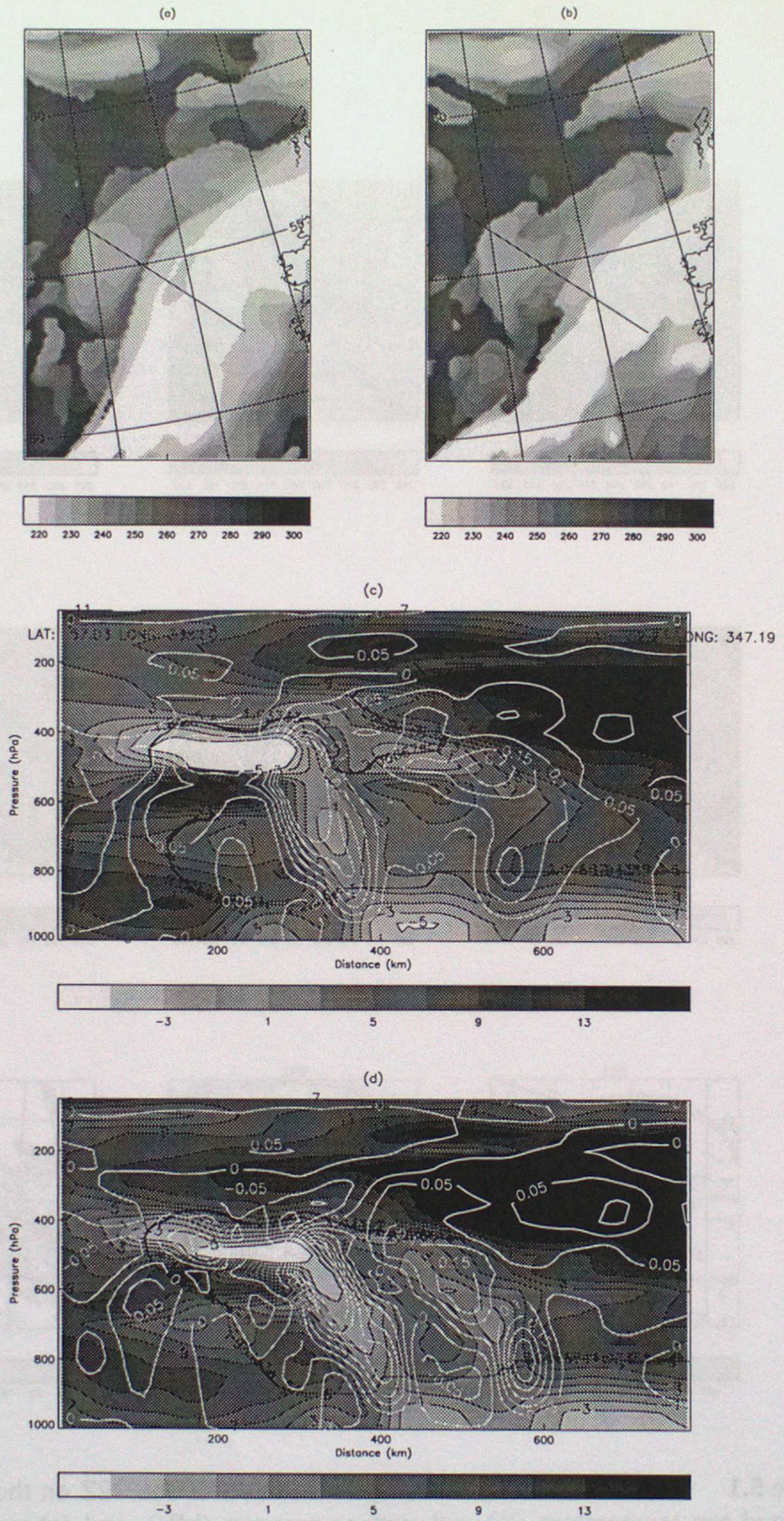

Figure 4.15 Cloud top temperature (K) from (a) 9Z analysis including FASTEX sondes and (b) T+9 forecast (valid at 9Z). (c) and (d) are cross sections along the lines shown in (a) and (b) respectively. In the cross sections the background shading shows the cross-frontal velocity (m/s) (negative means towards cold side, i.e. left in the cross-section plane), white contours are vertical velocity (m/s) and the thick black contour shows the cloud ice with the same threshold as used for the cloud top temperature charts.

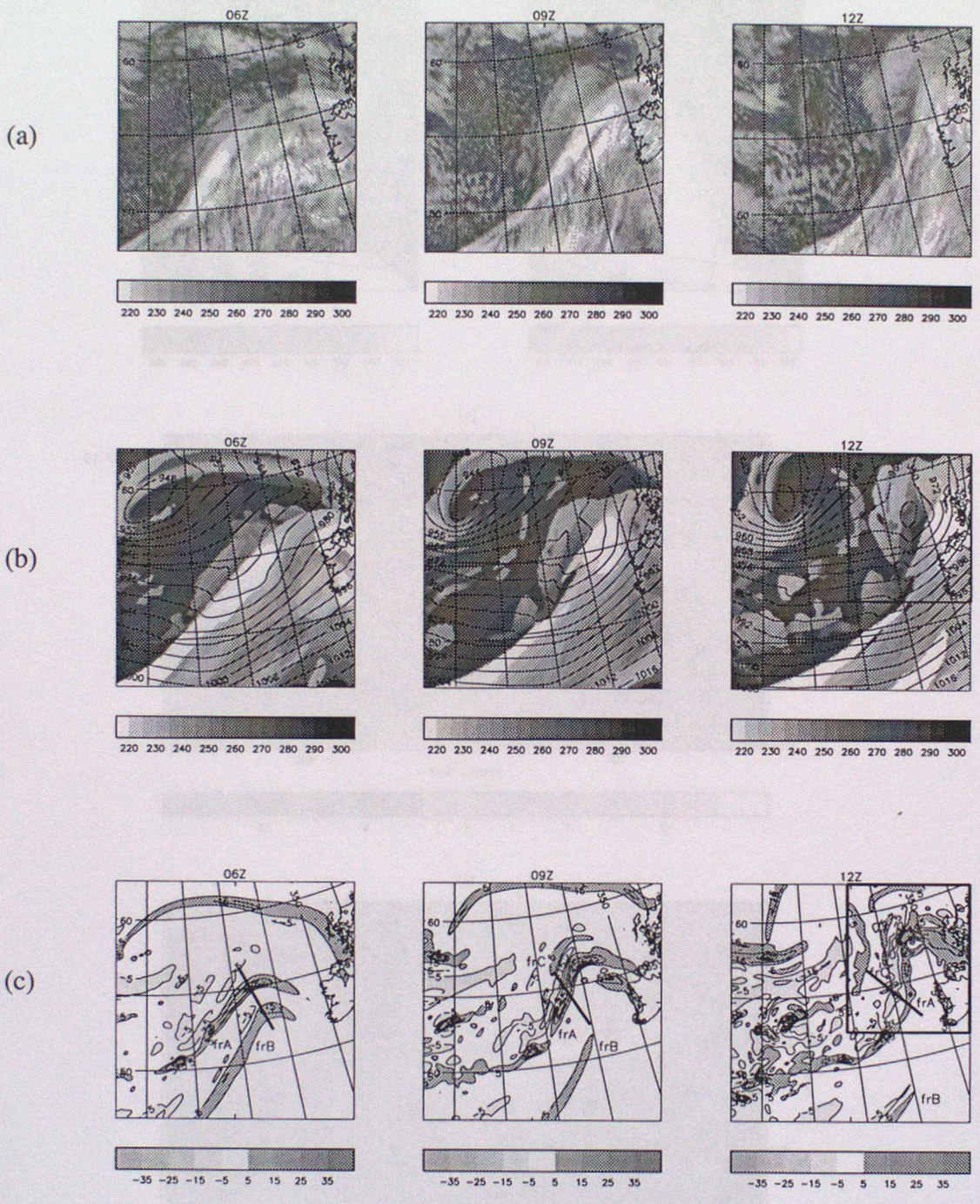

Figure 5.1 (a) Infra-red satellite image for 06Z, 09Z and 12Z on the 17/02/97. (b) Ice cloud top temperature (K) and surface pressure (hPa), and (c) vertical velocity (cm/s) at 800hPa from the 12km 45 level reference model forecast (REF) run from the 18Z LAM analysis. The box marked in the right hand corner of the 12Z image is the area used in the rest of the Figures. The labels frA, frB and frC in (c) identify the three fronts associated with those seen in the observations (see Fig. 2.5). The short solid line marks the approximate P3 aircraft flight track shifted system relative; leg 2 on the 06Z image, leg 4 on the 09Z image and leg 6 on the 12Z image.

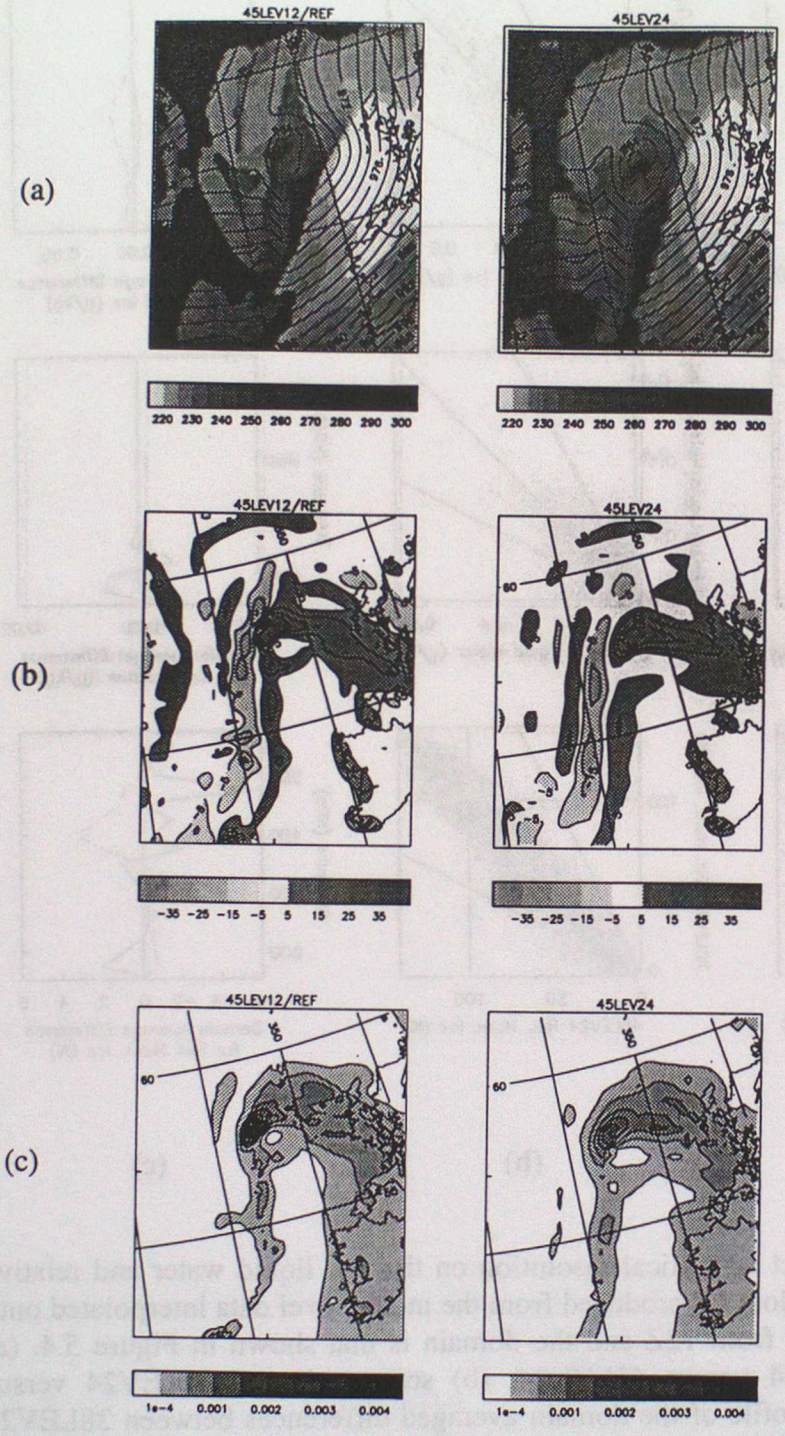

Figure 5.2 (a) Ice cloud top temperature (K) and surface pressure (hPa), (b) vertical velocity (cm/s) at 800hPa and (c) large scale surface rainfall ($kg/m^2/s$) for the 45LEV12/REF and 45LEV24 model forecasts at 12Z.

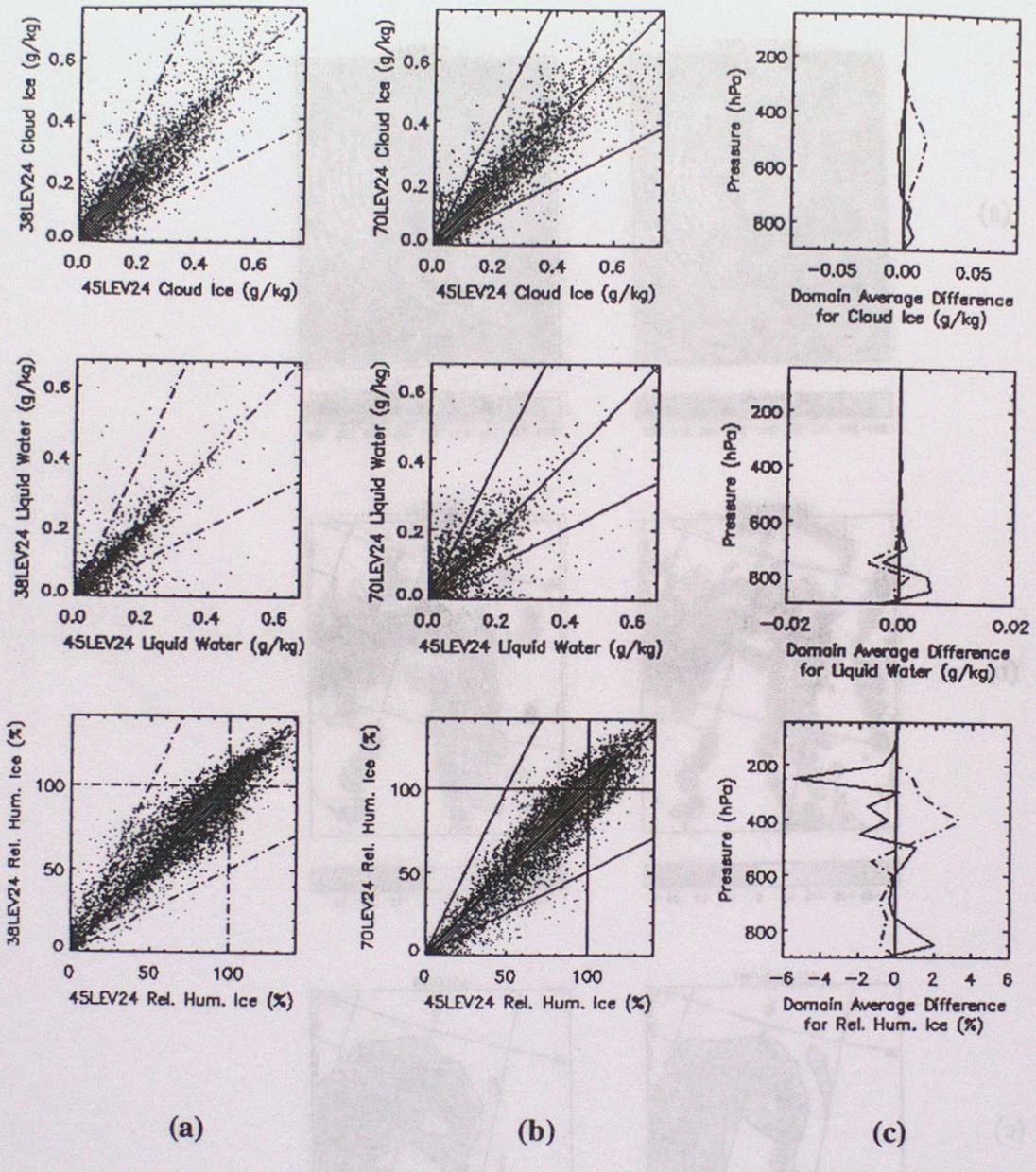

Figure 5.3 The impact of vertical resolution on the ice, liquid water and relative humidity fields. Scatter plots are produced from the model level data interpolated onto 50hPa levels. All data is from 12Z and the domain is that shown in Figure 5.4. (a) Scatter plot of 38LEV24 versus 45LEV24, (b) scatter plot of 70LEV24 versus 45LEV24, (c) vertical profile of the domain averaged differences between 38LEV24 and 45LEV24 (dot-dash line) and 70LEV24 and 45LEV24 (solid line).

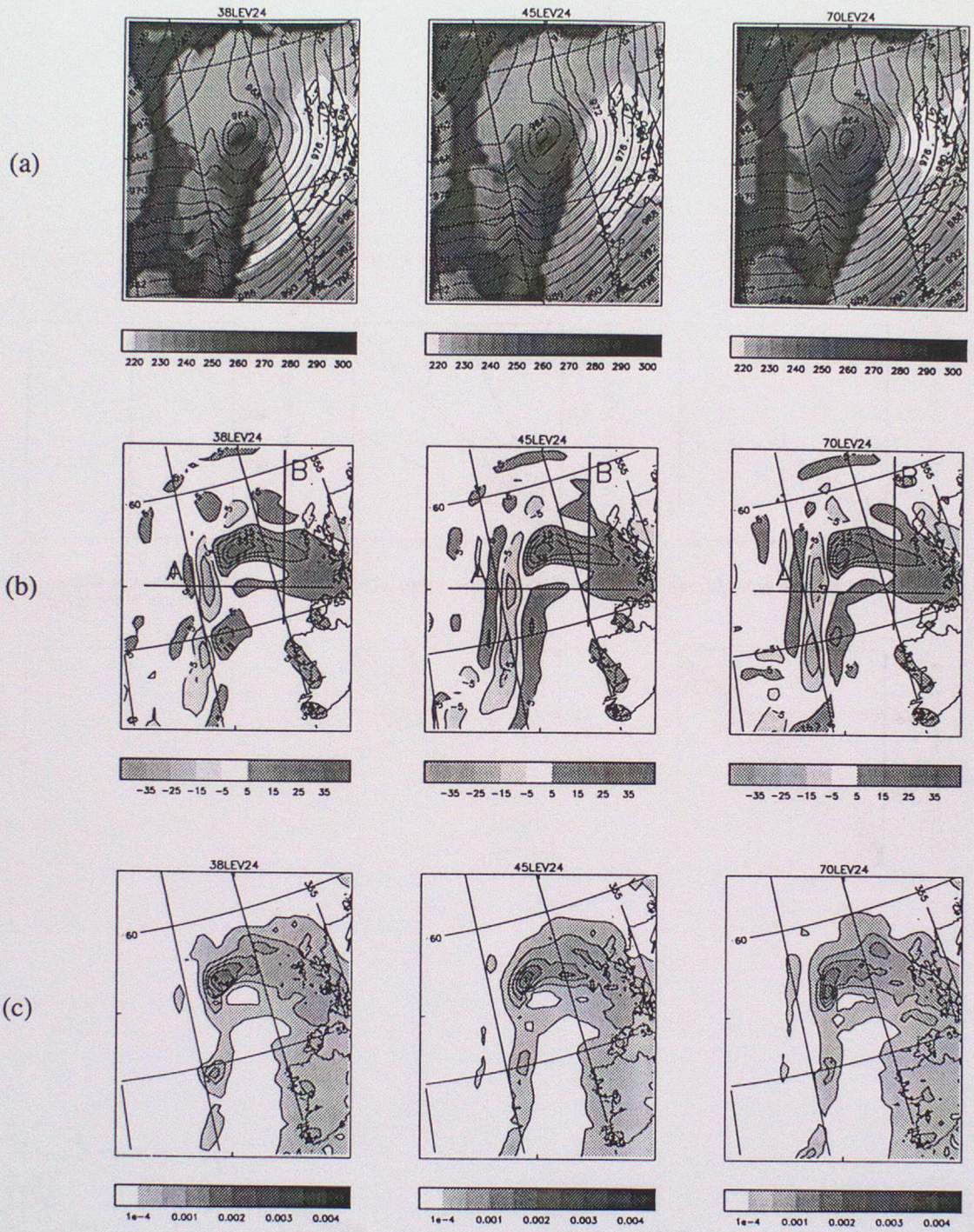

Figure 5.4 (a) Ice cloud top temperature (K) and surface pressure (hPa), (b) vertical velocity (cm/s) at 800hPa and (c) large scale surface rainfall (kg/m^2/s) for 38LEV24, 45LEV24 and 70LEV24 model forecasts at 12Z, 18 hours into the forecast.

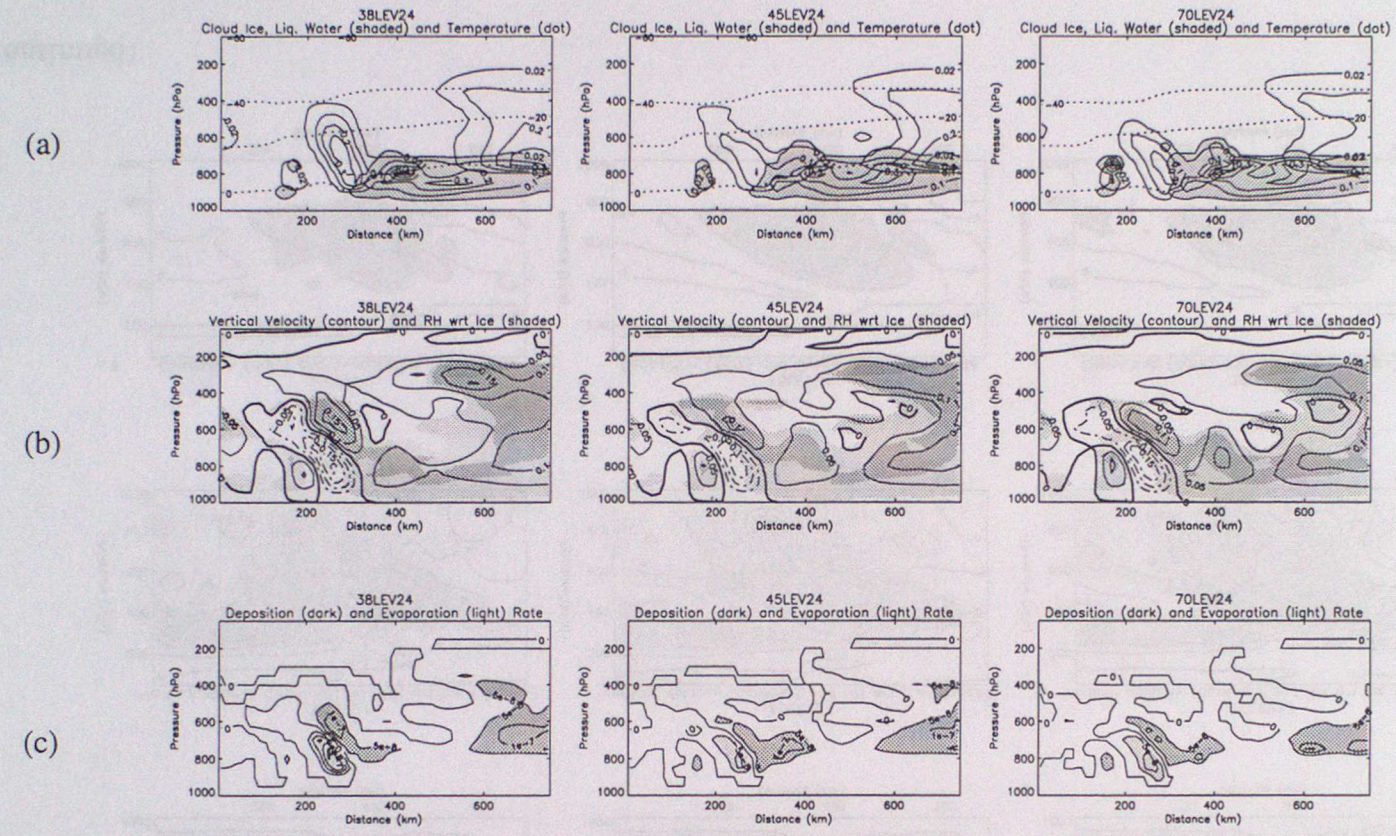

Figure 5.5 Vertical cross-section through the cold front trough (marked 'A' in Figure 5.4) for 38LEV24, 45LEV24 and 70LEV24. (a) Ice content [g/kg] (unfilled contours), liquid water content [g/kg] (filled contours) and temperature [°C] (dotted line), (b) vertical velocity [m/s] (solid contours for upward motion, dot-dash contours for downward motion and double thickness contour for zero vertical motion) and relative humidity with respect to ice [%] (light shading for RH>85%, heavy shading for RH>100% and heavier for RH>120%), (c) ice deposition rate [kg/kg/s] (deposition > 5e-8 kg/kg/s is heavily shaded, evaporation > 5e-8 kg/kg/s is lightly shaded), (d), (e) and (f) are vertical cross-sections of the same quantities as (a), (b) and (c) but are through the warm front trough (marked 'B' in Figure 5.4).

(d)

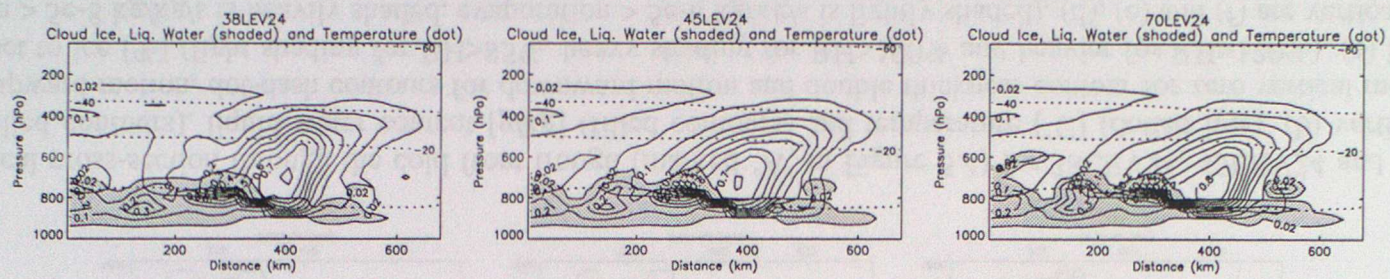

(e)

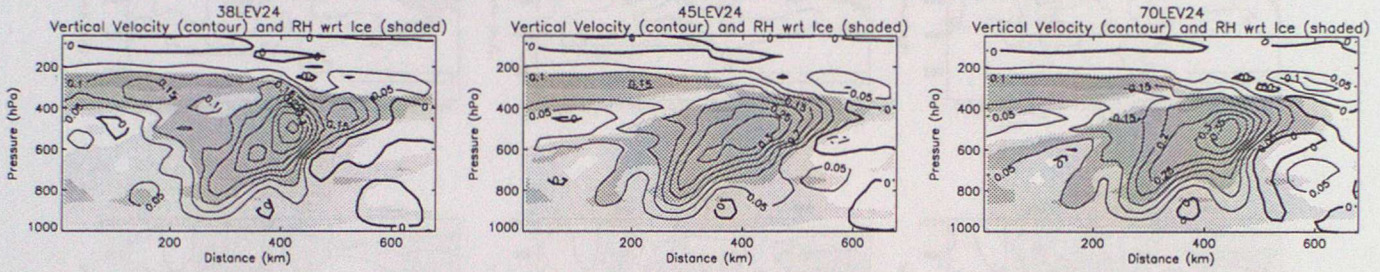

(f)

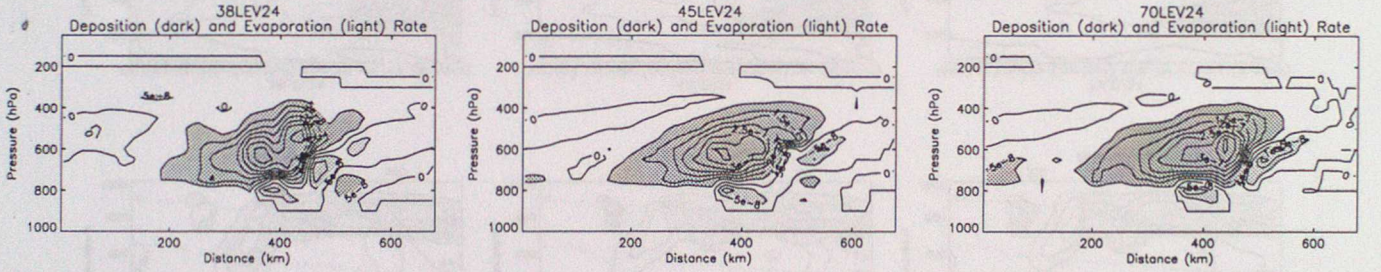

Figure 5.5 (continued)

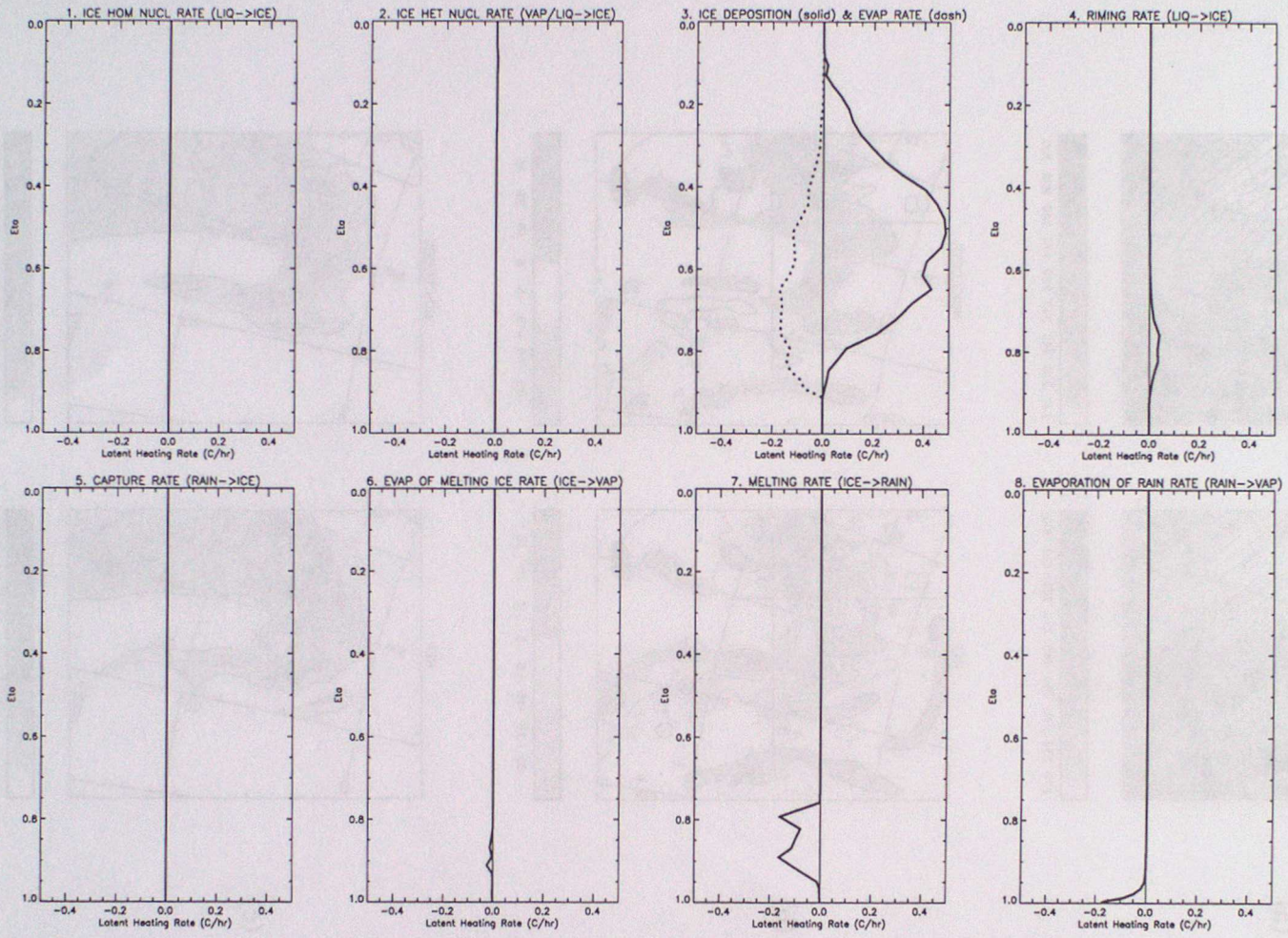

Figure 5.6 Vertical profiles of domain averaged latent heating rates (°C/hour) from the mixed-phase microphysics scheme. The averages are formed on each model level at 12Z on 17/02/97 for the domain shown in Figure 5.7 covering the low centre and associated frontal zones.

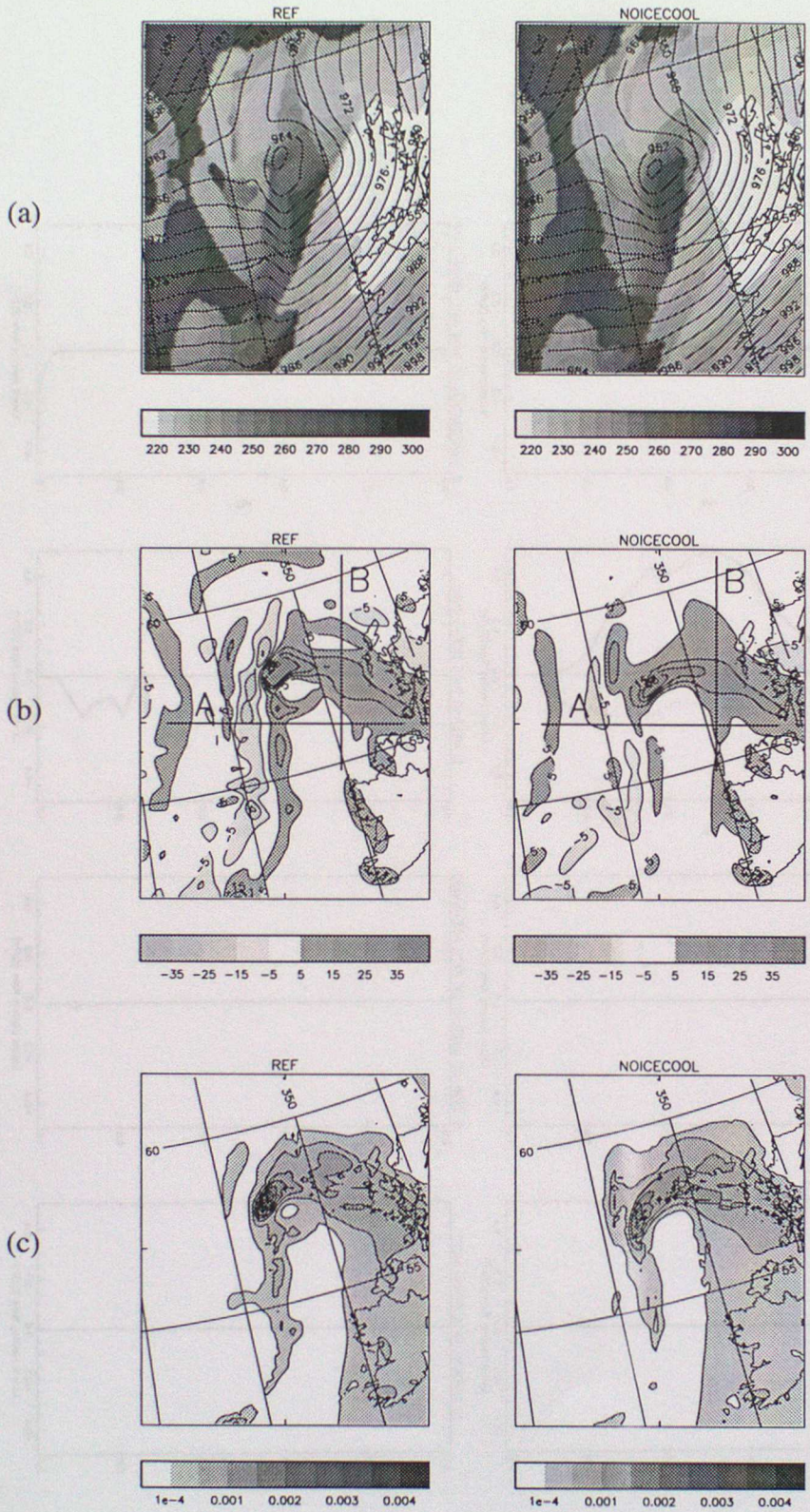

Figure 5.7 As for Figure 5.4 but (a) ice cloud top temperature (K) and surface pressure (hPa), (b) vertical velocity (cm/s) at 800hPa and (c) large scale surface rainfall ($kg/m^2/s$) for REF and NOICECOOL at 12Z.

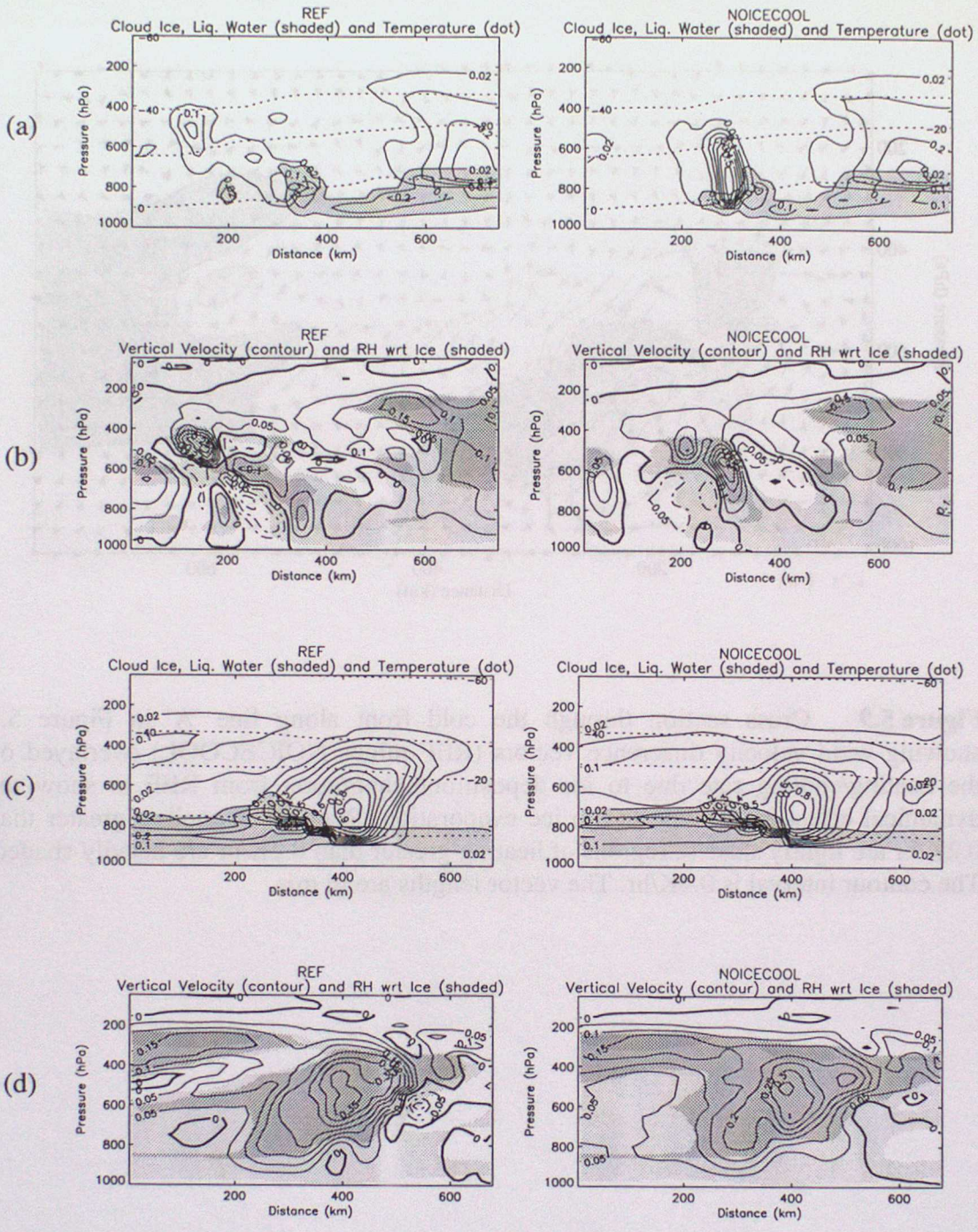

Figure 5.8 As for Figure 5.5 but vertical cross-sections through the troughs in REF and NOICECOOL. (a) and (b) correspond to line 'A' in Figure 5.7. (c) and (d) correspond to line 'B' in Figure 5.7.

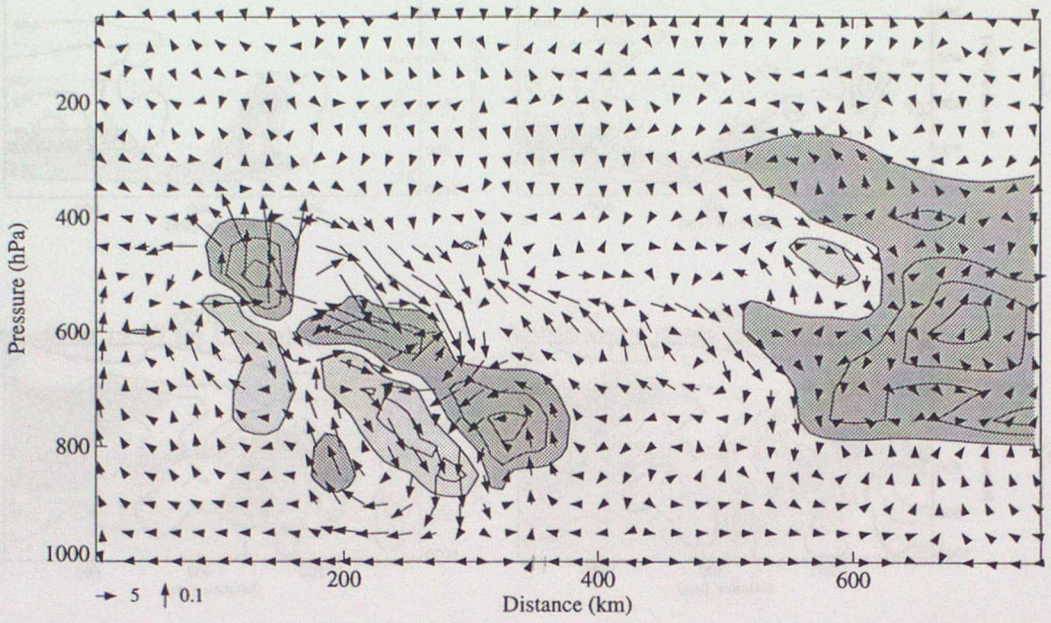

Figure 5.9 Cross section through the cold front along line 'A' in Figure 5.7 showing wind velocity difference vectors (REF minus NOICECOOL) overlayed on the heating/cooling rate due to ice deposition/evaporation from REF to show the dynamical effect of cooling due to ice evaporation. Regions of cooling greater than 0.2K/hr are lightly shaded, regions of heating greater than 0.2K/hr are heavily shaded. The contour interval is 0.4K/hr. The vector lengths are in m/s.

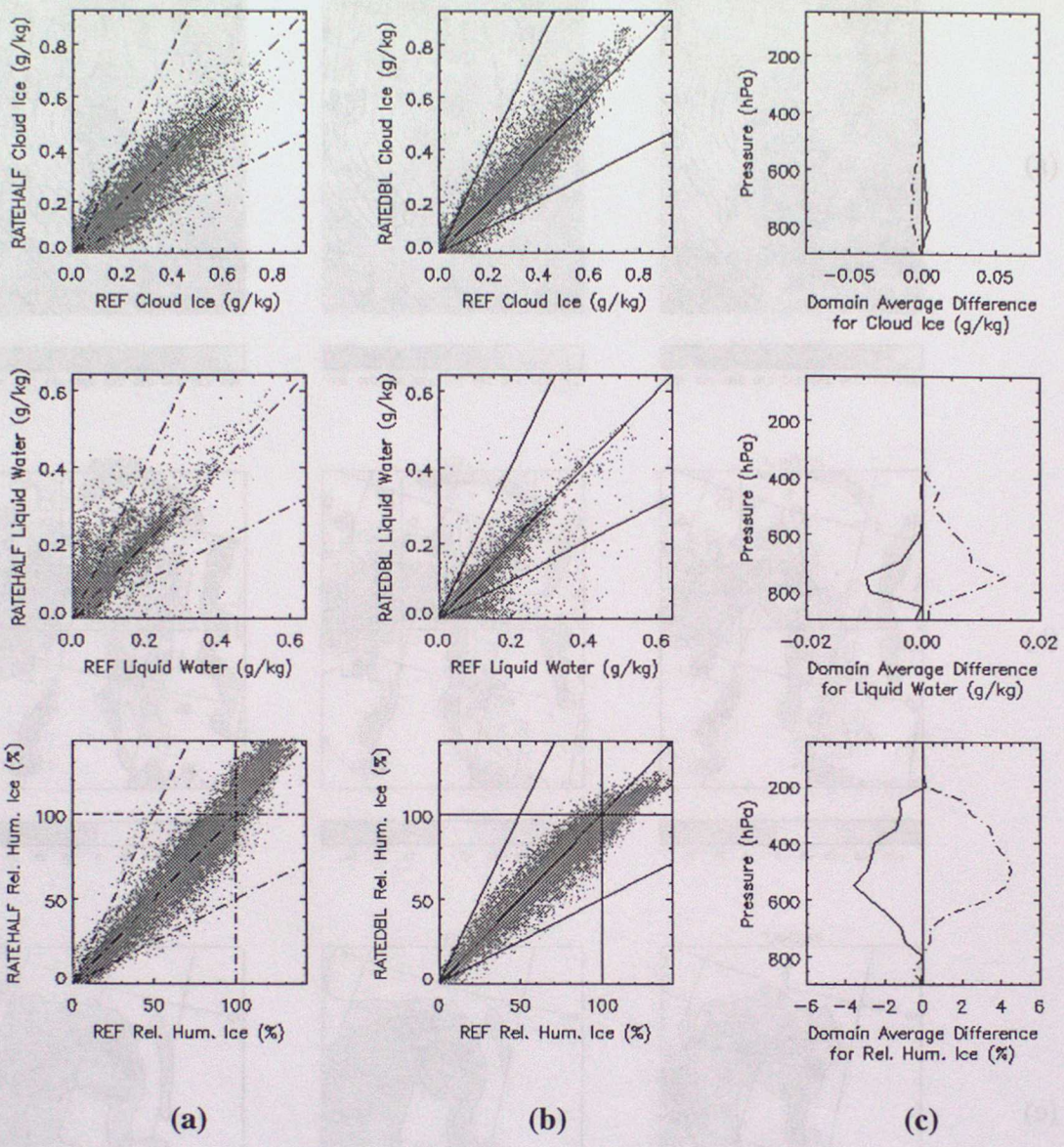

Figure 5.10 As for Figure 5.3 but showing the impact of changing the ice deposition/evaporation rate on the, ice, liquid water, relative humidity fields. (a) Scatter plot of RATEHALF versus REF, (b) Scatter plot of RATEDBL versus REF, (c) vertical profile of the domain averaged differences between RATEHALF and REF (dot-dash line) and RATEDBL and REF (solid line).

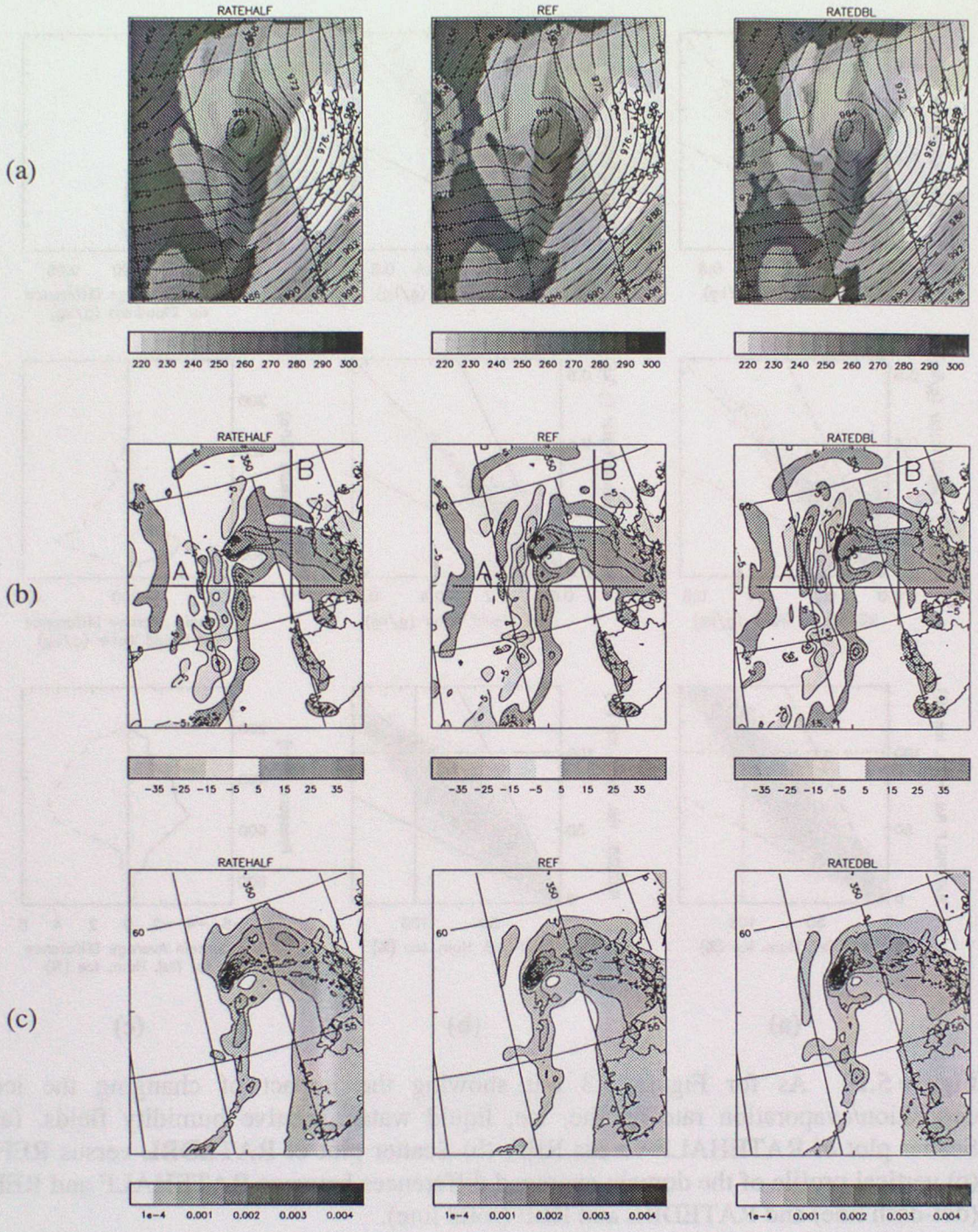

Figure 5.11 As for Figure 5.4 but (a) ice cloud top temperature (K) and surface pressure (hPa), (b) vertical velocity (cm/s) at 800hPa and (c) large scale surface rainfall ($kg/m^2/s$) for RATEHALF, REF and RATEDBL at 12Z.

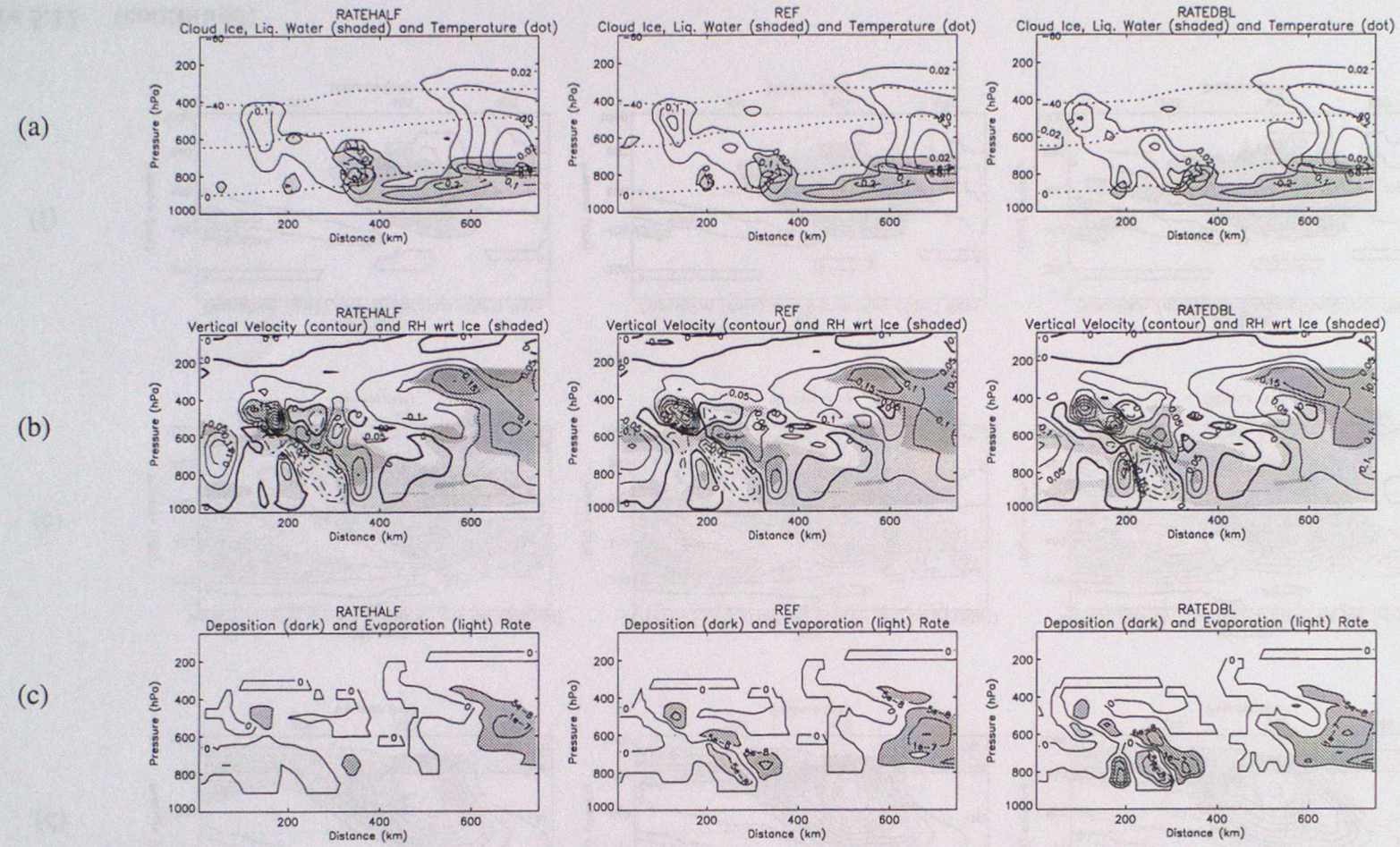

Figure 5.12 As for Figure 5.5 but vertical cross-sections through the troughs in RATEHALF, REF and RATEDBL. (a), (b), (c) correspond to line 'A' in Figure 5.11. (d), (e), (f) correspond to line 'B' in Figure 5.11.

(d)

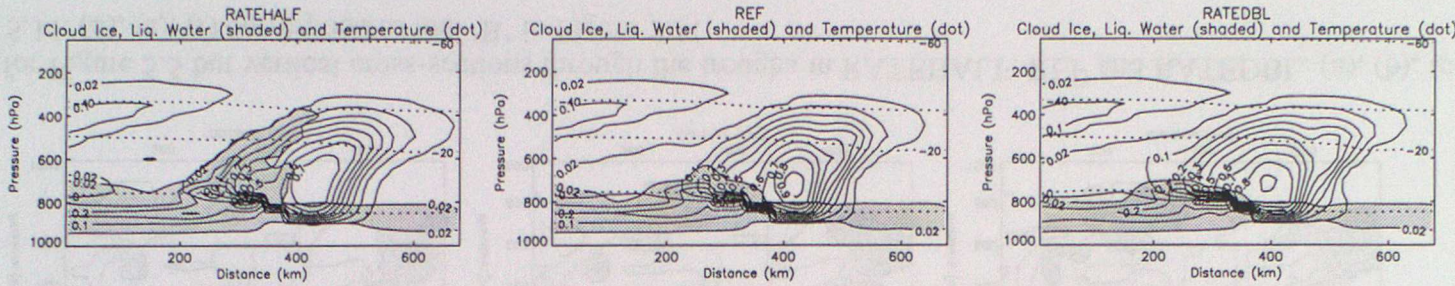

(e)

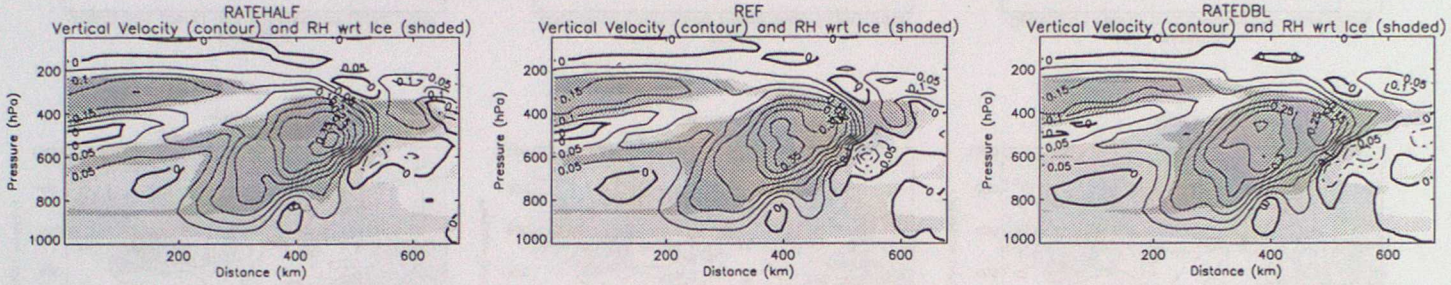

(f)

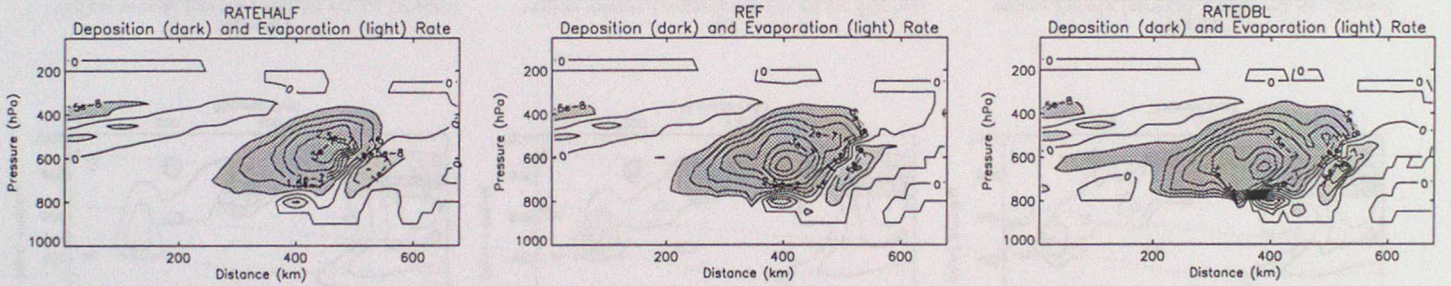

Figure 5.12 (continued)

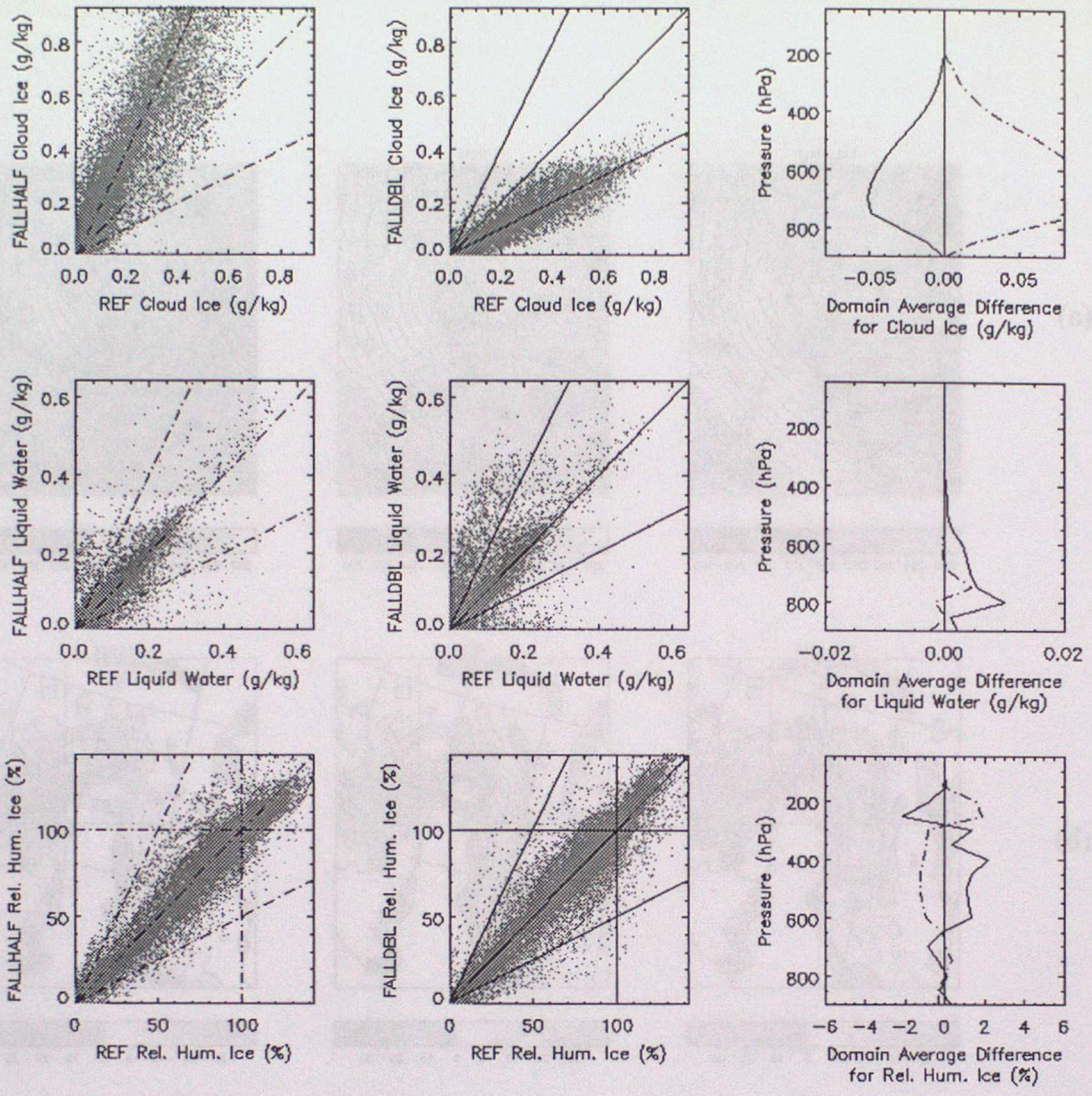

Figure 5.13 As for Figure 5.3 but showing the impact of changing ice particle fall speed on the, ice, liquid water and relative humidity fields. (a) Scatter plot of FALLHALF versus REF, (b) Scatter plot of FALLDBL versus REF, (c) vertical profile of the domain averaged differences between FALLHALF and REF (dot-dash line) and FALLDBL and REF (solid line).

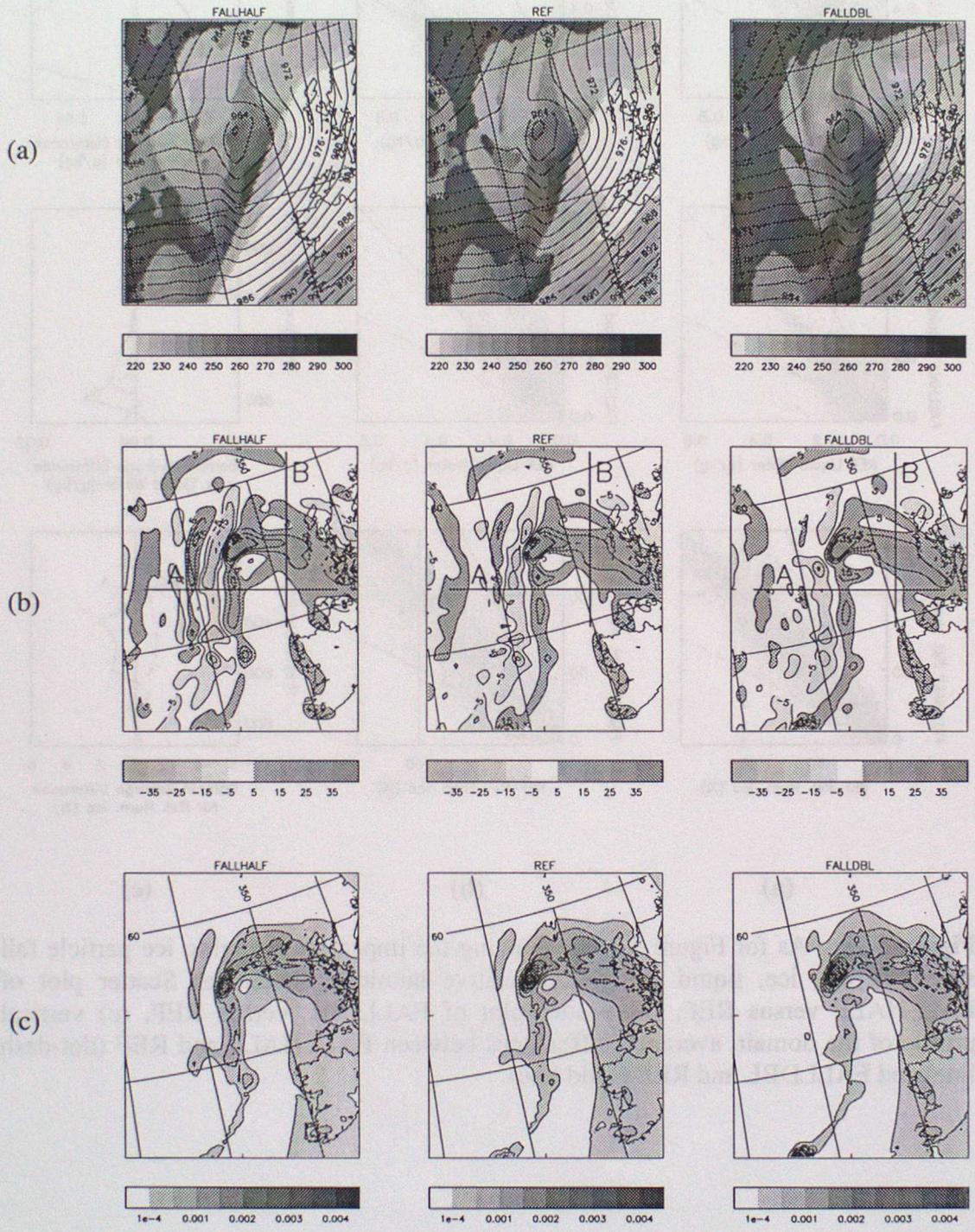

Figure 5.14 As for Figure 5.4 but (a) ice cloud top temperature (K) and surface pressure (hPa), (b) vertical velocity (cm/s) at 800hPa and (c) large scale surface rainfall ($kg/m^2/s$) for FALLHALF, REF and FALLDBL.

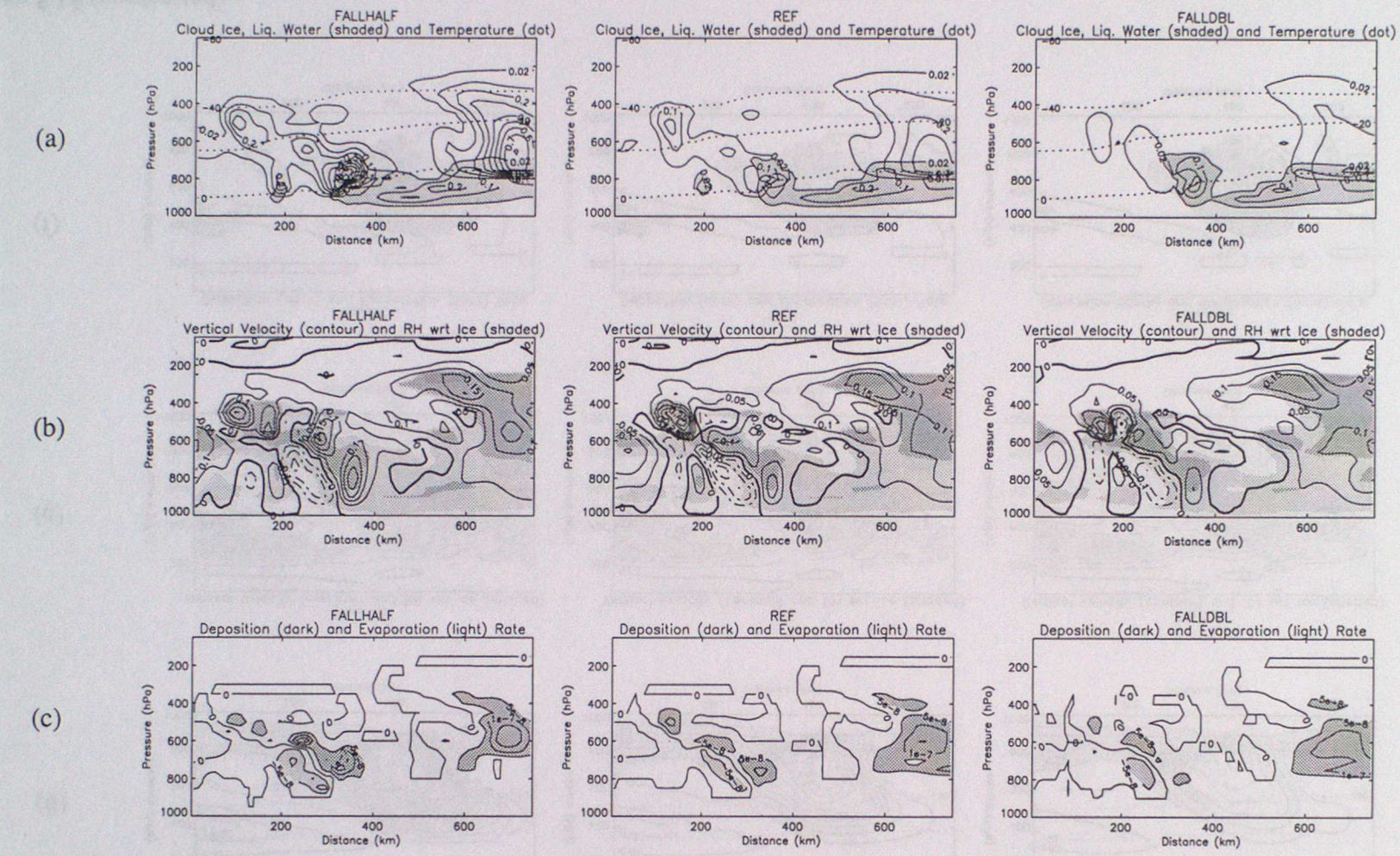

Figure 5.15 As for Figure 5.5 but vertical cross-sections through the troughs in FALLHALF, REF and FALLDBL. (a), (b), (c) correspond to line 'A' in Figure 5.14, (d), (e), (f) correspond to line 'B' in Figure 5.14.

(d)

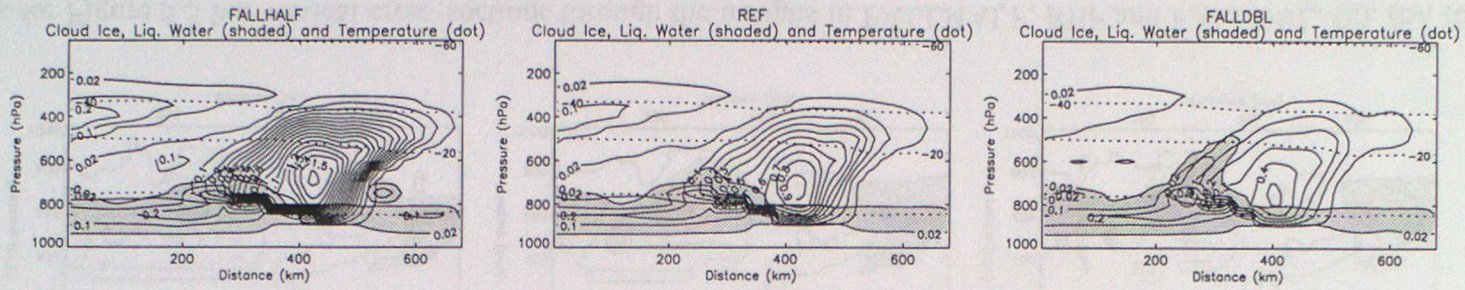

(e)

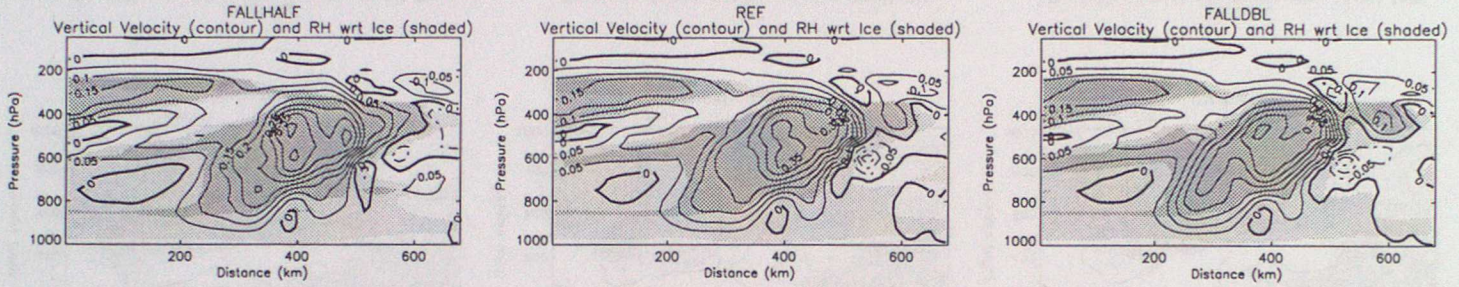

(f)

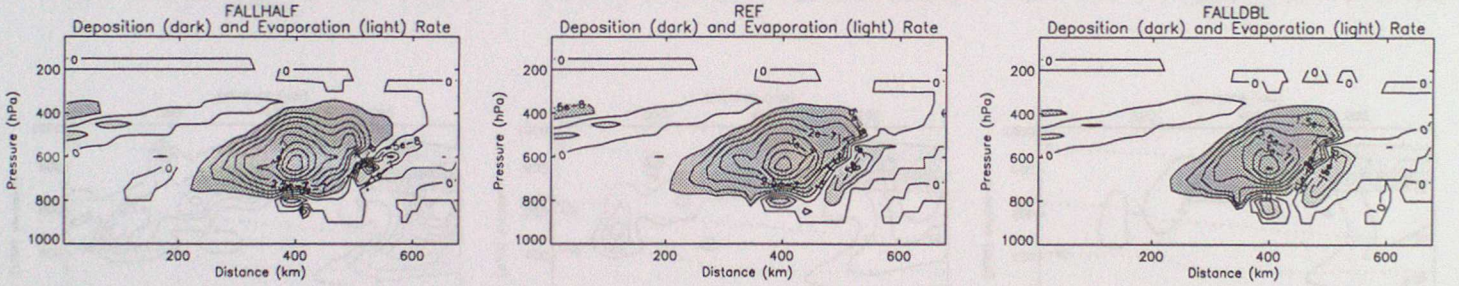

Figure 5.15 (continued)

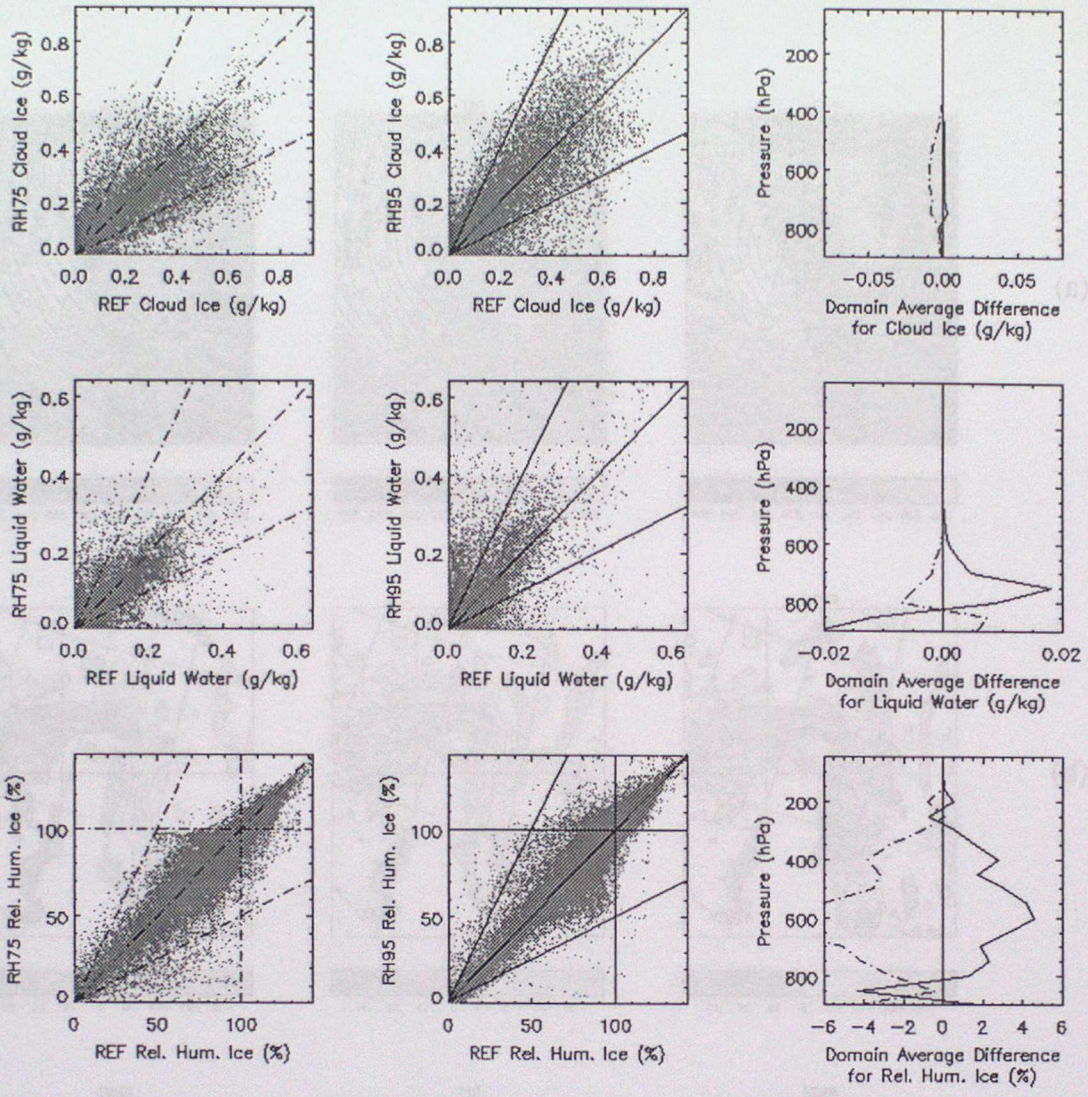

Figure 5.16 As for Figure 5.3 but showing the impact of changing RH_{crit} on the, ice, liquid water, relative humidity and vertical velocity fields. (a) Scatter plot of RH75 versus REF, (b) Scatter plot of RH95 versus REF, (c) vertical profile of the domain averaged differences between RH75 and REF (dot-dash line) and RH95 and REF (solid line).

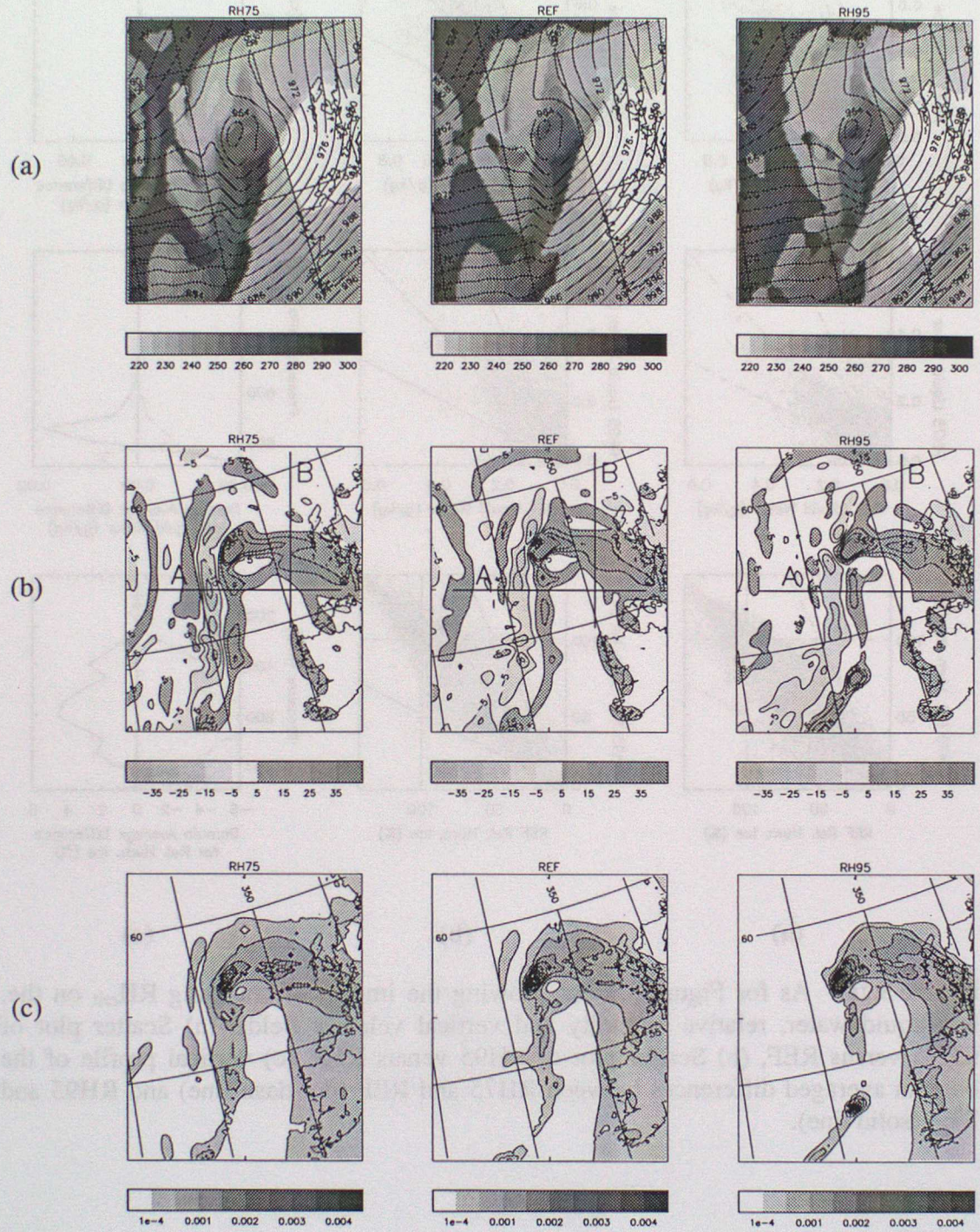

Figure 5.17 As for Figure 5.4 but (a) ice cloud top temperature (K) and surface pressure (hPa), (b) vertical velocity (cm/s) at 800hPa and (c) large scale surface rainfall (kg/m^2/s) for RH75, REF and RH95.

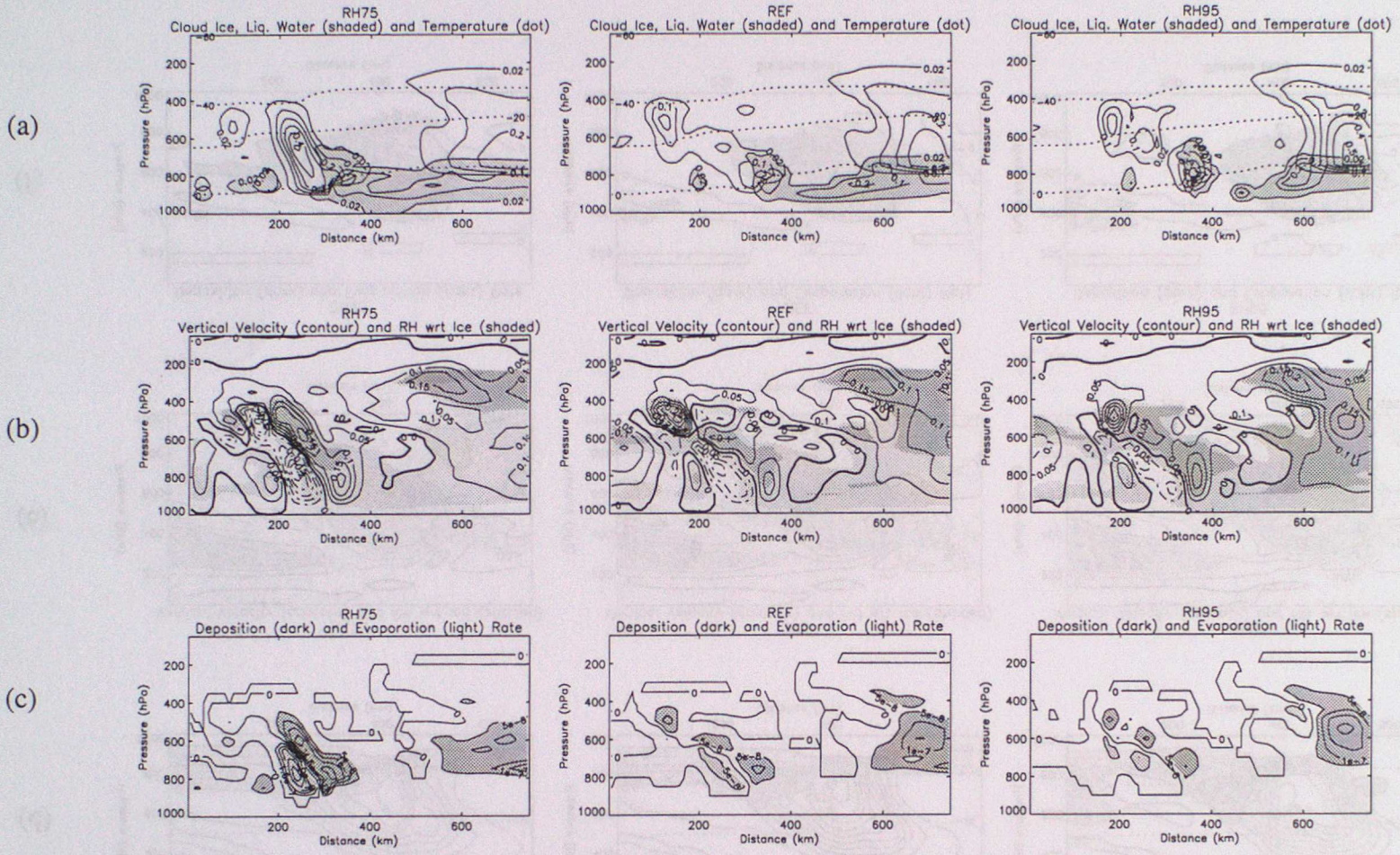

Figure 5.18 As for Figure 5.4 but vertical cross-sections through the troughs in RH75, REF and RH95. (a), (b), (c) correspond to line 'A' in Figure 5.17, (d), (e), (f) correspond to line 'B' in Figure 5.17.

(d)

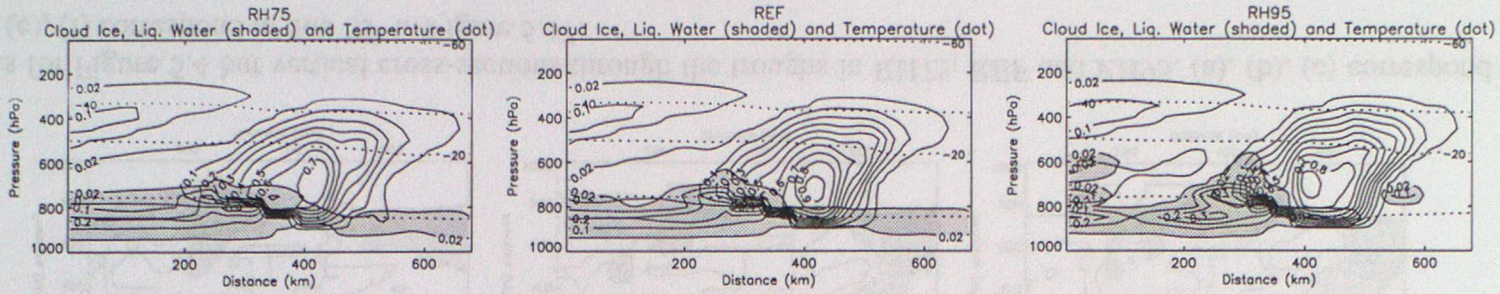

(e)

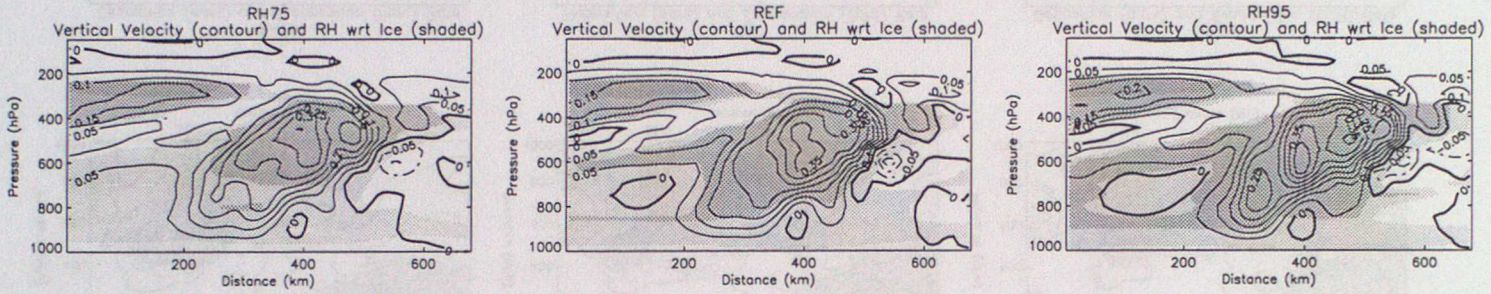

(f)

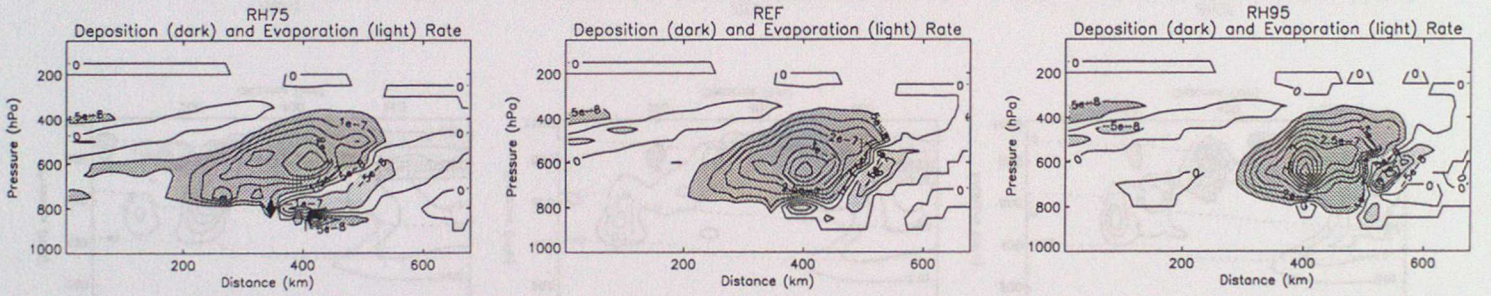

Figure 5.18 (continued)

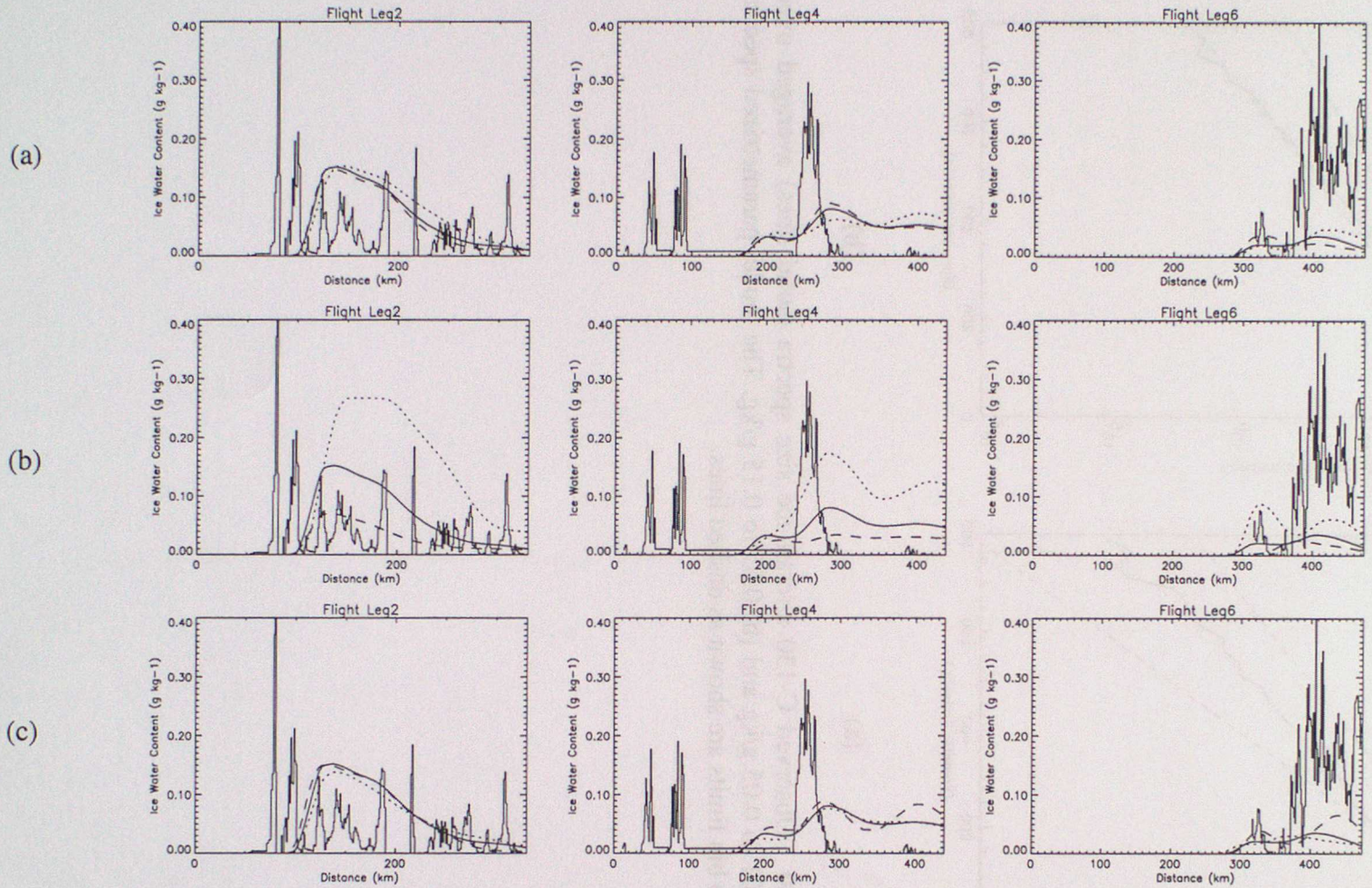

Figure 5.19 Observed C-130 aircraft ice water content along the flight path at 360hPa for flight legs 2, 4, and 6, overlayed values extracted from the model experiments. (a) half deposition rate (dotted), reference (solid) and double deposition rate (dashed), (b) half fall speed (dotted), reference (solid) and double fall speed (dashed), (c) RH_{crit}=0.75 (dotted), reference (solid) and RH_{crit}=0.95 (dashed).

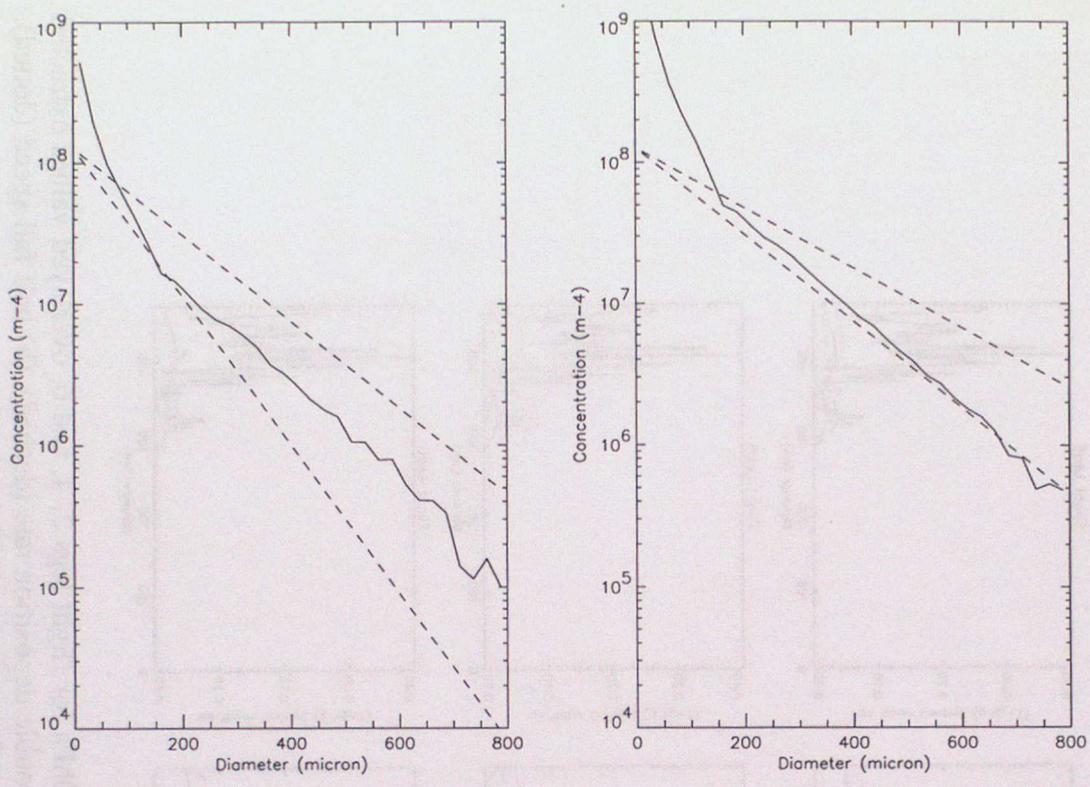

Figure 5.20 Observed C-130 aircraft ice size spectra (solid lines) averaged over bins (a) 0.01 to 0.05 g/kg and (b) 0.05 to 0.15 g/kg. The model parametrized spectra for the two bin limits are shown as dashed lines.

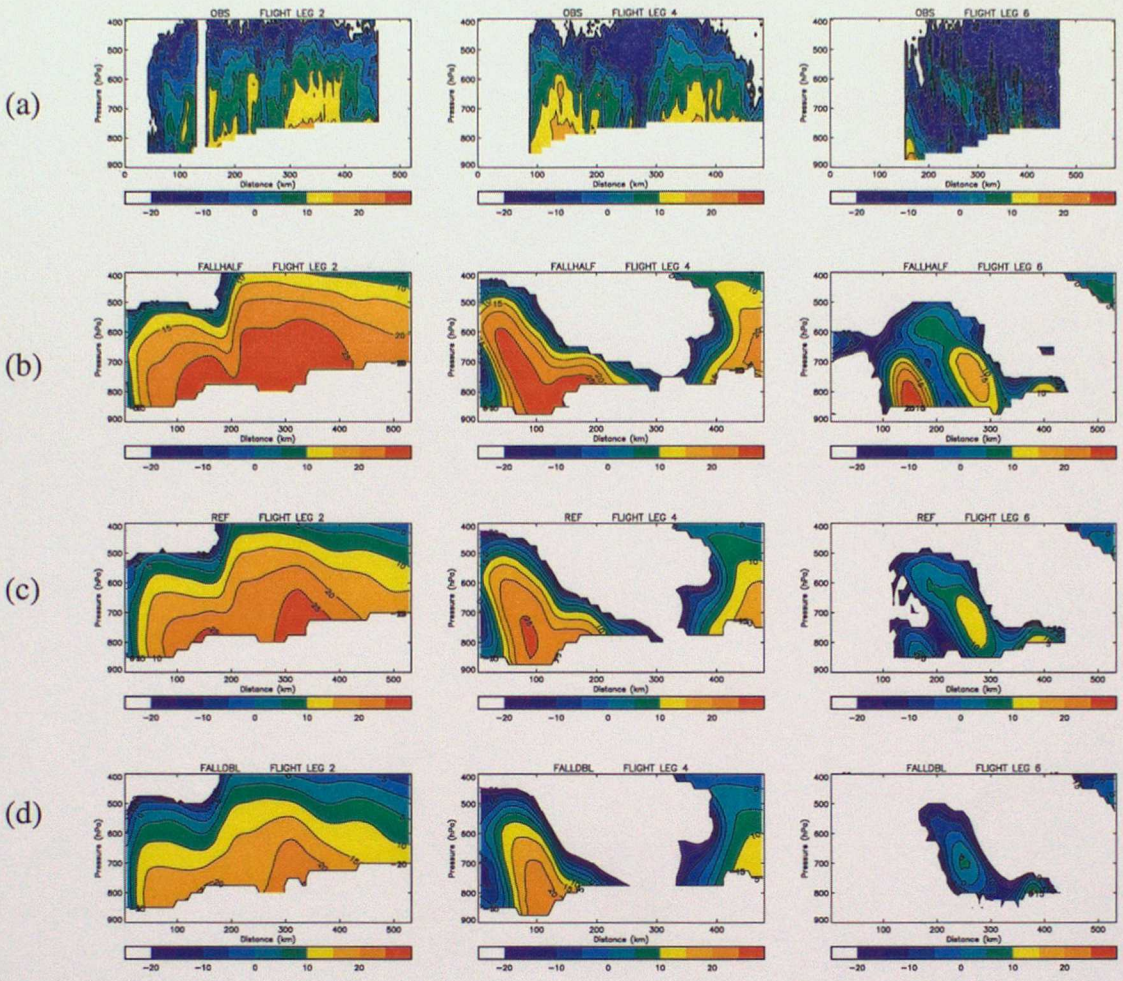

Figure 5.21 Radar reflectivity (dBZ) cross-sections along flight legs 2, 4, and 6 for (a) the P-3 observations, (b) the half fall speed experiment, (c) the reference run, and (d) the double fall speed experiment.

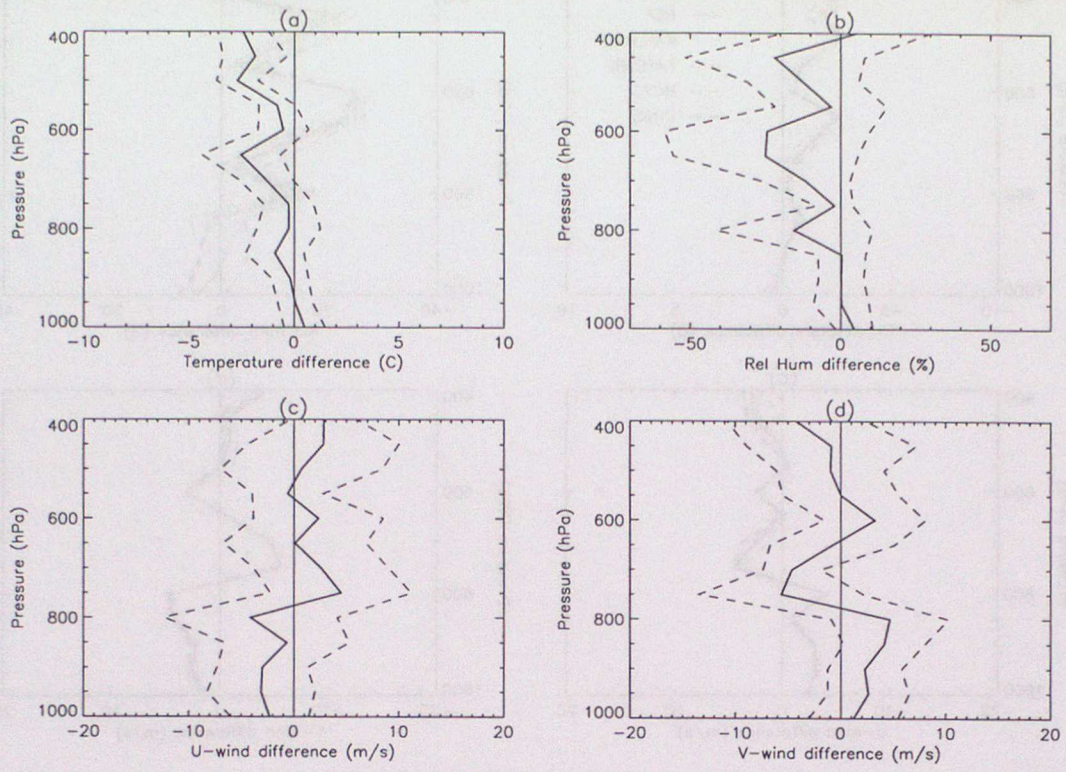

Figure 5.22 Vertical profiles of the mean (solid line) and standard deviation (dashed lines either side or the mean) of the differences between the reference model and the dropsonde observations (i.e. model minus obs.) for (a) temperature, (b) relative humidity with respect to water, (c) u-component of wind, and (d) v-component of wind. Three instantaneous model fields at 06Z, 09Z, and 12Z with dropsonde observations within 1 hour either side of these times were used for the calculation. All dropsonde positions were moved system relative for each model time. Values are calculated every 50hPa with over 30 sondes for each level.

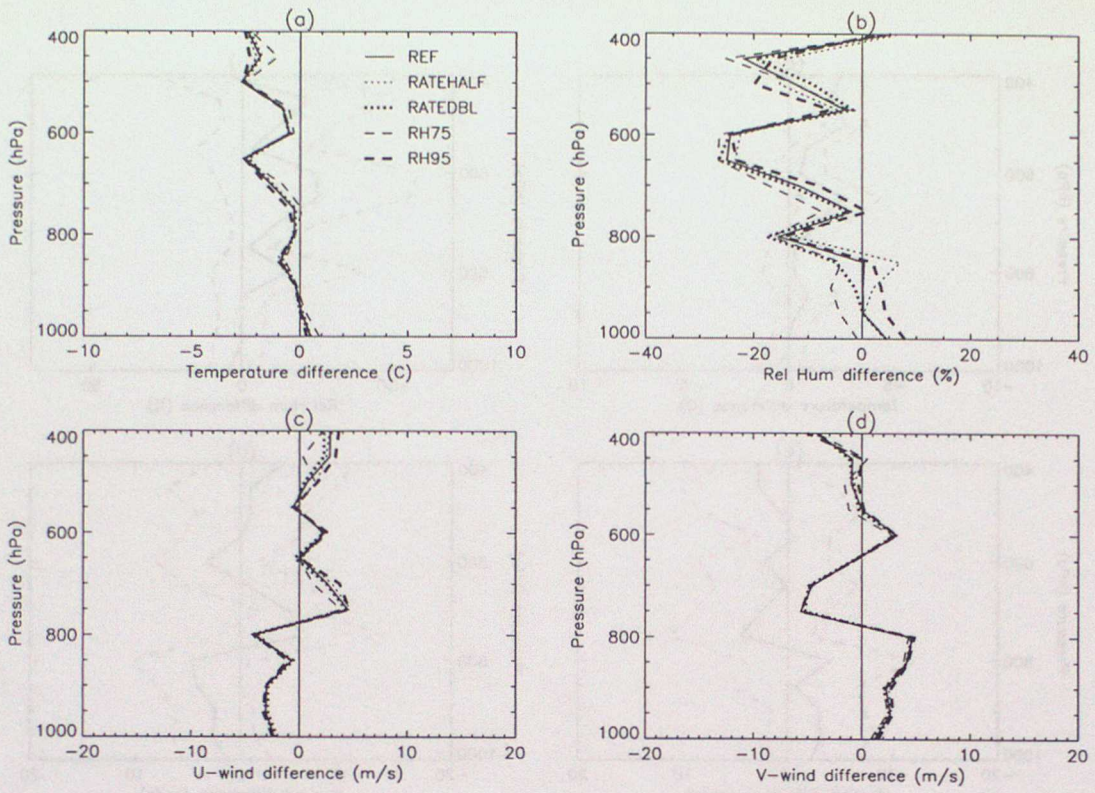

Figure 5.23 As for Figure 5.22 but showing the mean differences between model and dropsonde observations for the reference and deposition/evaporation rate and RH_{crit} sensitivity experiments for (a) temperature, (b) relative humidity with respect to water, (c) u-component of wind, and (d) v-component of wind.

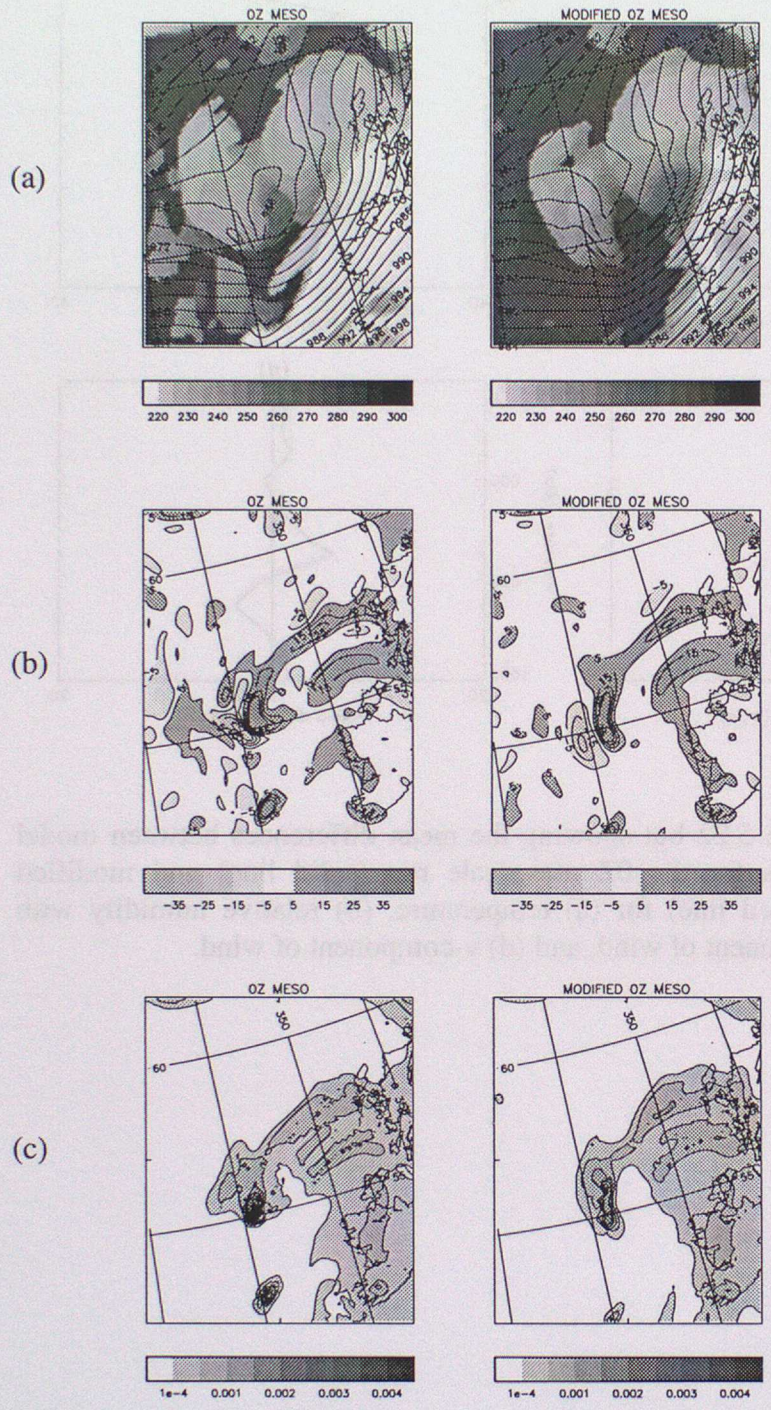

Figure 5.24 As for Figure 5.4 but (a) ice cloud top temperature (K) and surface pressure (hPa), (b) vertical velocity (cm/s) at 800hPa and (c) large scale surface rainfall ($kg/m^2/s$) for the 0Z MESO run and the modified parameter run.

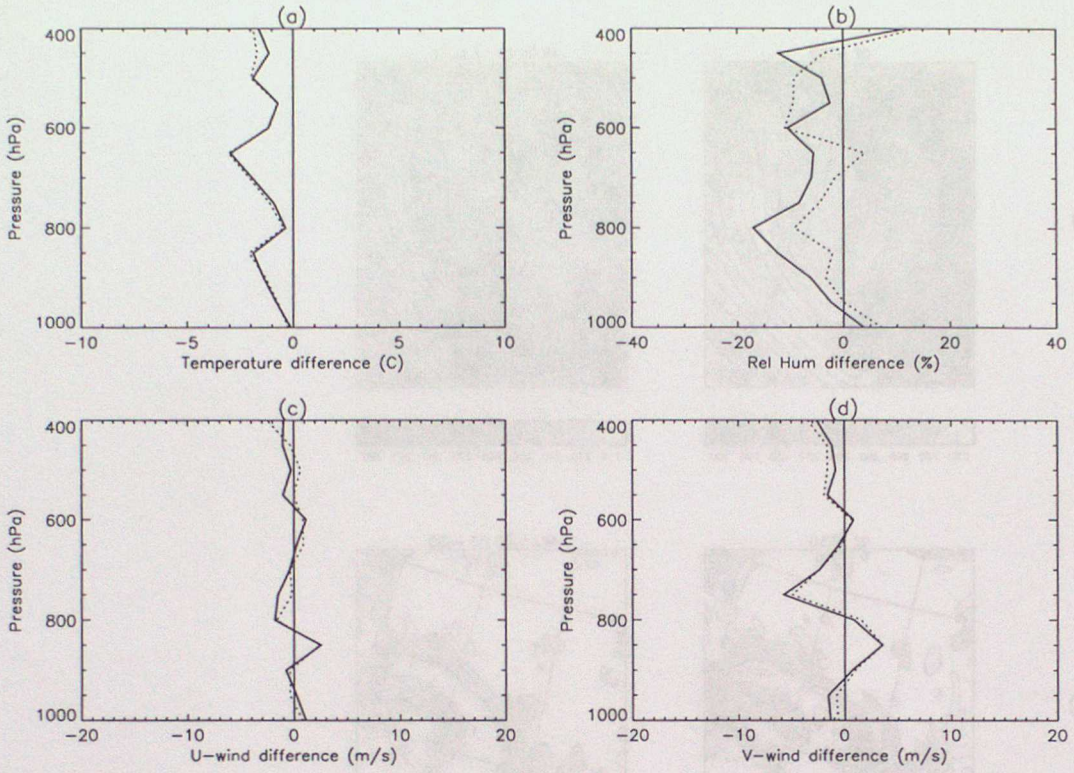

Figure 5.25 As for Figure 5.22 but showing the mean differences between model and dropsonde observations for the 0Z mesoscale run (solid line) and modified sensitivity experiment (dotted line) for (a) temperature, (b) relative humidity with respect to water, (c) u-component of wind, and (d) v-component of wind.